

REPORT DOCUMENTATION PAGE

Form Approved
OMB No. 0704-0188

Public reporting burden for this collection of information is estimated to average 1 hour per response, including the time for reviewing instructions, searching existing data sources, gathering and maintaining the data needed, and completing and reviewing this collection of information. Send comments regarding this burden estimate or any other aspect of this collection of information, including suggestions for reducing this burden to Department of Defense, Washington Headquarters Services, Directorate for Information Operations and Reports (0704-0188), 1215 Jefferson Davis Highway, Suite 1204, Arlington, VA 22202-4302. Respondents should be aware that notwithstanding any other provision of law, no person shall be subject to any penalty for failing to comply with a collection of information if it does not display a currently valid OMB control number. PLEASE DO NOT RETURN YOUR FORM TO THE ABOVE ADDRESS.

1. REPORT DATE (DD-MM-YYYY) 02/08/2007		2. REPORT TYPE Final Technical Report		3. DATES COVERED (From - To) 12/1/2003-11/30/2006	
4. TITLE AND SUBTITLE Swirl-Stabilized Injector Flow and Combustion Dynamics for Liquid Propellants at Supercritical Conditions				5a. CONTRACT NUMBER	
				5b. GRANT NUMBER FA9550-04-1-0014	
				5c. PROGRAM ELEMENT NUMBER	
6. AUTHOR(S) Vigor Yang				5d. PROJECT NUMBER	
				5e. TASK NUMBER	
				5f. WORK UNIT NUMBER	
7. PERFORMING ORGANIZATION NAME(S) AND ADDRESS(ES) The Pennsylvania State University 104 Research Building East University Park, PA 16802				8. PERFORMING ORGANIZATION REPORT NUMBER	
9. SPONSORING / MONITORING AGENCY NAME(S) AND ADDRESS(ES) Dr. Mitat A. Birkan / <i>MA</i> Air Force Office of Scientific Research 875 N. Randolph Street, Ste. 325 Arlington, VA 22203-1768				10. SPONSOR/MONITOR'S ACRONYM(S) AFOSR	
				11. SPONSOR/MONITOR'S REPORT NUMBER(S)	
12. DISTRIBUTION / AVAILABILITY STATEMENT Approved for public release; distribution unlimited. AFRL-SR-AR-TR-07-0138					
13. SUPPLEMENTARY NOTES					
14. ABSTRACT An integrated modeling and simulation program has been conducted to substantially improve the fundamental knowledge of supercritical combustion of liquid propellants under conditions representative of contemporary rocket engines. Both shear and swirl co-axial injectors were considered. The formulation was based on the complete conservation equations in three dimensions. In addition, general-fluid thermodynamics and transport theories were incorporated to allow for a unified treatment of fluid properties over the entire range of thermodynamic states. Turbulence closure was achieved by means of the large-eddy-simulation (LES) technique. Special attention was given to the fluid behavior in the two-phase and transcritical regimes in which rapid property variations occur. Various underlying physiochemical mechanisms associated with co-axial injector dynamics were studied in detail. These included flow evolution, flame stabilization and spreading, heat transfer, and acoustic response. The effects of design attributes and operating conditions on injector characteristics were assessed. Results have not only enhanced the basic understanding of the subject problem, but also provided a quantitative basis for identifying and prioritizing the key design parameters and flow variables that exert dominant influences on the injector behavior in different environments.					
15. SUBJECT TERMS supercritical fluid injection, mixing, and combustion; liquid rocket engines, injectors					
16. SECURITY CLASSIFICATION OF:			17. LIMITATION OF ABSTRACT UU	18. NUMBER OF PAGES 84	19a. NAME OF RESPONSIBLE PERSON
a. REPORT unclassified	b. ABSTRACT unclassified	c. THIS PAGE unclassified			19b. TELEPHONE NUMBER (include area code) (814) 863-1502

Final Report
on

**Swirl-Stabilized Injector Flow and Combustion Dynamics for
Liquid Propellants at Supercritical Conditions**

For

AFOSR Contract/Grant FA9550-04-1-0014

Prepared by

Vigor Yang
Department of Mechanical Engineering
The Pennsylvania State University
104 Research Building East

Submitted to:

Dr. Mitat A. Birkan
Air Force Office of Scientific Research
875 N. Randolph Street, Ste. 325
Arlington, VA 22203-1768

February 8, 2007

20070516066

Supercritical Combustion of Liquid Oxygen and Kerosene for Oxygen-Rich Preburner Staged-Combustion Cycle (ORPSCC) Engine Technology Development

SUMMARY

An integrated modeling and simulation program has been conducted to substantially improve the fundamental knowledge of supercritical combustion of liquid propellants under conditions representative of contemporary rocket engines. Both shear and swirl co-axial injectors were considered. The formulation was based on the complete conservation equations for a multi-component chemically reacting mixture in three dimensions. In addition, general-fluid thermodynamics and transport theories were incorporated to allow for a unified treatment of fluid properties over the entire range of thermodynamic states. Turbulence closure was achieved by means of the large-eddy-simulation (LES) technique. Start-of-the-art closure schemes for subgrid-scale dynamics and turbulence/chemistry interactions were implemented. Special attention was given to the fluid behavior in the two-phase and transcritical regimes in which rapid property variations occur. Furthermore, an efficient numerical framework utilizing contemporary computer software and hardware technologies were employed, such that sweeping calculations were performed within a realistic time frame.

The work contained the following four tasks in a hierarchical manner:

4. development of an efficient numerical algorithm for treating general-fluid mixtures with chemical reactions;
5. cryogenic fluid injection and mixing at supercritical conditions;
6. shear co-axial injection of cryogenic fluids with acoustic excitations; and
7. flow and flame dynamics of shear co-axial injectors with liquid oxygen (LOX) and methane

Various underlying physiochemical mechanisms associated with co-axial injector dynamics were studied in detail. These included flow evolution, flame stabilization and spreading, heat transfer, and acoustic response. The effects of design attributes (e.g., injection port size and location, center post recess distance, etc.) and operating conditions (e.g., chamber pressure, velocity, and temperature, swirl strength, etc.) on injector characteristics were assessed. Results have not only enhanced the basic understanding of the subject problem, but also provided a quantitative basis for identifying and prioritizing the key design parameters and flow variables that exert dominant influences on the injector behavior in different environments.

Results from this research project have led to the following publications.

1. "Dynamics of Simplex Swirl Injectors for Cryogenic Propellants at Supercritical Conditions," by N. Zong and V. Yang, AIAA Paper 2004-1332, presented at the AIAA 42nd Aerospace Sciences Meeting and Exhibit, January 2004, also submitted to *Physics of Fluids*, 2007.
2. "A Numerical Study of Cryogenic Fluid Injection and Mixing under Supercritical Conditions," by N. Zong, H. Meng, S.Y. Hsieh, and V. Yang, *Physics of Fluids*, Vol. 16, 2004, pp. 4248-4261.

3. "High-Pressure LOX/Methane Mixing and Combustion Processes," by N. Zong and V. Yang, AIAA Paper 2005-0152, presented at the 43rd AIAA Aerospace Sciences Meeting and Exhibit, January 2005.
4. "Supercritical LOX/Methane Flame Stabilization and Dynamics in a Shear Coaxial Injector," by N. Zong and V. Yang, AIAA Paper 2006-0760, presented at the 44th AIAA Aerospace Sciences Meeting and Exhibit, January 2006.
5. "Dynamics of Shear-Coaxial Cryogenic Nitrogen Jets with Acoustic Excitation under Supercritical Conditions," by T. Liu, N. Zong, and V. Yang, AIAA Paper 2006-0759, presented at the 44th AIAA Aerospace Sciences Meeting and Exhibit, January 2006.
6. "Cryogenic Fluid Jets and Mixing Layers in Transcritical and Supercritical Environments," by N. Zong and V. Yang, *Combustion Science and Technology*, Vol. 178, 2006, pp. 193-227.
7. "Near-Field Flow and Flame Dynamics of LOX/Methane Shear Coaxial Injector under Supercritical Conditions," by N. Zong and V. Yang, *Proceedings of the Combustion Institute*, Vol. 31, 2007, pp. 2309-2317.
8. "An Efficient Preconditioning Scheme for General Fluid Mixtures using Primitive Pressure-Temperature Variables," by Zong, N., and Yang, V., submitted for publication in *International Journal of Computational Fluid Dynamics*, February 2007.

TABLE OF CONTENTS

SUMMARY	1
Task 1 Development of an Efficient Numerical Algorithm for Treating General Fluid Mixtures with Chemical Reactions	3
1.1 Introduction	3
1.2 Theoretical Formulation	5
1.2.1 Thermodynamic Relations	6
1.2.2 Preconditioning Matrix	11
1.2.3 System Eigenvalues	12
1.3 Numerical Implementation	14
1.4 Stability Analysis	14
1.5 Sample Calculations	16
1.5.1 Cryogenic Nitrogen Fluid Jet Dynamics	16
1.5.2 Supercritical Mixing and Combustion of Oxygen and Methane	18
1.6 Conclusions	22
Appendix A	23
References	25
 Task 2 Cryogenic Propellant Injection and Mixing at Supercritical Conditions	27
2.1 Introduction	27
2.2 Theoretical Formulation	29
2.2.1 Governing Equations	30
2.2.2 Thermodynamic and Transport Properties	31
2.3 Numerical Method	33
2.4 Computational Domain and Grid System	33
2.5 Boundary Condition	34
2.6 Results and Discussions	35
2.6.1 Instantaneous Flowfield	36
2.6.2 Effect of Density Stratification	38
2.6.3 Shear-Layer Instability	41
2.6.4 Vortical Dynamics	43
2.6.5 Mean Flow Properties	45
2.7 Conclusions	47
References	52
 Task 3 Shear Co-axial Injection of Cryogenic Fluids with Acoustic Excitations	54
3.1 Introduction	54
3.2 Theoretical Formulation	55
3.2.1 Governing Equations	55

3.2.2 Equation of State and Thermodynamic Properties	57
3.2.3 Transport Properties Evaluation	57
3.3 Numerical Method and Boundary Conditions	57
3.4 Results and Discussions	58
3.4.1 Computational Case Description	58
3.4.2 Flow Evolution without External Acoustic Excitation	61
3.4.3 Flow Evolution with External Acoustic Excitation	61
3.5 Conclusion	67
References	69

Task 4 Flow and Flame Dynamics of Shear Co-axial Injectors with Liquid Oxygen (LOX) and Methane	70
4.1 Introduction	70
4.2 Theoretical formulation and numerical treatment	71
4.2.1 Turbulence/flame-structure interaction	72
4.2.2 Computational domain and boundary conditions	73
4.2.3 Numerical framework	74
4.3 Results and discussions	75
4.4 Conclusions	80
References	81

Task 1

Development of an Efficient Numerical Algorithm for Treating General-Fluid Mixtures with Chemical Reactions

The unified treatment of general fluid thermodynamics developed by Meng and Yang for supercritical fluid transport and combustion has been improved and incorporated into a highly efficient preconditioning scheme using primitive pressure-temperature type variables. The major advantageous of this newly developed algorithm include 1). all the numerical relationships, including the preconditioning matrix, Jacobian matrices, and eigenvalues, are derived based fundamental thermodynamics theories with the concepts of partial-mass and partial-density properties. This renders a self-consistent and robust algorithm valid for fluid flows at all speeds and at all thermodynamic states; 2). since pressure, temperature, and mass fraction are selected as the primary dependent variables of the governing system and solved directly, the cumbersome iterative solution of real-fluid equations of state is eliminated; and 3). the original governing system can be fully recovered for high-speed flows because of the use of a universal and general preconditioning matrix.

The work has remedied several deficiencies in the previous studies. Most importantly, computational efficiency has been significantly improved because the tedious iterative solution of a real-fluid equation of state is avoided through a careful selection of the primary dependent variables of the governing system. In addition, load balance can be easily achieved on a distributed computing facility. The resultant scheme is highly efficient and suitable for parallel implementation. This feature is extremely attractive because of the large-scale numerical calculations required for three-dimensional simulations of injector flow and flame dynamics. A comprehensive description of this new approach is given in the following paper which has been submitted for publication in the *International Journal of Computational Fluid Dynamics*.

“An Efficient Preconditioning Scheme for General Fluid Mixtures using Primitive Pressure-Temperature Variables,” by Zong, N., and Yang, V., submitted for publication in *International Journal of Computational Fluid Dynamics*, February 2007.

1.1 Introduction

The development of an efficient numerical algorithm capable of handling fluid flows over a broad range of thermodynamic states is of particular importance for many scientific and engineering problems involving fluid phase transition from a subcritical to a supercritical state. Notable examples include fluid transport, heat transfer, material processing, and high-pressure combustion for propulsion and power-generation applications. Thermodynamic non-idealities and transport anomalies often occur under these conditions, especially during the transition through the transcritical regime [1]. Thus, treating fluid-state transition and thermophysical-property variations in a manner consistent with the intrinsic characteristics of a numerical algorithm is critical to achieving numerical efficiency and robustness.

Several attempts have been made to treat fluid flows at different thermodynamic states. Merkel et al. [2] extended a preconditioning scheme for ideal gases [3-8] to accommodate arbitrary

equations of state. The resultant scheme, along with the use of the Soave-Redlich-Kwong equation of state, has been employed to simulate supercritical hydrogen flow through a two-dimensional cascade and a heated rectangular duct. Although encouraging results were obtained for the specific problems considered, no information was given about the evaluation of thermophysical properties. The relationship between numerical properties and general fluid thermodynamics was not addressed.

Edwards et al. [9] considered real-fluid flows with liquid-vapor phase transition using a low-diffusion flux-splitting scheme [10]. The fluid p - v - T behavior in the liquid phase was modeled with the Sanchez-Lacombe equation of state. A homogeneous vapor-liquid phase equilibrium model was employed to study the vapor cavitation during liquid carbon dioxide expansion through a sharp-orifice nozzle. Numerical experiments demonstrated the effectiveness of the method in capturing several important two-phase flow phenomena, such as cavitation bubbles and vapor-liquid condensation shocks. The scheme was later extended to investigate gas-solid two-phase flows in fluidized beds under different flow conditions [11].

Oefelein and Yang [12] extended the preconditioning methodology described in [13] to handle multi-component, dense-fluid mixtures with finite-rate chemical kinetics at supercritical pressures. Temporally accurate solutions were obtained through the implementation of a dual-time-stepping integration technique, in which the primitive variables of pressure, velocity components, temperature, and mass fraction, were chosen as the dependent variables in pseudo-time. The Soave-Redlich-Kwong equation of state was employed to predict the fluid volumetric behavior except in regions near the critical point, for which the Benedict-Webb-Rubin equation of state was used. Thermodynamics properties, such as the enthalpy, Gibbs energy, and specific heat, were obtained as explicit functions of temperature and pressure by using Maxwell's relations to derive thermodynamic departure functions [1]. Transport properties were estimated using an extended corresponding-state principle. The combined theoretical/numerical framework was applied to study the mixing and combustion of cryogenic propellants in supercritical environments [12,14]. The properties of fluid mixtures (i.e., enthalpy, and internal energy) in their analysis, however, were evaluated with the formulas for an ideal-gas mixture, taking as the mass-weighted sum of the values of constituent species without considering their interactions. Since the coupling among molecules of different species may be significant in real fluids, such a simplification leads to inconsistency with real-fluid equations of state and other property-evaluation schemes.

To remedy this deficiency, Meng and Yang [15] developed a unified numerical treatment of general fluid thermodynamics. The concepts of partial mass and partial density were introduced to evaluate the properties of real-fluid mixtures. All of the thermodynamic properties and numerical relations, including the Jacobian matrices and eigenvalues, were derived directly from fundamental thermodynamics theories, rendering a self-consistent and robust algorithm valid over the entire range of fluid states. Furthermore, full account is taken of transport property variations as functions of fluid density, temperature, and composition. The resultant numerical properties and property evaluation routines were incorporated into a preconditioning scheme [13] to handle fluid flows at all speeds. The overall approach is general and can accommodate any type of equation of state.

In spite of its effectiveness in treating real-fluid flows with thermodynamic non-idealities and transport anomalies in the transcritical regime [15, 16], the aforementioned formulation can not, in general, be solved in a non-iterative manner because the specific enthalpy is used as one of the dependent variables in the formulation of the pseudo-time derivatives. Extensive iterations at each time step and grid point are required to determine the fluid temperature from the specific enthalpy.

Although such iterations are straightforward to accomplish for an ideal-gas mixture, the procedures become quite complicated and time-consuming for real-fluid mixtures due to the complicated form of the equation of state and property evaluation schemes. The iterative solution of real-fluid equation of state not only significantly increases the computational cost, but also impairs the scalability of a parallelized code.

The purpose of the present work is to circumvent this limitation by replacing specific enthalpy with temperature as a primary dependent variable in the numerical formulation. Such an employment of the pressure-temperature type of primitive variables has been made in many existing approaches [3-8] and offers the following advantages. First, laborious iterations in calculating temperature from specific enthalpy or internal energy are avoided, rendering a highly efficient algorithm for real-fluid mixtures. Second, load balance is easier to achieve on a distributed computing facility since no iterative solution of the equation of state is required. The computation burden at each spatial grid point is the same. Third, computation of numerical Jacobian matrices is simplified, especially within the context of the general fluid thermodynamics. In addition, the preconditioning matrix in this study is derived by analyzing the eigenvalues of the governing system. All the off-diagonal terms in the Jacobian matrix relating the conservative to preconditioning variables are retained. The original governing equations can thus be fully recovered for high-speed flows in a steady-state simulation. The scheme is further optimized to facilitate parallel computation by treating the pseudo-time and spatial derivatives using a fourth-order Runge-Kutta (RK4) scheme [17] and an explicit fourth-order flux-differencing scheme [18], respectively. Because the time advancement is fully explicit in the pseudo-time space, the approach not only guarantees high-order numerical accuracy in both time and space, but also greatly simplifies the implementation of a parallelized code.

The remainder of this part is organized as follows. In Section 1.2, we briefly summarize the theoretical framework, including the governing equations and basic thermodynamics theories for general fluid mixtures. Fundamental thermodynamic and numerical attributes are established. Section 1.3 deals with the numerical implementation of the present scheme. A stability analysis is carried out in Section 1.4 to characterize the stability and convergence behavior of the algorithm. Section 1.5 presents results from selected numerical experiments, along with an assessment of the computational efficiency. Finally, a brief summary concludes the work.

1.2 Theoretical Formulation

To facilitate discussion, we consider the two-dimensional conservation equations of mass, momentum, energy, and species transport for a chemically reacting system of N species. Following the approach detailed in [4,6] for developing a preconditioning scheme for fluid flows at all speeds, a pseudo-time derivative of the form $\Gamma \partial \hat{Q} / \partial \tau$ is added to the conservation equations,

$$\Gamma \frac{\partial \hat{Q}}{\partial \tau} + \frac{\partial Q}{\partial t} + \frac{\partial (E - E_v)}{\partial x} + \frac{\partial (F - F_v)}{\partial x} = S \quad (1)$$

where Γ represents the preconditioning matrix and τ the pseudo-time. The conservative variable vector, Q , is defined as,

$$Q = y^\delta [\rho \quad \rho u \quad \rho v \quad \rho e_t \quad \rho Y_i]^\top. \quad (2)$$

The exponent $\delta = 0$ or 1 corresponds to a planar two-dimensional or an axisymmetric case, respectively. Standard notation in fluid mechanics is used here, with ρ , (u, v) , e_i , and Y_i denoting the density, velocity components, specific total energy, and mass fraction of species i , respectively. Explicit expressions of the convective flux vectors, E and F , and the diffusion flux vectors, E_v , and F_v , are given in [13-15]. The source term in Eq. (1), S , arises from chemical reactions or axisymmetric geometry [13].

Because the pseudo-time derivative in Eq. (1) vanishes at convergence, a certain amount of liberty can be taken in the selection of the pseudo-time variables [8]. Different options have been proposed for the primary dependent variables in the preconditioning scheme for ideal gases. Those include conservative and several sets of primitive (e.g., pressure-entropy, pressure-enthalpy, and pressure-temperature) variables [8]. The influences of selected preconditioning variables on the numerical convergence and accuracy for low-Mach number aerodynamic problems were examined by Turkel and colleagues [19,20]. Results indicated that the pressure-temperature type of primitive variables, which had long been a favorable choice by many researchers, led to fast convergence for simulating steady-state flows. The present study follows the same approach, and the pseudo-time variable vector, \hat{Q} , is thus defined as

$$\hat{Q} = [p_g, u, v, T, Y_i]. \quad (3)$$

The use of the gauge pressure, p_g , taken as the static pressure subtracted by a reference pressure [4,13], is crucial for two reasons. First, it allows the vectors E , F , E_v , F_v , and S to be expressed as unique functions of \hat{Q} [13]. Second, p_g is much more sensitive to the solution than the density at low Mach numbers, and thus provides a stronger velocity-pressure coupling in the momentum balance [6]. The selection of the velocity components (u, v) , temperature, T , and species mass fraction, Y_i , helps maintain the direction of the diffusion process, simplifies the structures of viscous vectors, and reduces the computational complexity [5]. In contrast to the schemes with the pressure-enthalpy type of primitive variables, all the thermodynamic properties of pressure, temperature, and mass fraction are directly solved, thereby eliminating tedious iterative solutions of the equations of state.

1.2.1 Thermodynamic Relations

To develop a robust numerical scheme in a manner consistent with real-fluid thermodynamics, all the numerical properties and relations, including the preconditioning matrix, Jacobian matrices, and system eigenvalues, must be derived in accordance with fundamental thermodynamics theories described in Meng and Yang [15]. The procedure should conform to the concepts of partial mass and partial density properties for fluid mixtures, along with the use of an appropriate equation of state.

Four thermodynamic relationships beyond those established in [15] are needed to derive the numerical properties. Those equations define density, enthalpy, and internal energy as functions of such dependent variables as pressure, temperature, and mass fraction, and consequently can be used to determine the Jacobian matrices $T \equiv \partial Q / \partial \hat{Q}$, $A \equiv \partial E / \partial \hat{Q}$, $B \equiv \partial F / \partial \hat{Q}$, and $D \equiv \partial S / \partial \hat{Q}$ (see Appendix A), as well as the associated eigen-properties.

Pressure as function of density, temperature, and mass fraction

The first relationship expresses pressure as a function of temperature, density, and mass fractions. For a general fluid mixture consisting of N species, each intensive thermodynamic property can be determined by the other $N+1$ properties of the mixture. This leads to the following expression:

$$p = p(T, \rho_i) \quad (4)$$

where $i = 1, \dots, N$. The differential form of Eq. (4) is

$$dp = \left(\frac{\partial p}{\partial T} \right)_{\rho_i} dT + \sum_{i=1}^N \left(\frac{\partial p}{\partial \rho_i} \right)_{T, \rho_{j \neq i}} d\rho_i \quad (5)$$

We may change the summation on the right hand side of Eq. (5) from 1 through N to 1 through $N-1$ to obtain the following relation:

$$dp = \left(\frac{\partial p}{\partial T} \right)_{\rho_i} dT + \sum_{i=1}^{N-1} \left[\left(\frac{\partial p}{\partial \rho_i} \right)_{T, \rho_{j \neq i}} - \left(\frac{\partial p}{\partial \rho_N} \right)_{T, \rho_{j \neq N}} \right] d\rho_i + \left(\frac{\partial p}{\partial \rho_N} \right)_{T, \rho_{j \neq N}} d\rho_N \quad (6)$$

Since $\rho_i = \rho Y_i$,

$$d\rho_i = Y_i d\rho + \rho dY_i \quad (7)$$

substitution of Eq. (7) into Eq. (6) yields

$$dp = A_T dT + A_{Y_i} dY_i + A_\rho d\rho \quad (8)$$

where

$$A_T = \left(\frac{\partial p}{\partial T} \right)_{\rho_i} \quad (9a)$$

$$A_{Y_i} = \rho \left[\left(\frac{\partial p}{\partial \rho_i} \right)_{T, \rho_{j \neq i}} - \left(\frac{\partial p}{\partial \rho_N} \right)_{T, \rho_{j \neq N}} \right] \quad (9b)$$

$$A_\rho = \left(\frac{\partial p}{\partial \rho} \right)_{T, Y_i} \quad (9c)$$

It has been shown in Ref. [15] that the speed of sound for a general fluid mixture can be expressed as

$$a^2 = \left(\frac{\partial p}{\partial \rho} \right)_{s, Y_i} = \frac{C_p}{C_v} \left(\frac{\partial p}{\partial \rho} \right)_{T, Y_i} = \gamma A_\rho \quad (10)$$

where C_p and C_v are constant-pressure and constant-volume specific heats, respectively, and γ is the ratio of specific heat.

Internal energy as function of temperature, pressure, and mass fraction

The second relationship expresses internal energy as a function of pressure, density, and mass fractions. We begin with the following functional relationship:

$$\rho e = \rho e(T, \rho_i) \quad (11)$$

where $i = 1, \dots, N$, and e the specific internal energy. The differential form of Eq. (11) can be written as

$$d\rho e = \rho \left(\frac{\partial e}{\partial T} \right)_{\rho_i} dT + \sum_{i=1}^N \left(\frac{\partial \rho e}{\partial \rho_i} \right)_{T, \rho_{j \neq i}} d\rho_i \quad (12)$$

The derivative in the first term on the right hand side is the constant-volume heat capacity, C_v , and that in the second term is the partial-density internal energy, \tilde{e}_i [15],

$$\tilde{e}_i = \left(\frac{\partial \rho e}{\partial \rho_i} \right)_{T, \rho_{j \neq i}} \quad (13)$$

Equation (12) thus becomes

$$d\rho e = \rho C_v dT + \sum_{i=1}^N \tilde{e}_i d\rho_i \quad (14)$$

Substitution of Eq. (7) into Eq. (14) gives

$$d\rho e = \rho C_v dT + \sum_{i=1}^N \tilde{e}_i \rho dY_i + \sum_{i=1}^N \tilde{e}_i Y_i d\rho \quad (15)$$

Since $d\rho e = \rho de + e d\rho$, a simple manipulation of Eq. (15) results in

$$de = C_v dT + \sum_{i=1}^{N-1} (\tilde{e}_i - \tilde{e}_N) dY_i + \frac{1}{\rho} \left(\sum_{i=1}^N Y_i \tilde{e}_i - e \right) d\rho \quad (16)$$

Substitution of Eq. (8) into the above equation leads to

$$de = B_T dT + B_p dp + \sum_{i=1}^{N-1} B_{Y_i} dY_i \quad (17)$$

where

$$B_T = C_v - \frac{1}{\rho} \left(\sum_{i=1}^N Y_i \tilde{e}_i - e \right) \left(\frac{\partial \rho}{\partial p} \right)_{T, Y_i} \left(\frac{\partial p}{\partial T} \right)_{\rho_i} \quad (18a)$$

$$B_p = \frac{1}{\rho} \left(\sum_{i=1}^N Y_i \tilde{e}_i - e \right) \left(\frac{\partial \rho}{\partial p} \right)_{T, Y_i} \quad (18b)$$

$$B_{Y_i} = \left\{ (\tilde{e}_i - \tilde{e}_N) - \left(\sum_{i=1}^N Y_i \tilde{e}_i - e \right) \cdot \left(\frac{\partial \rho}{\partial p} \right)_{T, Y_i} \cdot \left[\left(\frac{\partial p}{\partial \rho_i} \right)_{T, \rho_{j \neq i}} - \left(\frac{\partial p}{\partial \rho_N} \right)_{T, \rho_{j \neq N}} \right] \right\} \quad (18c)$$

Enthalpy as function of temperature, pressure, and mass fraction

The third relationship expresses enthalpy as a function of pressure, temperature, and mass fractions. According to basic thermodynamic definitions, we have

$$dh = de + \frac{1}{\rho} dp - \frac{p}{\rho^2} d\rho \quad (19)$$

Substitution of Eq. (8) and Eq. (17) into Eq. (19) and following some straightforward manipulations, we obtain

$$dh = D_T dT + D_p dp + \sum_{i=1}^{N-1} D_{Y_i} dY_i \quad (20)$$

where

$$D_T = C_v - \frac{1}{\rho} \left(\frac{\partial p}{\partial T} \right)_{\rho_i} \left(\frac{\partial \rho}{\partial p} \right)_{T, Y_i} \left(\sum_{i=1}^N Y_i \tilde{e}_i - e - \frac{p}{\rho} \right) \quad (21a)$$

$$D_p = \frac{1}{\rho} + \frac{1}{\rho} \left(\frac{\partial \rho}{\partial p} \right)_{T, Y_i} \left(\sum_{i=1}^N Y_i \tilde{e}_i - e - \frac{p}{\rho} \right) \quad (21b)$$

$$D_{Y_i} = \tilde{e}_i - \tilde{e}_N - \left(\frac{\partial \rho}{\partial p} \right)_{T, Y_i} \left(\sum_{i=1}^N Y_i \tilde{e}_i - e - \frac{p}{\rho} \right) \left[\left(\frac{\partial p}{\partial \rho_i} \right)_{T, \rho_{j \neq i}} - \left(\frac{\partial p}{\partial \rho_N} \right)_{T, \rho_{j \neq N}} \right] \quad (21c)$$

The coefficient, D_T , is equivalent to the constant-pressure heat capacity, C_p , of a fluid mixture, according to its definition. Thus,

$$C_p = D_T = C_v - \frac{1}{\rho} \left(\frac{\partial p}{\partial T} \right)_{\rho_i} \left(\frac{\partial \rho}{\partial p} \right)_{T, Y_i} \left(\sum_{i=1}^N Y_i \tilde{e}_i - e - \frac{p}{\rho} \right) \quad (22)$$

Relationship between constant-pressure and constant-volume specific heats

The final relationship deals with constant-pressure and constant-volume specific heats. According to fundamental thermodynamics for a multi-component mixture,

$$s = s(T, \rho, Y_i) \quad i = 1, \dots, N-1 \quad (23)$$

Its differential form can be written as

$$ds = \frac{C_v}{T} dT + \left(\frac{\partial s}{\partial \rho}\right)_{T, Y_i} d\rho + \sum_{i=1}^{N-1} \left(\frac{\partial s}{\partial Y_i}\right)_{T, \rho, Y_{j \neq i}} dY_i \quad (24)$$

A similar relationship that defines entropy as a function of temperature, pressure, and mass fraction can be easily derived as

$$ds = \frac{C_p}{T} dT + \left(\frac{\partial s}{\partial p}\right)_{T, Y_i} dp + \sum_{i=1}^{N-1} \left(\frac{\partial s}{\partial Y_i}\right)_{T, p, Y_{j \neq i}} dY_i \quad (25)$$

Combination of Eqs. (24) and (25) and rearrangement of the result lead to

$$\left(\frac{C_p}{T} - \frac{C_v}{T}\right) dT = \left(\frac{\partial s}{\partial \rho}\right)_{T, Y_i} d\rho - \left(\frac{\partial s}{\partial p}\right)_{T, Y_i} dp + \sum_{i=1}^{N-1} \left[\left(\frac{\partial s}{\partial Y_i}\right)_{T, \rho, Y_{j \neq i}} - \left(\frac{\partial s}{\partial Y_i}\right)_{T, p, Y_{j \neq i}} \right] dY_i \quad (26)$$

Substitution of Eq. (8) into Eq. (26) and elimination of dp give,

$$\begin{aligned} \left[\frac{C_p}{T} - \frac{C_v}{T} + \left(\frac{\partial s}{\partial \rho}\right)_{T, Y_i} \left(\frac{\partial p}{\partial T}\right)_{T, Y_i} \right] dT &= \left[\left(\frac{\partial s}{\partial \rho}\right)_{T, Y_i} - \left(\frac{\partial s}{\partial p}\right)_{T, Y_i} \left(\frac{\partial p}{\partial \rho}\right)_{T, Y_i} \right] d\rho \\ &+ \sum_{i=1}^{N-1} \left[\left(\frac{\partial s}{\partial Y_i}\right)_{T, \rho, Y_{j \neq i}} - \left(\frac{\partial s}{\partial Y_i}\right)_{T, p, Y_{j \neq i}} - \left(\frac{\partial s}{\partial p}\right)_{T, Y_i} \left(\frac{\partial p}{\partial Y_i}\right)_{T, Y_{j \neq i}} \right] dY_i \end{aligned} \quad (27)$$

Since temperature, density, and mass fraction can vary independently, the coefficients of the above differentials must vanish. Thus,

$$C_p = C_v - T \left(\frac{\partial s}{\partial \rho}\right)_{T, Y_i} \left(\frac{\partial p}{\partial T}\right)_{\rho, Y_i} \quad (28)$$

Application of the well-known Maxwell relation [21],

$$\left(\frac{\partial s}{\partial \rho}\right)_{T, Y_i} = \frac{1}{\rho^2} \left(\frac{\partial \rho}{\partial T}\right)_{\rho, Y_i} = -\frac{1}{\rho^2} \left(\frac{\partial p}{\partial T}\right)_{\rho, Y_i} \left/ \left(\frac{\partial p}{\partial \rho}\right)_{T, Y_i} \right., \quad (29)$$

gives,

$$C_p = C_v + \frac{T}{\rho^2} \left(\frac{\partial p}{\partial T}\right)_{\rho, Y_i}^2 \left/ \left(\frac{\partial p}{\partial \rho}\right)_{T, Y_i} \right. \quad (30)$$

This relationship will be employed to calculate the eigenvalues of the preconditioned governing system.

1.2.2 Preconditioning Matrix

The precondition matrix Γ in Eq. (2.1) is introduced to rescale the system eigenvalues in such a manner that they have the same order of magnitude to ensure uniform convergence at all Mach numbers. The specific form of the matrix is not unique [8], and is selected to maximize the numerical efficiency over a broad range of flow conditions. Generally, this matrix can be constructed by means of either an eigenvalue analysis [3,8] or an asymptotic theory [22,23].

Following the standard approach suggested in Refs. [5], we examine the Jacobian matrix $T \equiv \partial Q / \partial \hat{Q}$ in Appendix A. A common term $(\partial \rho / \partial p)_{T, Y_i}$, which can be expressed as

$$\left(\frac{\partial \rho}{\partial p} \right)_{T, Y_i} = \frac{C_p}{C_v} \left(\frac{\partial p}{\partial \rho} \right)_{s, Y_i} = \frac{\gamma}{a^2}, \quad (2.31)$$

is identified in each element of the first column of T . It is this term, after multiplication of the time derivatives of dependent variables in Eq. (2.1), that dictates the propagation speeds of acoustic waves in the governing system [5]. The preconditioning matrix is, then, established by simply replacing this term with a scaling factor, Θ .

$$\Gamma = \begin{pmatrix} \Theta & 0 & 0 & -\frac{A_T}{A_\rho} & -\frac{A_{Y_1}}{A_\rho} & \dots & -\frac{A_{Y_{N-1}}}{A_\rho} \\ \Theta u & \rho & 0 & -\frac{A_T u}{A_\rho} & -\frac{A_{Y_1} u}{A_\rho} & \dots & -\frac{A_{Y_{N-1}} u}{A_\rho} \\ \Theta v & 0 & \rho & -\frac{A_T v}{A_\rho} & -\frac{A_{Y_1} v}{A_\rho} & \dots & -\frac{A_{Y_{N-1}} v}{A_\rho} \\ \Theta h_i + \left(\sum_{i=1}^N Y_i \tilde{e}_i - e - \frac{p}{\rho} \right) \left(\frac{\partial \rho}{\partial p} \right)_{T, Y_i} & \rho u & \rho v & \rho B_T - \frac{A_T e_i}{A_\rho} & \rho B_{Y_1} - \frac{A_{Y_1} e_i}{A_\rho} & \dots & \rho B_{Y_{N-1}} - \frac{A_{Y_{N-1}} e_i}{A_\rho} \\ \Theta Y_1 & 0 & 0 & -\frac{A_T Y_1}{A_\rho} & \rho - \frac{A_{Y_1} Y_1}{A_\rho} & \dots & -\frac{A_{Y_{N-1}} Y_1}{A_\rho} \\ \vdots & \vdots & \vdots & \vdots & \vdots & \ddots & \vdots \\ \Theta Y_{N-1} & 0 & 0 & -\frac{A_T Y_{N-1}}{A_\rho} & -\frac{A_{Y_1} Y_{N-1}}{A_\rho} & \dots & \rho - \frac{A_{Y_{N-1}} Y_{N-1}}{A_\rho} \end{pmatrix} \quad (32)$$

where the two sets of coefficients, (A_T, A_ρ, A_{Y_i}) and (B_T, B_{Y_i}) are defined by Eqs (9) and (18), respectively. The scaling factor, Θ , is defined as,

$$\Theta = [1/\varepsilon^2 + (\gamma - 1)]/a^2 \quad (33)$$

The preconditioning factor, ε , lies between 0 and 1. In comparison with the preconditioning matrices defined in [4,5,13,15], all of the off-diagonal terms in Eq. (32) are

retained. The preconditioning matrix becomes the Jacobian matrix $T \equiv \partial Q / \partial \hat{Q}$ in the limit of $\varepsilon \rightarrow 1$, and the original governing system is recovered for high-speed flows in a steady state simulation. For an ideal gas, the preconditioning matrix, Γ , reduces to the form introduced by Weiss and Smith [6], and becomes a member of the generalized preconditioner family suggested by Turkel [3,8]. For an incompressible fluid, as the speed of sound, a , reaches infinite, the preconditioning matrix takes a form similar to that proposed in Ref. [5]. As will be shown later, through an appropriate selection of the preconditioning factor, ε , the preconditioning matrix developed herein can effectively circumvent the eigenvalue-disparity problem associated with low-Mach number flows and help achieve an optimal convergence rate in the entire flowfield.

According to Ref. [5], the preconditioning factor for an inviscid flow is specified as

$$\varepsilon_{inv} = \begin{cases} \varepsilon_{min} & M \leq \varepsilon_{min} \\ M^2 & \varepsilon_{min} < M < 1 \\ 1 & M \geq 1 \end{cases} \quad (34)$$

A lower bound, ε_{min} , typically taken as 10^{-5} , is used to avoid the singularity of a stagnation point. In regions where diffusion plays a dominant role in determining the flow behavior, it is important to simultaneously control both the Courant-Friedriches-Lewy (CFL) and von Neumann (VNN) numbers to achieve efficient convergence [24]. Oefelein and Yang [12] suggested that the viscous preconditioning factor, ε_{vis} , be selected as

$$\varepsilon_{vis} = \max \left[\frac{u^2 \delta_x (\delta_x - 1)}{u^2 \delta_x^2 + a^2}, \frac{v^2 \delta_y (\delta_y - 1)}{v^2 \delta_y^2 + a^2} \right] \quad (35)$$

where

$$\begin{aligned} \delta_x &= \max \left(\nu, \frac{\nu}{Pr}, \frac{\nu}{Sc_i} \right) \frac{1}{u} \frac{CFL}{VNN} \\ \delta_y &= \max \left(\nu, \frac{\nu}{Pr}, \frac{\nu}{Sc_i} \right) \frac{1}{v} \frac{CFL}{VNN} \end{aligned} \quad (36)$$

and ν , Pr , and Sc_i are the kinematic viscosity, cell Prandtl number, and cell Schmidt number of species i , respectively. Equation (36) takes into account the effects of momentum, energy, and mass diffusion on the overall convergence rate.

A preconditioning factor that can optimally control both convection and diffusion processes is determined locally as

$$\varepsilon = \min[1, \max(\varepsilon_{inv}, \varepsilon_{vis})] \quad (37)$$

1.2.3 System Eigenvalues

The basic characteristics of the algorithm developed herein, specifically, the numerical convergence and stability properties, can be examined by studying the system eigenvalues. For

brevity, only those eigenvalues associated with the inviscid flux vector in the axial direction, $\Gamma^{-1}A$ with $A \equiv \partial E / \partial \hat{Q}$, are discussed.

$$\lambda_A = \text{diag}(\lambda_1 \quad \lambda_2 \quad u \quad u \quad \dots \quad u) \quad (38)$$

where λ_1 and λ_2 represent the rescaled acoustic-wave speeds propagating upstream and downstream, respectively,

$$\lambda_{1,2} = \frac{1}{2}[(q_{11} + u) \pm \sqrt{(q_{11} - u)^2 - 4(uq_{11} - \varepsilon a^2)}] \quad (39)$$

The variable q_{11} represents the first element in the first column of the matrix, $\Gamma^{-1}A$.

$$q_{11} = u \left(\frac{\gamma C_p}{a^2} - \frac{T}{\rho^2} \frac{A_T^2}{A_p^2} \right) \bigg/ \left(\frac{\gamma C_p}{\beta} - \frac{T}{\rho^2} \frac{A_T^2}{A_p^2} \right) \quad (40)$$

where A_T and A_p , are given in Eqs. (9a) and (9c), respectively. We then obtain,

$$\frac{A_T^2}{A_p^2} = \left(\frac{\partial p}{\partial T} \right)_{\rho_i}^2 \bigg/ \left(\frac{\partial p}{\partial \rho} \right)_{T,Y_i}^2 \quad (41)$$

Combination of Eqs. (41) and (30) and substitution of Eq. (10) into the resultant equation yield

$$C_p = C_v + \frac{T}{\rho^2} \cdot \frac{A_T^2}{A_p^2} \cdot \frac{C_v}{C_p} a^2 \quad (42)$$

The above equation can be rearranged to become

$$\frac{A_T^2}{A_p^2} = \frac{\rho^2 (\gamma - 1) C_p}{T a^2} \quad (43)$$

Incorporation of Eq. (43) into Eq. (40) leads to

$$q_{11} = u \left(\frac{\gamma C_p}{a^2} - \frac{T}{\rho^2} \frac{A_T^2}{A_p^2} \right) \bigg/ \left(\frac{\gamma C_p}{\beta} - \frac{T}{\rho^2} \frac{A_T^2}{A_p^2} \right) = \varepsilon u \quad (44)$$

The first two system eigenvalues, $\lambda_{1,2}$, can thus be obtained by substituting Eq. (44) into Eq. (39).

$$\lambda_{1,2} = \frac{1}{2}[(1 + \varepsilon)u \pm \sqrt{(1 - \varepsilon)^2 u^2 + 4\varepsilon a^2}] \quad (45)$$

All of the eigenvalues in the pseudo-time space are real, and have signs consistent with the directions of characteristic wave propagation. The present scheme not only preserves the

hyperbolicity of the system, but also gives rise to individual eigenvalues that behave in a manner representative of the physical reality involved [13]. The same conclusion was reached in [15] using different pseudo-time variables and preconditioning matrix.

1.3 Numerical Implementation

A dual-time-stepping integration technique is implemented to obtain time-accurate results [4,12,13,15]. The solution converged in pseudo-time corresponds to a time-accurate solution in physical-time. One major advantage of this technique lies in the fact that the convergence of the iterative process is dictated by the well-behaved eigenvalues in the pseudo-time space, instead of the original eigenvalues that may become disparate in certain flow regimes (e.g., low Mach-number flows) [4].

A standard fourth-order Runge-Kutta (RK4) scheme [17] is employed to perform the inner-loop pseudo-time integration because of its relatively higher temporal accuracy and greater stability margin compared to many commonly used explicit schemes. The temporal discretization of the real-time derivative term is obtained using a second-order backward difference. Spatial discretization is achieved by means of a fourth-order flux differencing scheme [18]. Further improvement is acquired by adding both the second- and fourth-order artificial dissipation with a total-variation-diminish (TVD) switch [25,26] to ensure numerical stability and convergence. The entire approach guarantees that the second-order artificial dissipation exerts an appropriate influence in regions with strong gradients, whereas only the fourth-order dissipation exists in smooth regimes to achieve numerical stability. The details regarding implementation of artificial dissipation in a preconditioning scheme can be found in [8].

Because the time advancement is fully explicit in pseudo-time and only the neighboring data at the previous time step is required when evaluating the derivatives of the convective and viscous terms, the present scheme is suitable for parallel implementation. The scheme is then parallelized using a multiblock domain decomposition technique with message passing interfaces (MPI) at the domain boundaries. The parallelization methodology is robust and the speedup is almost linear.

1.4 Stability Analysis

A von Neumann analysis is performed to characterize the stability and convergence behavior of the present scheme. For simplicity, only the inviscid part without any source terms is considered, and the coefficient matrices are assumed to be locally constant. The amplification matrix is obtained by the Fourier transformation of the discretized governing equations to the wave-number space. The partial derivatives of the thermodynamic properties in the corresponding numerical Jacobian matrices and the fluid p-v-T behavior are evaluated with a modified Soave-Redlich-Kwong equation of state [27,28].

Figure 1a shows the one-dimensional stability characteristics for an ideal gas in terms of the magnitude of the largest eigenvalue of the amplification matrix. The numerical parameters are $CFL = 0.7$, $\Delta\tau/\Delta t = 1$, and $\epsilon_x^{(4)} = 1/64$, where the latter denotes the coefficient of the fourth-order artificial dissipation. The result of the RK4 integration combined with the fourth-order central differencing (4CD) scheme is also included for comparison. The amplification factor of the standard RK4-4CD algorithm approaches unity in the bulk of the wave-number space, whereas the preconditioning technique stabilizes numerical calculations over the entire domain at all Mach numbers.

The effects of fluid state on the numerical stability behavior are investigated by considering nitrogen fluid at a near-critical ($p = 40 \text{ atm}$ and $T = 120 \text{ K}$), a transcritical ($p = 90 \text{ atm}$ and $T = 120 \text{ K}$), and a supercritical ($p = 90 \text{ atm}$ and $T = 185 \text{ K}$) fluid state. Table 1 lists the thermodynamic critical properties of nitrogen. The compressibility factors, Z , which measure the departure from the ideal-gas behavior, are 0.2, 0.4, and 0.8 at those three different fluid states, respectively. As evidenced Fig. 1b, the present scheme appears to be quite robust, and exhibits an almost identical stability behavior independent of fluid states. The same result is obtained for all flow Mach numbers.

Table 1 Critical properties of nitrogen, methane and oxygen.

	p_c (atm)	T_c (K)	v_c (L/mol)
Nitrogen	34	126	0.089
Methane	46	190	0.099
Oxygen	50	154	0.076

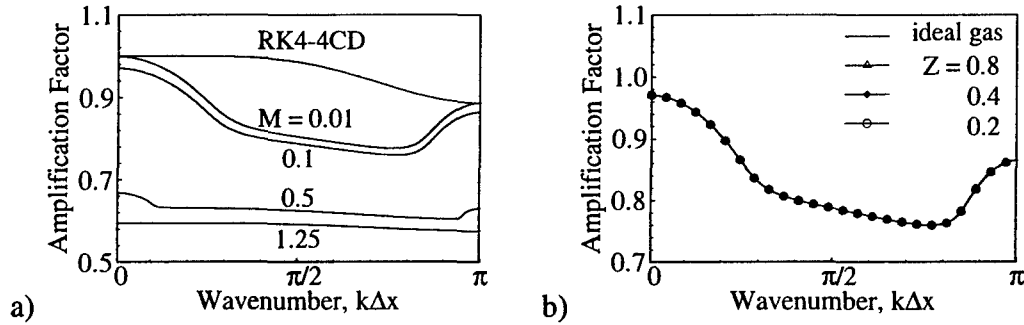


Fig. 1 Amplification factor showing the one-dimensional stability characteristics of the scheme at $CFL = 0.95$, $\Delta\tau/\Delta t = 1$, $\varepsilon_4 = 1/64$, a) ideal gas at $M = 10^{-3}, 10^{-2}, 0.1$, and 1.25 ; and b) compressed nitrogen fluid at $M = 0.1$ and $Z = 0.2, 0.4, 0.8$.

Two-dimensional stability analyses are also conducted for an ideal gas, a cryogenic oxygen fluid ($p = 100 \text{ atm}$ and $T = 100 \text{ K}$), and a supercritical fluid mixture of oxygen and methane ($p = 100 \text{ atm}$, $T = 200 \text{ K}$, and $x_{O_2} = 0.5$) at a flow Mach number of 10^{-3} and a flow angle of 45° (i.e., $v/u = 1$). The compressibility factors for the latter two cases are 0.34 and 0.48, respectively. The amplification factors shown in Fig. 2 indicate that the scheme exhibits an identical stability behavior in a two-dimensional domain, regardless of the fluid state. The result further corroborates the numerical uniformity and self-consistence of the general fluid thermodynamic treatment [15] implemented herein.

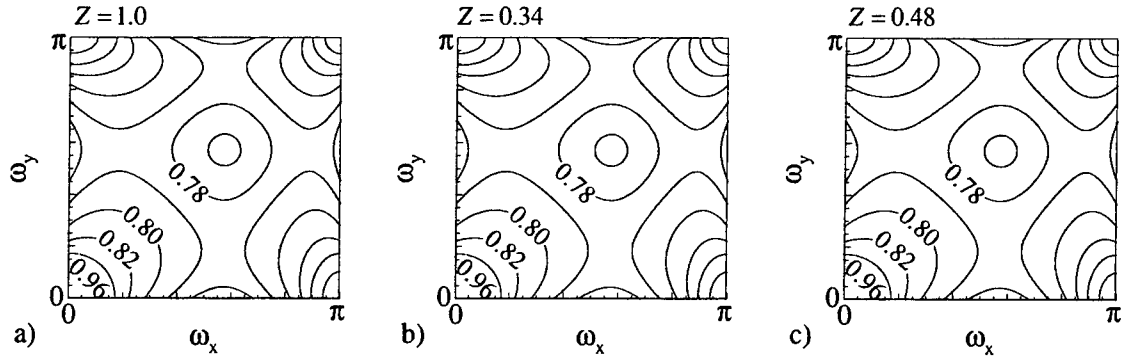


Fig. 2 Amplification factors showing the two-dimensional stability characteristics of the scheme at $M = 10^{-3}$, $CFL = 0.95$, and $\Delta\tau/\Delta t = 1$, a) ideal gas, $Z = 1.0$; b) compressed cryogenic oxygen at 100 K and 100 atm, $Z = 0.34$; c) supercritical oxygen/methane mixture at 200 K, 100 atm, and oxygen mole fraction of 0.5, $Z = 0.48$.

1.5 Sample Calculations

The numerical scheme developed in the preceding sections has been applied to study a wide variety of flow problems in order to assess its accuracy, efficiency, and robustness. This section presents some representative results, including injection of cryogenic fluids and mixing and combustion of coaxial oxygen/methane fluid jets under supercritical conditions. For all the demonstration cases considered herein, turbulence closure is achieved by means of a large-eddy-simulation (LES) technique, in which large-scale motions are calculated explicitly and the effects of unresolved small-scale turbulence are modeled either analytically or empirically. The Favre-filtered mass, momentum, energy, and species conservation equations are derived by filtering small-scale dynamics from resolved scales over a well-defined set of spatial and temporal intervals. The effects of subgrid-scale (sgs) motions are treated using the model proposed by Erlebacher et al. [29]. It employs a Favre-averaged generalization of the Smagorinsky eddy-viscosity model coupled with a gradient-diffusion assumption to simulate sgs energy and species transport processes. The Smagorinsky coefficients C_R (≈ 0.01) and C_I (≈ 0.007) are determined empirically. Thermodynamic properties, such as enthalpy, Gibbs energy, and constant-pressure specific heat, are obtained directly from fundamental thermodynamics theories and a modified Soave-Redlich-Kwong equation of state [27,28]. Transport properties, such as viscosity and thermal conductivity, are evaluated using an extended corresponding-state theory [30,31] along with the 32-term Benedict-Webb-Rubin equation of state [32]. Mass diffusivity is obtained by means of the Takahashi method, calibrated for high pressure conditions [33]. The implementation and validation of the property evaluation schemes were detailed by Yang [1] and Meng et al. [16].

1.5.1 Cryogenic Nitrogen Fluid Jet Dynamics

The first case deals with the injection of cryogenic fluids into supercritical environments. Liquid nitrogen at a temperature of 120 K is injected through a circular tube with a diameter of 254 μm into a supercritical nitrogen environment. A turbulent pipe flow with a bulk velocity of 15 m/s is assumed at the injector exit. The ambient temperature remains at 300 K, but the pressure varies from 69 to 93 atm, which is comparable to the chamber pressures of many operational rocket engines. Two different flow conditions summarized in Table 2 are considered, simulating the experiments conducted by Chehroudi and colleagues [34,35]. The subscripts ∞ and inj denote the

injection and ambient conditions, respectively. The Reynolds number is defined as $Re = \rho_{inj} u_{inj} D_{inj} / \mu_{inj}$.

Table 2 Simulation conditions for injection of liquid nitrogen.

	p_{∞} (MPa)	T_{inj} (K)	T_{∞} (K)	ρ_{inj} (kg/m ³)	ρ_{∞} (kg/m ³)	ρ_{inj}/ρ_{∞}	u_{inj} (m/s)	M_{inj}	Re
Case 1	6.9	120	300	603	77	7.83	15	0.031	44700
Case 2	9.3	120	300	626	103	6.07	15	0.028	42300

The computational domain downstream of the injector measures a length of $40 D_{inj}$ and a diameter of $12 D_{inj}$. The dimensions are sufficient to minimize the effect of the far-field boundary conditions on the near-injector flow evolution. A three-dimensional grid consisting of $225 \times 90 \times 72$ cells is employed. The mean grid size falls roughly in the inertial sub-range of the turbulent kinetic energy (TKE) spectrum, estimated using the Kolmogorov-Obukhov theory. The computational domain is divided into 54 blocks, with each calculated on a single processor of a distributed-memory parallel computer. The physical time step is 1×10^{-3} ms and the maximum CFL number for the inner-loop pseudo-time integration is 0.7. For each case, the calculation is first conducted for an extended period until the flowfield reaches its stationary state. The time stamp is then reset, and data is collected for more than 12 flow-through times (i.e., 15 ms) to obtain statistically meaningful turbulence properties.

Figure 3 shows snapshots of the density-gradient fields at two different ambient pressures of 6.9 and 9.3 MPa. The salient features of supercritical fluid jets are well captured. The fluid state changes continuously from the injected liquid phase to the warmer ambient gas phase with a series of finger- or thread-like entities emerging from the jet surface and dissolving gradually in the surrounding gases. Strong anisotropy of turbulence occurs close to the jet interface, where large

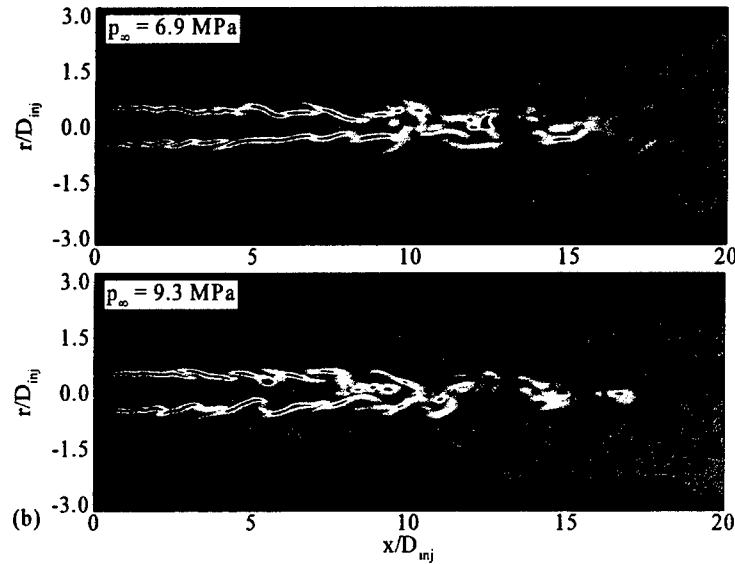


Fig. 3 Effect of pressure on the density-gradient magnitude field ($T_{\infty} = 300$ K, $u_{inj} = 15$ m/s, $T_{inj} = 120$ K, $D_{inj} = 254$ μ m).

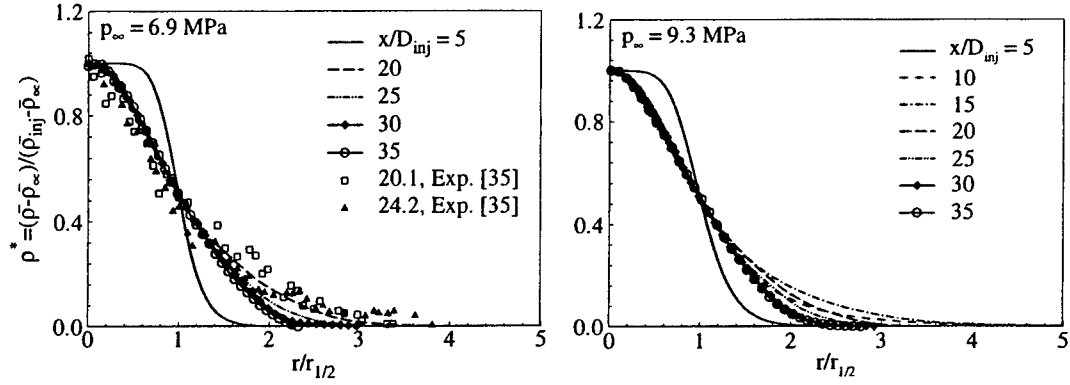


Fig. 4 Radial distributions of normalized density at different axial locations ($T_\infty = 300$ K, $u_{inj} = 15$ m/s, $T_{inj} = 120$ K, $D_{inj} = 254$ μ m).

eddies of integral-length scales become flattened, and the radial component of the TKE is transferred to its axial quantity [36]. Compared with incompressible turbulent jets, both vortex roll-up and pairing are delayed, which leads to a longer potential core, around $8D_{inj}$ for Case 1. The influence of the density stratification decays as the ambient pressure increases. Thus, the location of vortex roll-up shifts upstream from $x/D_{inj} \approx 5$ in Case 1 to $x/D_{inj} \approx 3$ in Case 2, and the jet spreads wider and the length of the potential core reduces to $6-7D_{inj}$ in the latter case.

Figure 4 shows the radial distributions of the normalized mean density, $\rho^+ = (\bar{\rho} - \bar{\rho}_\infty) / (\bar{\rho}_c - \bar{\rho}_\infty)$, at different axial locations. The radial coordinate is normalized by the full width of the radial profile measured where the fluid density is one half of its maximum value (FWHM), $r_{1/2}$, at the axial position of concern. Three distinct flow regimes, similar to incompressible turbulent jets, are identified. The potential core is manifested by the flat-hat distribution near the injector. The density profiles merge into a single distribution farther downstream ($x/D_{inj} > 30$), which suggests the existence of a fully developed self-similarity region. A transition region occurs between 10 and $30D_{inj}$. The experimental data obtained using the Raman scattering technique at the test condition of Case 1 [34,35] is also plotted for comparison. Good agreement between calculations and measurements is achieved with a maximum deviation of 8%.

1.5.2 Supercritical Mixing and Combustion of Oxygen and Methane

The second case treats the flow and flame dynamics of a shear-coaxial injector operating at supercritical conditions, as shown schematically in Fig. 5. Co-flowing methane and oxygen streams are injected through two concentric tubes. The inner diameters of the LOX post and the methane annulus are 3.42 and 5.18 mm, respectively. Fully developed turbulent pipe flows are assumed at the injector exit. In the cold-flow simulations, supercritical oxygen and methane are injected at temperatures of 200 and 300 K, respectively. The bulk velocities of the two streams are 10 and 30 m/s, respectively.

The computational domain extends 40δ downstream of the injector exit with a radius of 12δ , where δ is the thickness of the LOX post. A quasi-axisymmetric simulation involving 360×200 grid points was conducted. The mean grid size of 10 μ m is sufficient to resolve the

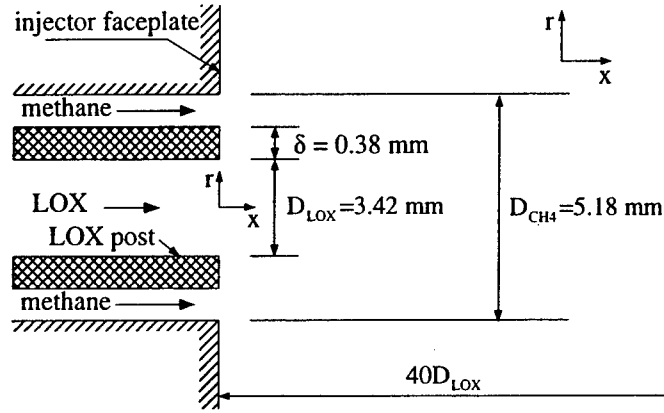


Fig.5 Schematic diagram of shear coaxial injection of oxygen and methane.

inertial sub-range of the TKE spectrum estimated based on the inlet Reynolds number of the oxygen stream. The physical time step is 0.5×10^{-3} ms and the maximum CFL number for the inner-loop pseudo-time integration is 0.7. A more detailed description of the simulation conditions is given in [37].

Figure 6 presents close-up views of the vorticity, temperature, oxygen mass-fraction, and compressibility-factor fields near the injector without chemical reactions. Three shear layers are clearly observed: one emerging from the inner rim of the LOX post; and two from the inner and outer edges of the methane annulus. A series of large scale vortices shed from the outer rim of the LOX post. As those vortices develop, the two shear layers separated by the LOX post merge. Although those energetic eddies concentrate on the light fluid side, they entrain the denser oxygen much deep into the methane stream and greatly facilitate the mixing process.

The situation with chemical reactions is also considered. Liquid oxygen (LOX) and methane are injected at temperatures of 122 and 300 K, respectively. The bulk velocities of the two streams are 13 and 75 m/s, respectively. The mixture and momentum-flux ratios are 3 and 2.5, respectively. The injection conditions are typical of operational liquid-propellant rocket engines. The combustion chamber is preconditioned with a mixture of CO_2 and H_2O at the stoichiometric ratio and 1800 K. The ambient pressure is fixed at 100 atm. A one-step global chemical kinetics model for methane and oxygen is employed [38].

Figure 7 shows snapshots of vorticity, temperature, methane mass-fraction, and compressibility-factor fields. A diffusion-dominated flame emanates immediately from the LOX post and propagates downstream along the surface of the LOX stream. A wake region, which consists of hot combustion products, effectively separates the methane and LOX streams. Similar to the non-reacting flow case, the near-field flow dynamics are characterized by the evolution of the three mixing layers originating from the inner and outer edges of the methane annulus and the inner rim of the LOX post. The evolution of the inner mixing layer of the methane stream, however, is slightly inhibited by the expansion of the combustion products in the flame zone. Because of the strong density stratification between the oxygen stream and flame, the large-scale vortices emerging from the outer rim of the LOX post evolve in a manner analogous to that produced by a backward-facing step and mainly reside on the lighter fluid side. Consequently, the denser oxygen stream is less influenced by those vortices.

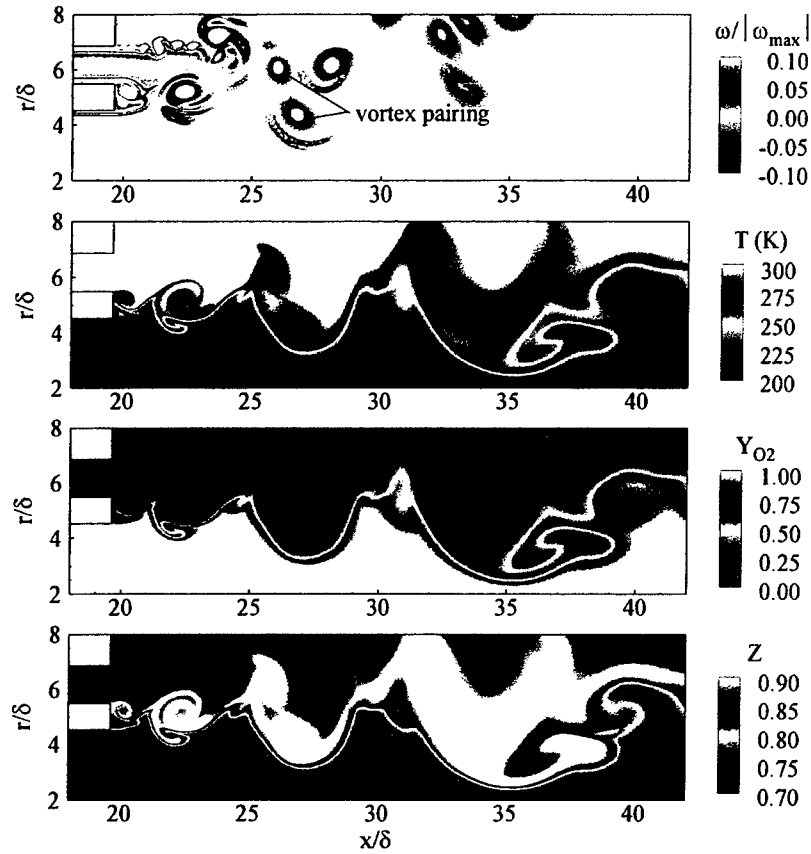


Fig. 6 Snapshots of vorticity, temperature, oxygen mass-fraction, and compressibility-factor fields of shear coaxial injection of oxygen and methane ($p_\infty = 100$ atm, $T_{O_2} = 200$ K, $u_{O_2} = 10$ m/s, $T_{CH_4} = 300$ K, $u_{CH_4} = 30$ m/s).

To assess the numerical performance of the present scheme, calculations are also conducted using the preconditioning scheme developed in [15] for both the non-reacting and reacting flows. The same flow solver described in Section 3 is employed, but with the preconditioning formulation based on the pressure-enthalpy type of primitive variables and a different preconditioning matrix in [15]. The use of enthalpy as one of the dependent variables leads to an iteration solution of the real-fluid equation of state by means of the Newton-Raphson method with a convergence criterion of $|\Delta\rho|/\rho \leq 10^{-6}$ and $|\Delta T|/T \leq 10^{-6}$. A relaxation of this criterion may result in an overflow of the calculation due to strong property variations in the flowfield. Figure 8 compares the convergence histories of computations using the schemes developed in the present study and in [15]. Because the same temporal and spatial discretization techniques are employed, the two schemes exhibit an almost identical behavior of convergence in terms of the number of pseudo-time iterations. The present scheme, however, is much more efficient because it avoids laborious iterations in determining temperature from enthalpy. Table 3 lists the CPU times per pseudo-time iteration, t_{sp} , and the times for solving the equation of state, t_{eos} . All the computations were performed on a Pentium IV 2.4 GHz processor. Less than 5% of the total CPU usage is expended for solving the equation of state with the present scheme, as opposed to more than 50% in the scheme in [15]. The overall computational time is also reduced by half. Another major benefit of the present scheme is that the computational burden for each spatial grid cell is the same because no iterations are

required for solving the equation of state. The load balance among numerical blocks is much easier to achieve on a distributed computing facility.

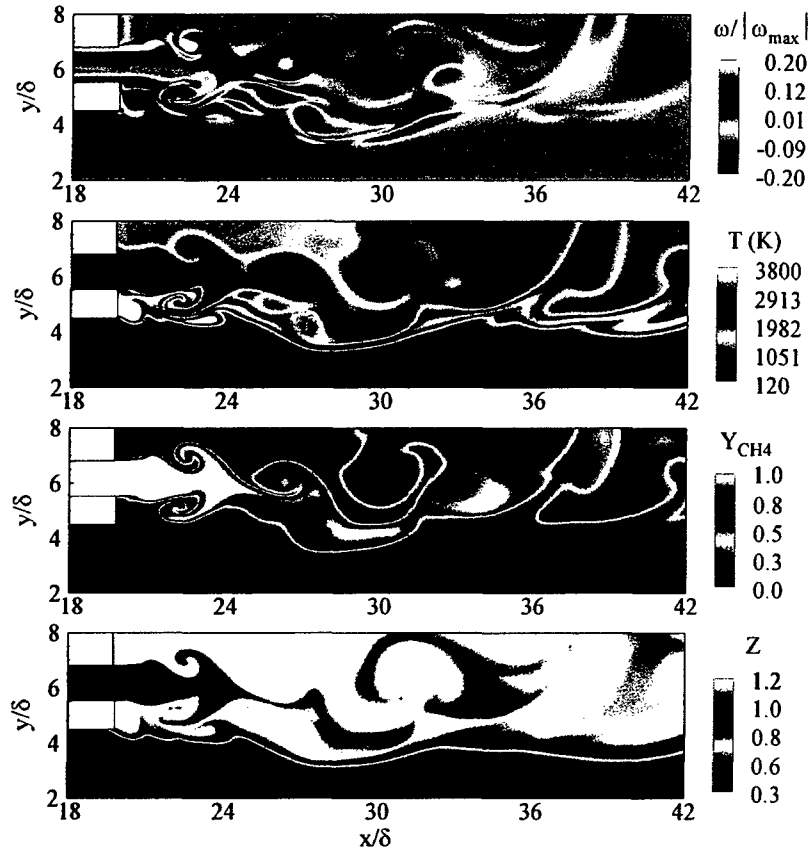


Fig. 7 Snapshots of vorticity, temperature, methane mass-fraction, and compressibility-factor fields near the injector faceplate ($p_\infty = 100$ atm, $T_{O_2} = 122$ K, $u_{O_2} = 13$ m/s, $T_{CH_4} = 300$ K, $u_{CH_4} = 75$ m/s).

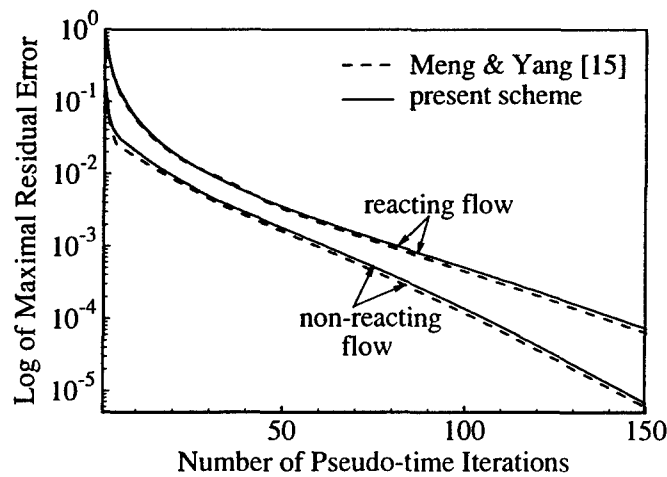


Fig. 8 Convergence histories in the pseudo-time domain for shear coaxial injection and combustion of oxygen and methane.

Table 3 CPU time per iteration in pseudo-time.

	non-reacting flow case			reacting flow case		
	t_{sp} (s)	t_{eos} (s)	t_{eos}/t_{sp}	t_{sp} (s)	t_{eos} (s)	t_{eos}/t_{sp}
Present scheme	52	1.8	3%	87	3.8	4%
Meng & Yang [15]	120	70	58%	158	86	54%

1.6 Conclusions

A general treatment of real-fluid thermodynamics within the framework of a preconditioning scheme has been established. All of the numerical properties are derived directly from fundamental thermodynamics theories based on the concepts of partial-mass and partial-density properties. The algorithm is self-consistent and robust, and can accommodate any equation of state for fluid mixtures. The scheme employs temperature instead of enthalpy as the primary dependent variable in the preconditioned energy equation. As a consequence, the laboriously iterative solution of the equation of state can be avoided. The computational burden is uniform throughout the entire domain. A series of sample calculations, including the injection and combustion of cryogenic fluids under supercritical conditions, were conducted to assess the effectiveness of the scheme at various fluid states. In addition, a numerical stability analysis was performed to characterize the algorithm behavior over a broad range of flow conditions.

Appendix A

The Jacobian matrices, $T \equiv \partial Q / \partial \hat{Q}$, $A \equiv \partial E / \partial \hat{Q}$, $B \equiv \partial F / \partial \hat{Q}$, and $D \equiv \partial S / \partial \hat{Q}$ are derived as:

$$T = \begin{pmatrix} \frac{1}{A_\rho} & 0 & 0 & -\frac{A_T}{A_\rho} & -\frac{A_{Y_1}}{A_\rho} & \dots & -\frac{A_{Y_{N-1}}}{A_\rho} \\ \frac{u}{A_\rho} & \rho & 0 & -\frac{A_T u}{A_\rho} & -\frac{A_{Y_1} u}{A_\rho} & \dots & -\frac{A_{Y_{N-1}} u}{A_\rho} \\ \frac{v}{A_\rho} & 0 & \rho & -\frac{A_T v}{A_\rho} & -\frac{A_{Y_1} v}{A_\rho} & \dots & -\frac{A_{Y_{N-1}} v}{A_\rho} \\ \frac{h_i}{A_\rho} + \left(\sum_{i=1}^N Y_i \bar{e}_i - e - \frac{p}{\rho} \right) \left(\frac{\partial \rho}{\partial p} \right)_{T, Y_i} & \rho u & \rho v & \rho B_T - \frac{A_T e_i}{A_\rho} & \rho B_{Y_1} - \frac{A_{Y_1} e_i}{A_\rho} & \dots & \rho B_{Y_{N-1}} - \frac{A_{Y_{N-1}} e_i}{A_\rho} \\ \frac{Y_1}{A_\rho} & 0 & 0 & -\frac{A_T Y_1}{A_\rho} & \rho - \frac{A_{Y_1} Y_1}{A_\rho} & \dots & -\frac{A_{Y_{N-1}} Y_1}{A_\rho} \\ \vdots & \vdots & \vdots & \vdots & \vdots & \ddots & \vdots \\ \frac{Y_{N-1}}{A_\rho} & 0 & 0 & -\frac{A_T Y_{N-1}}{A_\rho} & -\frac{A_{Y_1} Y_{N-1}}{A_\rho} & \dots & \rho - \frac{A_{Y_{N-1}} Y_{N-1}}{A_\rho} \end{pmatrix} \quad (\text{A.1})$$

$$A = \begin{pmatrix} \frac{u}{A_\rho} & \rho & 0 & -u \frac{A_T}{A_\rho} & -u \frac{A_{Y_1}}{A_\rho} & \dots & -u \frac{A_{Y_{N-1}}}{A_\rho} \\ 1 + \frac{u^2}{A_\rho} & 2\rho u & 0 & -u^2 \frac{A_T}{A_\rho} & -u^2 \frac{A_{Y_1}}{A_\rho} & \dots & -u^2 \frac{A_{Y_{N-1}}}{A_\rho} \\ \frac{uv}{A_\rho} & \rho v & \rho u & -uv \frac{A_T}{A_\rho} & -uv \frac{A_{Y_1}}{A_\rho} & \dots & -uv \frac{A_{Y_{N-1}}}{A_\rho} \\ \frac{u}{A_\rho} [h_i + \left(\sum_{i=1}^N Y_i \bar{e}_i - e - \frac{p}{\rho} \right) + 1] & h_i + \rho u^2 & \rho uv & u(\rho B_T - \frac{A_T e_i}{A_\rho}) & u(\rho B_{Y_1} - \frac{A_{Y_1} e_i}{A_\rho}) & \dots & u(\rho B_{Y_{N-1}} - \frac{A_{Y_{N-1}} e_i}{A_\rho}) \\ \frac{u Y_1}{A_\rho} & \rho Y_1 & 0 & -u \frac{A_T Y_1}{A_\rho} & u(\rho - \frac{A_{Y_1} Y_1}{A_\rho}) & \dots & -u \frac{A_{Y_{N-1}} Y_1}{A_\rho} \\ \vdots & \vdots & \vdots & \vdots & \vdots & \ddots & \vdots \\ \frac{u Y_{N-1}}{A_\rho} & \rho Y_{N-1} & 0 & -u \frac{A_T Y_{N-1}}{A_\rho} & -u \frac{A_{Y_1} Y_{N-1}}{A_\rho} & \dots & u(\rho - \frac{A_{Y_{N-1}} Y_{N-1}}{A_\rho}) \end{pmatrix} \quad (\text{A.2})$$

$$B = \begin{pmatrix} \frac{v}{A_\rho} & 0 & \rho & -v \frac{A_T}{A_\rho} & -v \frac{A_{Y_1}}{A_\rho} & \dots & -v \frac{A_{Y_{N-1}}}{A_\rho} \\ \frac{uv}{A_\rho} & \rho v & \rho u & -uv \frac{A_T}{A_\rho} & -uv \frac{A_{Y_1}}{A_\rho} & \dots & -uv \frac{A_{Y_{N-1}}}{A_\rho} \\ 1 + \frac{v^2}{A_\rho} & 0 & 2\rho v & -v^2 \frac{A_T}{A_\rho} & -v^2 \frac{A_{Y_1}}{A_\rho} & \dots & -v^2 \frac{A_{Y_{N-1}}}{A_\rho} \\ \frac{v}{A_\rho} [h_i + (\sum_{i=1}^N Y_i \tilde{e}_i - e - \frac{p}{\rho}) + 1] & \rho uv & h_i + \rho v^2 & v(\rho B_T - \frac{A_T e_i}{A_\rho}) & v(\rho B_{Y_1} - \frac{A_{Y_1} e_i}{A_\rho}) & \dots & v(\rho B_{Y_{N-1}} - \frac{A_{Y_{N-1}} e_i}{A_\rho}) \\ \frac{v Y_1}{A_\rho} & 0 & \rho Y_1 & -v \frac{A_T Y_1}{A_\rho} & v(\rho - \frac{A_{Y_1} Y_1}{A_\rho}) & \dots & -v \frac{A_{Y_{N-1}} Y_1}{A_\rho} \\ \vdots & \vdots & \vdots & \vdots & \vdots & \ddots & \vdots \\ \frac{v Y_{N-1}}{A_\rho} & 0 & \rho Y_{N-1} & -v \frac{A_T Y_{N-1}}{A_\rho} & -v \frac{A_{Y_1} Y_{N-1}}{A_\rho} & \dots & v(\rho - \frac{A_{Y_{N-1}} Y_{N-1}}{A_\rho}) \end{pmatrix} \quad (\text{A.3})$$

$$D = \begin{pmatrix} 0 & 0 & 0 & 0 & \dots & 0 \\ 0 & 0 & 0 & 0 & \dots & 0 \\ 0 & 0 & 0 & 0 & \dots & 0 \\ 0 & 0 & 0 & 0 & \dots & 0 \\ (\frac{\partial \dot{\omega}_1}{\partial p})_{T, Y_i} & 0 & 0 & (\frac{\partial \dot{\omega}_1}{\partial T})_{p, Y_i} & (\frac{\partial \dot{\omega}_1}{\partial Y_1})_{p, T, Y_{j \neq 1}} & \vdots & (\frac{\partial \dot{\omega}_1}{\partial Y_{N-1}})_{p, T, Y_{j \neq N-1}} \\ \vdots & \vdots & \vdots & \vdots & \vdots & \ddots & \vdots \\ (\frac{\partial \dot{\omega}_{N-1}}{\partial p})_{T, Y_i} & 0 & 0 & (\frac{\partial \dot{\omega}_{N-1}}{\partial T})_{p, Y_i} & (\frac{\partial \dot{\omega}_{N-1}}{\partial Y_1})_{p, T, Y_{j \neq 1}} & \dots & (\frac{\partial \dot{\omega}_{N-1}}{\partial Y_{N-1}})_{p, T, Y_{j \neq N-1}} \end{pmatrix} \quad (\text{A.4})$$

Reference:

- [1] V. Yang, Modeling of supercritical vaporization, mixing, and combustion processes in liquid-fueled propulsion systems, *Proc. Combust. Inst.* 28 (2000) 925-942.
- [2] C.L. Merkle, J.Y., Sullivan, P.E.O. Buelow, S. Venkateswaran, Computation of flows with arbitrary equation of state, *AIAA. J.* 36 (1998) 515-521.
- [3] E. Turkel, Preconditioned methods for solving the incompressible and low speed compressible equations, *J. Comput. Phys.* 72 (1987) 277-298.
- [4] J. S. Shuen, K.H. Chen, Y.H. Choi, A coupled implicit method for chemical non-equilibrium flows at all speeds, *J. Comput. Phys.* 106 (1993) 306-318.
- [5] Y.H. Choi, C.L. Merkle, The application of preconditioning to viscous flows, *J. Comput. Phys.* 105 (1993) 207-223.
- [6] J.M. Weiss, W.A. Smith, Preconditioning applied to variable and constant density flows, *AIAA J.* 33 (1995) 2050-2057.
- [7] D. Darmofal, B. Van Leer, Local preconditioning: manipulating mother nature to fool father time, *Computing the Future II: advances and prospects in computational aerodynamics*, edited by M. Hafez and D. Caughey, Wiley, New York, 1998.
- [8] E. Turkel, Proconditioning techniques in computational fluid dynamics, *Annu. Rev. Fluid Mech.* 31 (1999) 385-416.
- [9] J.R. Edwards, R.K. Franklin, M.S. Liou, Low-diffusion flux-splitting methods for real fluid flows with phase transitions, *AIAA J.* 38 (2000) 1624-1633.
- [10] J.R. Edwards, M.S. Liou, "Low-diffusion flux-splitting scheme for flows at all speeds," *AIAA J.* 36 (1998) 1610-1617.
- [11] D. Mao, J.R. Edwards, A. V., Kuznetsov, R. K., Srivastava, Development of low-diffusion flux-splitting methods for dense gas-solid flows, *J. Comput. Phys.* 185 (2003) 100-119.
- [12] J.C. Oefelein, V. Yang, Modeling high-pressure mixing and combustion processes in liquid rocket engines, *J. Prop. Power* 14 (1998) 843-857.
- [13] S.Y. Hsieh, V. Yang, A preconditioned flux-differencing scheme for chemically reacting flows at all Mach numbers, *Int. J. Comput. Fluid Dyn.* 8 (1997) 31-49.
- [14] Oefelein, J.C., Mixing and combustion of cryogenic oxygen-hydrogen shear-coaxial jet flames at supercritical pressure, *Combust. Sci. Tech.*, 178 (2006) 229-252.
- [15] H. Meng, V. Yang, A unified treatment of general fluid thermodynamics and its application to a preconditioning scheme, *J. Comput. Phys.* 189 (2003) 277-304.
- [16] H. Meng, G.C. Hsiao, V. Yang, J.S. Shuen, Transport and dynamics of liquid oxygen droplets in supercritical hydrogen streams, *J. Fluid Mech.* 527 (2005) 115-139.
- [17] A. Jameson, The evolution of computational methods in aerodynamics, *J. of Applied Mathematics* 50 (1983) 1052-1070.
- [18] M.M. Rai, S. Chakravarthy, Conservative high-order accurate finite difference methods for curvilinear grids, *AIAA Paper No.* 1993-3380.
- [19] E. Turkel, Robust low speed preconditioning for viscous high lift flows, *AIAA Paper No.* 2002-0962.
- [20] E. Turkel, V.N. Vatsa, Choice of variables and preconditioning for time dependent problems, *AIAA paper No.* 2003-3692.
- [21] M.J. Moran, H.N. Shapiro, *Fundamentals of Engineering Thermodynamics*, 4th ed., John Wiley & Sons, Inc., New York (1999).

- [22] S. Venkateswaran, C.L. Merkle, X. Zeng, D. Li, Influence of large-scale pressure changes on preconditioned solutions at low speeds, *AIAA J.* 42 (2004) 2490-2498.
- [23] H. Guillard, C. Viozat, On the behavior of upwind scheme in the low Mach number limit, *Computer and Fluids* 28 (1999) 63-86.
- [24] P.E.O. Buelow, S. Venkateswaran, C.L. Merkle, Effect of grid aspect ratio on convergence, *AIAA J.* 32 (1994) 2401-2408.
- [25] R.C. Swanson, E. Turkel, On central difference and upwind schemes, *J. Comput. Phys.* 101 (1992) 292-306.
- [26] P. Jorgenson, E. Turkel, Central difference TVD schemes for time dependent and steady state problems, *J. Comput. Phys.* 107 (1993) 297-308.
- [27] M.S. Graboski, T.E. Daubert, A modified Soave equation of state for phase equilibrium calculation, 1. hydrocarbon systems, *Ind. Eng. Chem. Proc. Design Dev.* 17 (1978) 448-454.
- [28] M.S. Graboski, T.E. Daubert, A modified Soave equation of state for phase equilibrium calculation, 1. systems containing hydrogen, *Ind. Eng. Chem. Proc. Design Dev.* 18 (1979) 300-305.
- [29] G. Erlebacher, M. Y. Hussaini, C. G. Speziale, T. A. Zang, Toward the large eddy simulation of compressible turbulent flows, *J. Fluid Mech.* 238 (1992) 155-185.
- [30] J.F. Ely, H.J. Hanley, Prediction of transport properties. 1. Viscosity of fluids and mixtures, *Ind. Eng. Chem. Fundamentals* 20 (1981) 323-332.
- [31] J.F. Ely, H.J. Hanley, Prediction of transport properties. 2. Thermal conductivity of pure fluids and mixtures, *Ind. Eng. Chem. Fundamentals* 22 (1983) 90-97.
- [32] R.T. Jacobsen, R.B. Stewart, Thermodynamic properties of nitrogen including liquid and vapor phases from 63K to 2000K with pressure to 10,000 bar, *J. Phys. Chem. Ref. Data* (1973) 2 757-922.
- [33] S. Takahashi, Preparation of a generalized chart for diffusion coefficients of gases at high pressures, *J. Chem. Eng (Japan)* (1974) 7 417-420.
- [34] B. Chehroudi, D. Talley, E. Coy, Visual characteristics and initial growth rates of round cryogenic jets at subcritical and supercritical pressures, *Phys. Fluids* 14 (2002) 850-861.
- [35] B. Chehroudi, R. Cohn, D. Talley, A. Badakhshan, Cryogenic shear layers: experiments and phenomenological modeling of the initial growth rate under subcritical and supercritical conditions, *Int. J. Heat Fluid Flow* 23 (2002) 554-563.
- [36] N. Zong, H. Meng, S.Y. Hsieh, V. Yang, A numerical study of cryogenic fluid injection and mixing under supercritical conditions, *Phys. Fluids* 16 (2004) 4248-4261.
- [37] N. Zong, V. Yang, Cryogenic jets and mixing layers in transcritical and supercritical environments, *Combust. Sci. Tech.* 178 (2006) 193-227.
- [38] C.K. Westbrook, F.L. Dryer, Simplified reaction for the oxidation of hydrocarbon fuels in flames, *Combust. Sci. Tech.* 27 (1981) 31-43.

Task 2

Cryogenic Propellant Injection and Mixing at Supercritical Conditions

This work treats cryogenic propellant injection and mixing at near-critical and super-critical conditions under conditions with and without transverse acoustic excitations, simulating the experiments conducted by Chehroudi and Talley at the Air Force Research Laboratory. The purposes are to achieve an improved understanding of high-pressure cryogenic fluid jet dynamics, and to further validate the code outlined in the subtask 1. The analysis accommodates full conservation laws and real-fluid thermodynamics and transport over the entire temperature and pressure regimes of concern. Turbulence closure is achieved using a large-eddy-simulation (LES) technique, in which large energy-carrying structures are computed explicitly and the effects of small-scale motions on resolved scales are modeled. A Smagorinsky model extended to compressible flows is used to treat small-scale motions. Thermodynamic properties, including enthalpy, internal energy, and heat capacity, are directly calculated by means of fundamental thermodynamic theories and a modified Soave-Redlich-Kwong (SRK) equation. Transport properties, such as viscosity and thermal conductivity, are estimated with an extended corresponding-state principle. Mass diffusivity is obtained by the Takahashi method calibrated for high-pressure conditions. Numerical implementation includes a preconditioning scheme in conjunction with a dual time-stepping integration algorithm. Further efficiency is achieved by utilizing a parallel computational scheme that involves the message-passing-interface (MPI) library and a multi-block treatment. Results from this task have led to one archival journal publication as follows.

“A Numerical Study of Cryogenic Fluid Injection and Mixing under Supercritical Conditions,” by N. Zong, H. Meng, S.Y. Hsieh, and V. Yang, *Physics of Fluids*, Vol. 16, 2004, pp. 4248-4261.

2.1 Introduction

Injection of liquid fluid initially at a subcritical temperature into an environment in which the temperature and pressure exceed the thermodynamic critical point of the injected fluid is an important phenomenon in many high-pressure combustion devices, including diesel, gas-turbine, and liquid-propellant rocket engines. Under these conditions, fluid jets exhibit many characteristics distinct from their counterparts at low pressures. First, because of the diminishment of surface tension and enthalpy of vaporization, the sharp distinction between the liquid and gas phases vanishes. The fluid properties and their spatial gradients vary continuously throughout the entire field. Second, thermodynamic and transport anomalies may occur during the temperature transition across the critical value, especially when the pressure approaches the critical point, a phenomenon commonly referred to as near-critical enhancement [1]. As a result, compressibility effects (i.e., volumetric changes induced by pressure variations) and variable inertial effects (i.e., volumetric changes induced by heat addition and/or variable composition) play an important role in dictating the flow evolution. Third, the characteristic times of the flow motions around the jet boundary have the same order of magnitude at supercritical conditions. The resultant coupling dynamics becomes transient in both the jet interior and the surrounding fluid, and involves an array of physiochemical processes with widely disparate time and length scales. Fourth, the flow Reynolds number increases almost linearly with pressure. For oxygen and hydrogen, an increase in pressure from 1 to 100 atmospheres results in a reduction of the corresponding kinematic viscosity by a factor of two orders of magnitude. Based on the Kolmogorov universal equilibrium theory, the Kolmogorov and

variable-density, single-phase turbulent submerged jet at both subcritical and supercritical pressures, when the ambient temperature remained supercritical.

Motivated by the development of high-pressure cryogenic-propellant rocket engines, extensive experimental studies have recently been conducted to provide direct insight into supercritical fluid injection and mixing. The work included injection of liquid nitrogen and co-injection of liquid nitrogen and gaseous helium into gaseous nitrogen environments over a wide range of pressure [8-10]. Cryogenic propellants such as liquid oxygen and hydrogen under both cold-flow and hot-fire test conditions were also considered. Results from the shadowgraph images confirmed the findings by Newman and Brzustowski [7]. Drastic changes in jet surface phenomena took place across the critical pressure. Ligaments and droplets formed at subcritical pressures, but disappeared at supercritical conditions due to the prevalence of turbulent motions and vanishment of surface tension. The jet surface topology bears a strong resemblance to its gaseous counterpart, with the spatial growth rate following that of an incompressible variable-density gaseous jet [10]. The spontaneous Raman Scattering technique was employed to measure the density field [11,12]. In general, the normalized density profiles indicated a tendency towards the self-similarity solution observed for classical constant- and variable-density single-phase fluid jets at low pressures. The effects of acoustic waves on cryogenic nitrogen jet flow development were recently studied by Chehroudi and Talley[13]. The influence was substantial at subcritical conditions, but became unnoticeable at supercritical conditions. The phenomenon may be attributed to the formation of high-frequency vortices in the supercritical jet flow.

In parallel to experimental studies, attempts were made both theoretically and numerically to explore the underlying mechanisms of high-pressure fluid injection and mixing. Oefelein and Yang [2] modeled two-dimensional mixing and combustion of oxygen and hydrogen streams at supercritical conditions by means of a large-eddy-simulation technique. The formulation accommodated real-fluid thermodynamics and transport phenomena. All the thermophysical properties were evaluated directly from fundamental thermodynamics theories over the entire regime of fluid states of concern. Furthermore, a unified treatment of numerical algorithms based on general fluid thermodynamics was established to improve computational accuracy and efficiency[3,14]. Bellan and colleagues [15,16,17] treated the temporal evolution of heptane/nitrogen and oxygen/hydrogen mixing layers at supercritical conditions. Several important characteristics of high-pressure transitional mixing processes were identified. In particular, as a result of density stratification, the mixing layer is considerably more stable than a corresponding gaseous mixing layer. Energy dissipation due to both the species-flux and heat-flux effects prevails during the evolution of the mixing layer, whereas the viscous effect appears minimal.

The purpose of the present work is to conduct a comprehensive analysis of cryogenic fluid injection and mixing under supercritical conditions. The theoretical formulation accommodates full conservation laws and real-fluid thermodynamics and transport phenomena. Turbulence closure is achieved using a large-eddy-simulation technique. As a specific example, the dynamics of a cryogenic nitrogen jet in a supercritical nitrogen environment is studied over a wide range of pressure. The work focuses on the near-field jet dynamics and its subsequent evolution.

2.2 Theoretical Formulation

A unified theoretical framework capable of treating fluid flows, trans-critical property variations and real-fluid thermodynamics is developed. Turbulence closure is achieved using a large-eddy-simulation (LES) technique, in which large-scale motions are calculated explicitly and

the effects of unresolved small-scale turbulence are modeled either analytically or empirically. Thermodynamic properties such as enthalpy, Gibbs energy, and constant-pressure specific heat are obtained directly from fundamental thermodynamics theories [3,14] Transport properties are evaluated using an extended corresponding-state theory along with the 32-term Benedict-Webb-Rubin equation of state [3].

2.2.1 Governing Equations

The formulation is based on the Favre-filtered conservation equations of mass, momentum and energy. These equations are derived by filtering the small-scale dynamics from the resolved scales over a well-defined set of spatial and temporal intervals. They can be conveniently expressed in the following Cartesian tensor form:

$$\frac{\partial \bar{\rho}}{\partial t} + \frac{\partial \bar{\rho} \tilde{u}_j}{\partial x_j} = 0 \quad (1)$$

$$\frac{\partial \bar{\rho} \tilde{u}_i}{\partial t} + \frac{\partial (\bar{\rho} \tilde{u}_i \tilde{u}_j + \bar{p} \delta_{ij})}{\partial x_j} = \frac{\partial (\bar{\tau}_{ij} - \tau_{ij}^{sgs})}{\partial x_j} \quad (2)$$

$$\frac{\partial \bar{\rho} \tilde{E}}{\partial t} + \frac{\partial ((\bar{\rho} \tilde{E} + \bar{p}) \tilde{u}_i)}{\partial x_i} = \frac{\partial}{\partial x_i} (\tilde{u}_j \bar{q}_i + \bar{q}_i - H_i^{sgs} + \sigma_{ij}^{sgs}) \quad (3)$$

where overbars and tildes denote resolved-scale and Favre-averaged resolved-scale variables, respectively. ρ , u_i , p , E , τ_{ij} and q_i represent the density, velocity components, pressure, specific total energy, viscous stress tensor, heat flux, respectively. A detailed derivation of the filtered equations is presented by Oefelein and Yang [2]. The unclosed subgrid-scale (*sgs*) terms in Eqs. (1) - (3), including the stresses τ_{ij}^{sgs} , energy fluxes H_i^{sgs} and viscous work σ_{ij}^{sgs} , are defined as

$$\tau_{ij}^{sgs} = (\overline{\rho u_i u_j} - \bar{\rho} \tilde{u}_i \tilde{u}_j) \quad (4)$$

$$H_i^{sgs} = (\overline{\rho E u_i} - \bar{\rho} \tilde{E} \tilde{u}_i) + (\overline{p u_i} - \bar{p} \tilde{u}_i) \quad (5)$$

$$\sigma_{ij}^{sgs} = (\overline{u_j \tau_{ij}} - \tilde{u}_j \tilde{\tau}_{ij}) \quad (6)$$

The unclosed *sgs* stress term is modeled using the compressible flow version of the Smagorinsky model suggested by Erlebacher et al. [18]

$$\tau_{ij}^{sgs} = -2\nu_t \bar{\rho} (\tilde{S}_{ij} - \tilde{S}_{kk} \delta_{ij} / 3) + \frac{2}{3} \bar{\rho} k^{sgs} \delta_{ij} \quad (7)$$

where

$$\nu_t = C_R \Delta^2 (2\tilde{S}_{ij} \tilde{S}_{ij})^{1/2} \quad (8)$$

$$k^{sgs} = C_I \Delta^2 (2\tilde{S}_{ij} \tilde{S}_{ij}) \quad (9)$$

The dimensionless constants C_R (≈ 0.01) and C_I (≈ 0.007) are determined empirically, $k^{sgs} = \tau_{kk}^{sgs} / 2\bar{\rho} = (\overline{\rho u_k u_k} / \bar{\rho} - \tilde{u}_k \tilde{u}_k) / 2$ and $\tilde{S}_{ij} = (\partial \tilde{u}_i / \partial x_j + \partial \tilde{u}_j / \partial x_i) / 2$. The symbol Δ denotes the filter width. The subgrid energy flux term H_i^{sgs} is modeled as

$$H_i^{sgs} = -\bar{\rho} \frac{\nu_t}{Pr_t} \left(\frac{\partial \tilde{h}}{\partial x_j} + \tilde{u}_i \frac{\partial \tilde{u}_i}{\partial x_j} + \frac{1}{2} \frac{\partial k^{sgs}}{\partial x_j} \right) \quad (10)$$

A standard value of 0.7 is used for the turbulent Prandtl number. The unclosed subgrid viscous-work term σ_{ij}^{sgs} is assumed to be small and is neglected in the present study.

2.2.2 Thermodynamic and Transport Properties

Owing to the continuous variations of fluid properties throughout the jet and surroundings under supercritical conditions, conventional treatment of fluid jets at low pressures in which the liquid and gas phases are solved separately and then matched at the interfaces often leads to erroneous results. The problem becomes even more exacerbated when the fluid approaches its critical state, around which fluid properties exhibit anomalous sensitivities with respect to local temperature and pressure variations. Thus, a prerequisite of any realistic treatment of supercritical fluid behavior lies in the establishment of a unified property evaluation scheme valid over the entire thermodynamic regime [3,14].

The formulation established here can accommodate any equation of state. In the present work, a modified Soave-Redlick-Kwong (SRK) equation of state is adopted because of its wide range of validity and ease of implementation [19]. It takes the following form,

$$p = \frac{\rho R_u T}{W - b\rho} - \frac{a\alpha}{W} \frac{\rho^2}{(W + b\rho)} \quad (11)$$

where R_u is the universal gas constant. The parameters a and b account for the effects of attractive and repulsive forces between molecules, respectively. The third parameter α includes the critical compressibility factor and acentric (size-shape) interactions between molecules.

Thermodynamic properties, such as enthalpy, internal energy, and constant- pressure specific heat, can be expressed as the sums of ideal-gas properties at the same temperature and departure functions taking into account the dense-fluid correction [3]. Thus,

$$e(T, \rho) = e_0(T) + \int_{p_0}^p \left[\frac{p}{\rho^2} - \frac{T}{\rho^2} \left(\frac{\partial p}{\partial T} \right)_\rho \right] d\rho \quad (12)$$

$$h(T, p) = h_0(T) + \int_{p_0}^p \left[\frac{1}{\rho} + \frac{T}{\rho^2} \left(\frac{\partial \rho}{\partial T} \right)_p \right] dp \quad (13)$$

$$C_p(T, \rho) = C_{v0}(T) - \int_{p_0}^p \left[\frac{T}{\rho^2} \left(\frac{\partial^2 p}{\partial T^2} \right)_\rho \right] d\rho + \frac{T}{\rho^2} \left(\frac{\partial p}{\partial T} \right)_\rho^2 / \left(\frac{\partial p}{\partial \rho} \right)_T \quad (14)$$

The subscript 0 refers to the ideal state at low pressure. The departure functions on the right-hand sides of equations (12)-(14) can be determined from the equation of state.

Transport properties including viscosity and thermal conductivity are estimated by means of the corresponding state principles along with the use of the 32-term Benedict-Webb-Rubin(BWR) equation of state [20,21]. Figure 2 shows the effects of temperature on the compressibility factor, specific heat, viscosity, and thermal conductivity of nitrogen in the temperature range of 40–1000 K at five different pressures of 1, 10, 33.4, 100, 200 atmospheres. These figures illustrate key trends over the range of pressure and temperature of interest. At 750 K and above, nitrogen exhibits ideal gas behavior and the pressure effect is negligible. As the temperature decreases below 750 K, however, significant non-idealities are introduced with strong pressure dependence. The implementation and validation of the property evaluation schemes were discussed in Ref. [3]. It should be noted that the present scheme does not consider the critical enhancement in the close vicinity of the critical point, a region known as the critical region proper where a scaled equation of state must be used [22]. Thus, the thermophysical properties shown in Fig. 2 do not diverge at the critical point as predicted by classical theories. Since the simulation conditions chosen herein deviate considerably from the critical point, the neglect of critical divergence exerts no influence on the solution accuracy.

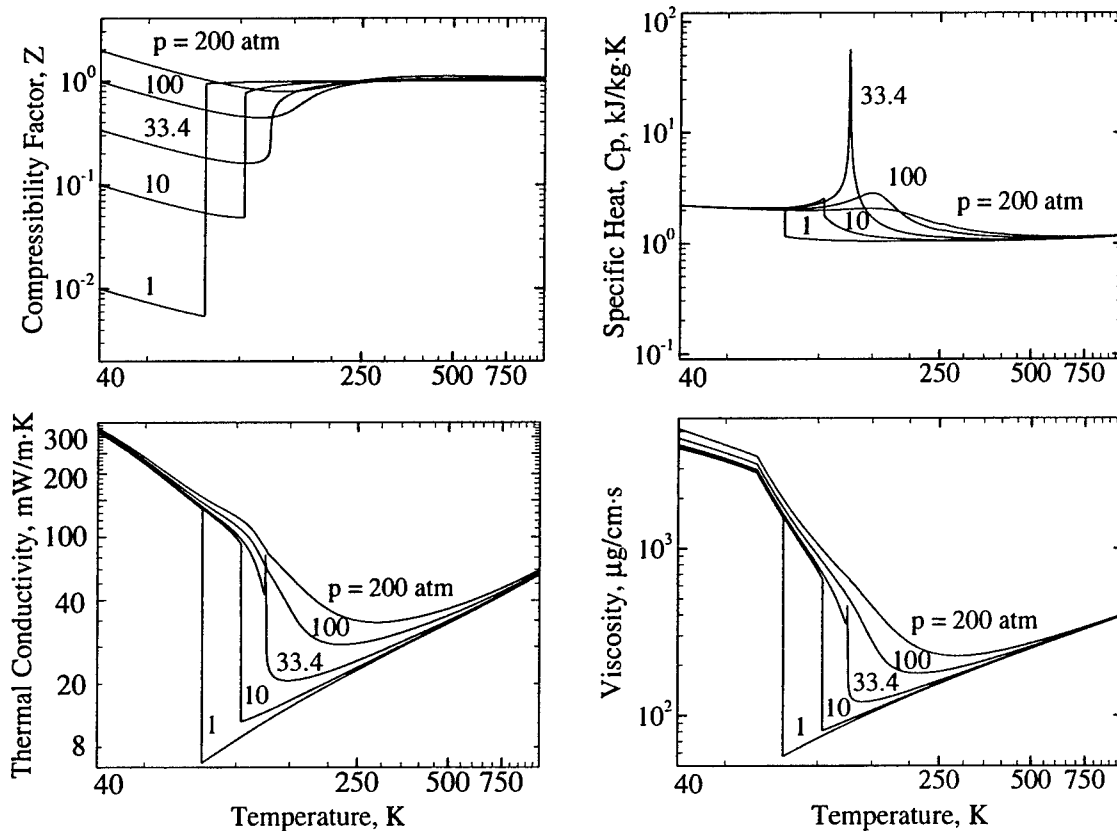


Fig.2 Thermo-physical properties of nitrogen as functions of pressure and temperature.

2.3 Numerical Method

The present work bears two severe numerical challenges. First, thermodynamic non-idealities and transport anomalies take place as the fluid transits through the transcritical regime. Thus, treating these phenomena in a manner consistent with the intrinsic characteristics of a numerical algorithm presents a major obstacle. Second, the rapid variation of fluid state and wide disparities in the characteristic time and length scales pose the well-known stiffness problem. A unified treatment of general fluid thermodynamics is developed to circumvent those difficulties. The method is based on the concepts of partial-mass and partial-density properties [14], and valid for the entire pressure and temperature regimes of concern. The resultant routine is incorporated into a preconditioning scheme along with a dual time-step integration algorithm to handle compressible fluid flows at all speeds [23,24]. Since all of the numerical relations, including the Jacobian matrices and eigenvalues, are derived directly from fundamental thermodynamics theories, the algorithm is self-consistent and robust. A detailed description of the overall approach was given by Meng and Yang [14].

The theoretical formulation outlined above is solved by means of a density-based, finite volume methodology. The spatial discretization employs a fourth-order, central-difference scheme in generalized coordinates. A fourth-order scalar dissipation with a total-variation-diminishing switch developed by Swanson and Turkel [25] is implemented to ensure computational stability and to prevent numerical oscillations in regions with steep gradients. Temporal discretization is obtained using a second-order backward difference, and the inner-loop pseudo-time term is integrated with a three-step third-order Runge-Kutta scheme. A multiblock domain decomposition technique, along with static load balance, is employed to facilitate the implementation of parallel computation with message passing interfaces at the domain boundaries.

2.4 Computational Domain and Grid System

The physical model of concern is shown schematically in Fig. 1, simulating the experiments described in Refs. [10] and [12]. Cryogenic nitrogen fluid is injected into supercritical gaseous nitrogen through a circular duct with an inner diameter of 0.254 mm. Because of the enormous computational effort required for calculating the flowfield in the entire three-dimensional regime, only a cylindrical sector with periodic boundary conditions specified in the azimuthal direction is treated herein. The analysis, in spite of the lack of vortex-stretching mechanism, has been shown to be able to capture the salient features of supercritical fluid jet evolution [26].

The computational domain downstream of the injector measures a length of $40 D_{inj}$ and a radius of $6 D_{inj}$. The dimensions are sufficient to minimize the effect of the far-field boundary conditions on the near-injector flow evolution. The entire grid system consists 225×90 points along the axial and radial directions, respectively. The grids are clustered in the shear layer and near the injector to resolve rapid property variations in those regions. The mean grid size in the near field ($0 \leq x/D_{inj} \leq 20$) falls in the inertial sub-range of the turbulent kinetic energy spectrum, estimated using the Kolmogorov-Obukhov theory. The smallest grid width is $2 \mu\text{m}$. The computational domain is divided into 45 blocks, with each calculated on a single processor of a distributed-memory parallel computer. The physical time step is 1×10^{-3} ms and the maximum CFL number for the inner-loop pseudo-time integration is 0.7. For each case, simulation was conducted for 12 flow-through times (i.e., 15 ms) to obtain statistically meaningful data.

A grid independence study was performed as part of the validation procedure, in which the same numerical code, configuration, and flow condition (i.e. Case 1 in Table 1) were considered with two different grid resolutions: a fine (270×120) and a coarse (225×90) mesh. Figure 3 shows the radial distributions of the mean axial velocity, turbulent kinetic energy (TKE), compressibility factor Z , and viscosity (normalized by the value of the ambient gas) at different axial locations. Results from the two different grid systems agree well with each other, except for the small deviation of TKE.

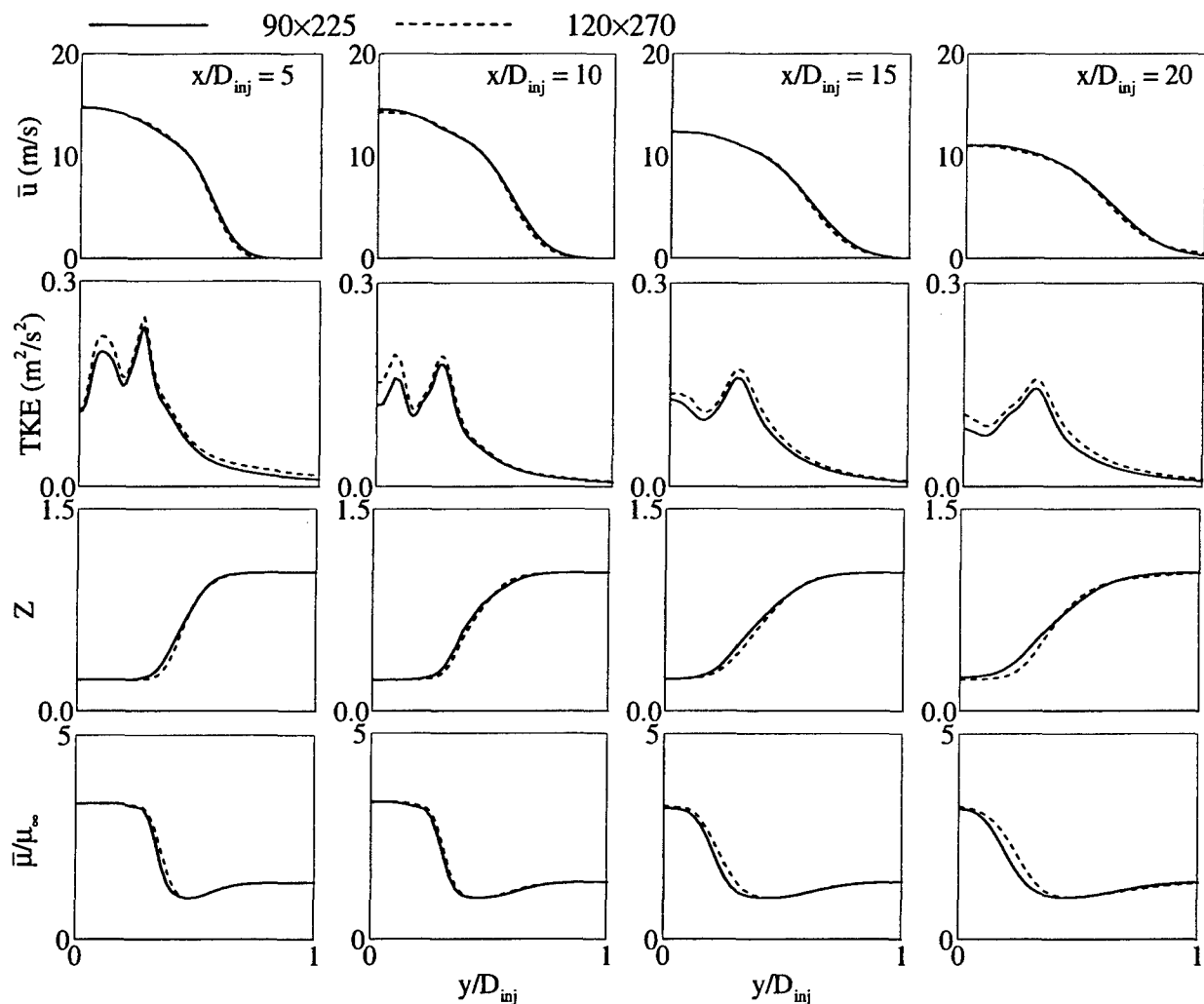


Fig.3 Effect of grid resolution on radial distributions of mean axial velocity, turbulent kinetic energy, compressibility factor, and viscosity at different axial locations ($p_{\infty} = 4.3$ MPa, $T_{\infty} = 300$ K, $u_{inj} = 15$ m/s, $T_{inj} = 120$ K, $D_{inj} = 254$ μ m)

2.5 Boundary Condition

At the injector exit, a fully developed turbulent pipe flow is assumed. The mean velocity follows the one-seventh-power law and the temperature is specified with a top-hat profile. The pressure is determined using a one-dimensional approximation to the momentum equation in the axial direction. Turbulence is provided by superimposing broad-band white noise onto the mean velocity profile. The disturbances are generated by a Gaussian random-number generator with an intensity of 12% of the mean quantity. At the downstream boundary, extrapolation of primitive

variables from the interior may cause undesired reflection of waves propagating into the computational domain. Thus, the non-reflecting boundary conditions proposed by Poinso and Lele [27] are applied, along with the specification of a reference pressure. Because the jet flow is directly exhausted to an ambient condition, the surrounding fluid may be entrained into the computational domain. At the radial boundary, the pressure, temperature, and axial velocity are specified. The conservation law of mass is employed to determine the radial velocity. Finally, the non-slip adiabatic conditions are enforced along the solid walls.

2.6 Results and Discussions

The theoretical model and numerical scheme established in the preceding sections were implemented to study the injection and mixing of cryogenic fluid under supercritical conditions. As a specific example, liquid nitrogen at a temperature of 120 K is injected through a circular tube with a diameter of 254 μm into a supercritical nitrogen environment. A turbulent pipe flow with a bulk velocity of 15 m/s is assumed at the injector exit. The ambient temperature remains at 300 K, but the pressure varies from 42 to 93 atm, comparable to the chamber pressures of many operational rocket engines. For reference, the critical temperature and pressure of nitrogen are 126 K and 34 atm, respectively. Three different flow conditions summarized in Table 1 are considered, simulating the experiments conducted by Chehroudi and Talley [10], where the subscripts ∞ and inj denote the injection and ambient conditions, respectively. The Reynolds number is defined as $Re = \rho_{inj} u_{inj} D_{inj} / \mu_{inj}$.

Table 1 Simulation Conditions

	Case 1	Case 2	Case 3
P_{∞} (MPa)	4.3	6.9	9.3
T_{∞} (K)	300	300	300
ρ_{∞}	46	77	103
T_{inj} (K)	120	120	120
ρ_{inj}	563	603	626
u_{inj} (m/s)	15	15	15
ρ_{inj}/ρ_{∞}	12.24	7.83	6.07
Re	48500	44700	42300

Figure 4 shows the variations of nitrogen density and constant-pressure specific heat as functions of temperature at four different pressures. Two observations are noted here. First, the density decreases sharply near the critical point as the temperature increases. The effect of density stratification between the jet and the ambient fluid becomes much more substantial for $p_{\infty} = 4.3 \text{ MPa}$ compared with the other two cases. Second, the temperature sensitivity of the specific heat depends strongly on pressure. It increases rapidly as the fluid state approaches the critical point, and theoretically becomes infinite exactly at the critical point. This implies that much more thermal energy is needed to heat up the cold fluid jet in Case 1 (i.e., $p_{\infty} = 4.3 \text{ MPa}$) than the other two cases when the fluid temperature transits across the near-critical regime. The anomalous variations of fluid volumetric and thermal properties near the critical point and their dependence on pressure have profound influences on fluid jet development at high pressures.

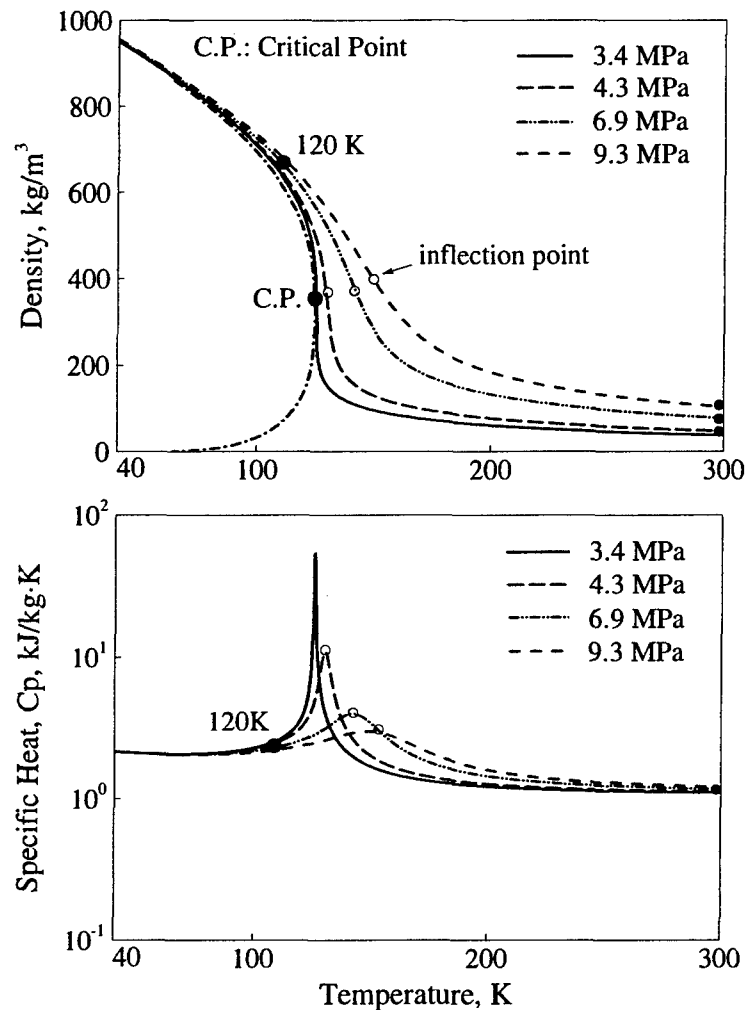


Fig.4 Density and constant-pressure specific heat of nitrogen as the functions of temperature and pressure.

2.6.1 Instantaneous Flowfield

For a constant-density jet, the shear layer between the jet and the ambient fluid is susceptible to the Kelvin-Helmholtz instability and experiences vortex rolling, pairing, and breakup. A cryogenic supercritical jet undergoes qualitatively the same process, but with additional mechanisms arising from volume dilation and baroclinic torque.

Figure 5 shows snapshots of the density, density-gradient, temperature, and vorticity-magnitude fields at three different ambient pressures. The small vortical structures in the core region result from the imposed turbulent motions at the injector exit. For Case 1, in which the ambient pressure of 4.3 MPa is closer to the critical value, the jet surface is straight near the injector with only tiny instability waves in the downstream region. As the ambient pressure increases, the velocity fluctuation in the radial direction becomes more vigorous. Large-scale instability waves develop in the near-injector region, which then grow up and roll into a succession of ring vortices as the injected fluid moves downstream. The resultant vortical flow motions facilitate the entrainment of the ambient gaseous nitrogen into the cold jet fluid. The initial density-stratification layer is only slightly stretched in Case 1, but severely twisted in higher-pressure cases. As a general trend, the

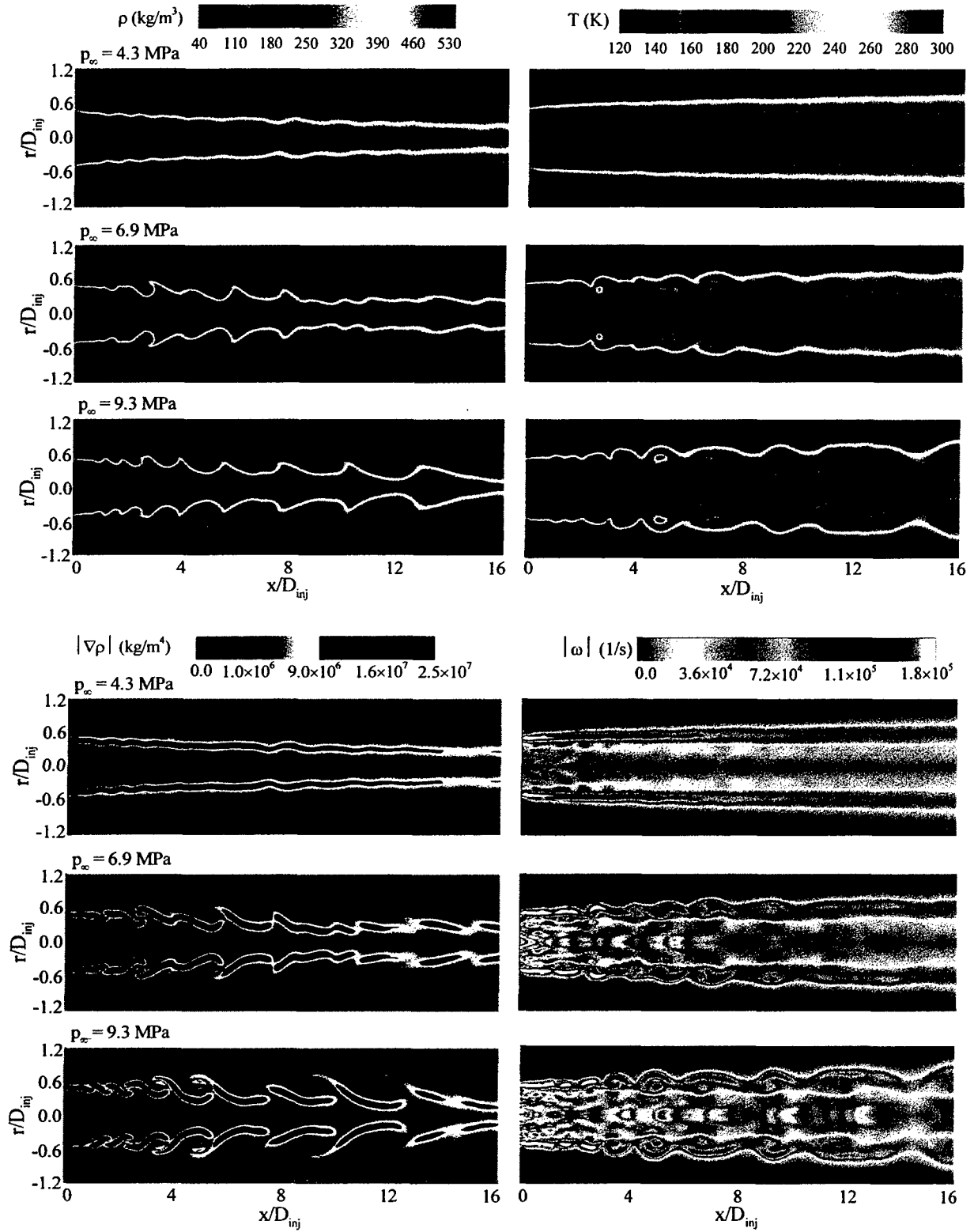


Fig.5 Effect of pressure on density, density gradient, temperature and vorticity fields ($T_\infty = 300$ K, $u_{inj} = 15$ m/s, $T_{inj} = 120$ K, $D_{inj} = 254$ μm , $t = 1.55$ ms).

higher the ambient pressure, the stronger vortical motions and radial velocity fluctuations near the jet surface.

It has been established [28] that the evolution and interaction of large coherent structures strongly influence the mixing and entrainment of a shear layer. Figure 6 shows the temporal evolution of the jet surface structures of Case 3 ($p_\infty = 9.3 \text{ MPa}$). Both the temperature and density fields clearly demonstrate the entrainment of lighter and warmer ambient gaseous nitrogen into the jet flow through vortical motions, along with a series of thread-like entities emerging from the jet surface. The same phenomena were observed in the experiments by Chehroudi and co-works under the same flow condition [10].

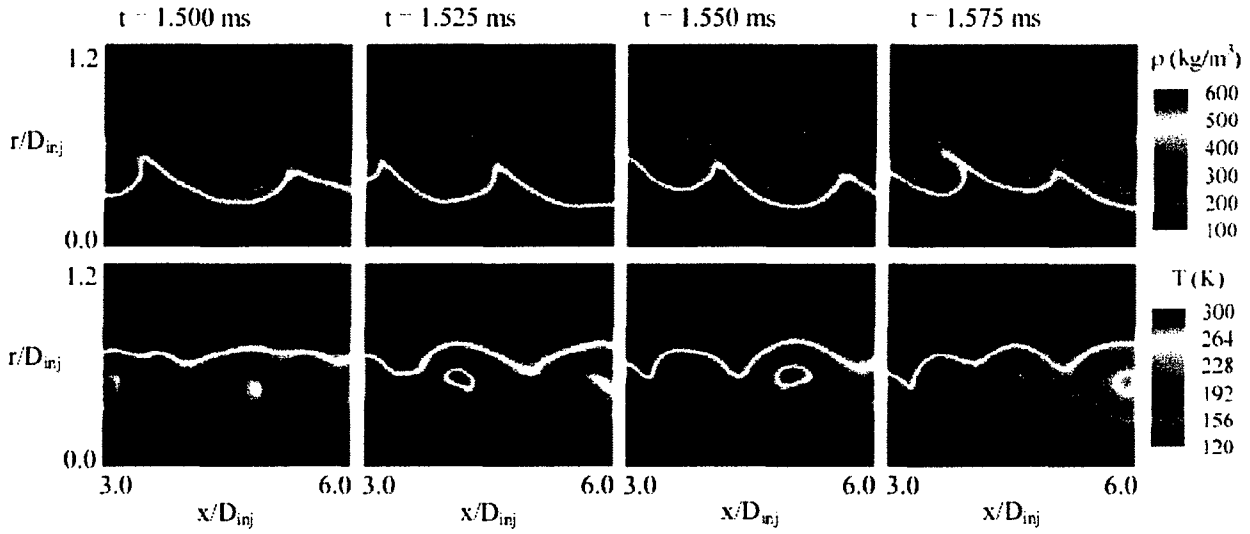


Fig.6 Time evolution of jet surface structures ($p_\infty = 9.3 \text{ MPa}$, $T_\infty = 300 \text{ K}$, $u_{inj} = 15 \text{ m/s}$, $T_{inj} = 120 \text{ K}$, $D_{inj} = 254 \text{ } \mu\text{m}$).

2.6.2 Effect of Density Stratification

To explore the formation and influence of the density-stratification layer near the jet boundary, conditional-averaged temperatures over the regions where the density-gradient magnitudes exceed pre-specified cutoff values are determined. The result is listed in Table 2, where $|\nabla \rho|_{\max}$ is the maximum density gradient in the entire field, around $1.15 \times 10^7 \text{ kg/m}^4$ for Case 3. The conditional fluid temperature decreases with increasing cutoff density gradient, and approaches the inflection point on the isobaric $\rho - T$ curve shown in Fig. 4. Table 3 summarizes the inflection temperatures for the three different pressures considered herein. It is noteworthy that fluid properties usually undergo rapid variations across the temperature inflection point for an isobaric process, and the specific heat reaches its maximum at this point. For example, the density of nitrogen decreases more than three times in Case 1 as the temperature increases from 125 to 135 K. Thus, the formation of the steep density-gradient region is closely related to property variations, which to a large extent are dictated by real-fluid thermodynamics. Turbulent diffusion and mixing tend to introduce warm ambient gases into the cold jet, and subsequently smooth the density-stratification effect. The drastic volume dilation during the mixing process when the temperature

Table 2 Conditional averaged temperatures (K) in regions with $|\nabla\rho| > \text{cutoff value}$.

Cutoff	Case 1	Case 2	Case 3
$0.1 \cdot \nabla\rho _{\max}$	131.7	151.0	158.0
$0.2 \cdot \nabla\rho _{\max}$	131.1	148.0	154.0
$0.3 \cdot \nabla\rho _{\max}$	130.6	145.5	151.3

Table 3 Temperatures at inflection points on isobaric $\rho - T$ curves at different pressures

	Case 1	Case 2	Case 3
p_{∞} (MPa)	4.3	6.9	9.3
T (K)	130.3	142.1	148.6

transits across the inflection point, however, prevents the entrainment of the surrounding fluid, and thereby facilitates the formation of steep density-gradient regimes.

The effect of density stratification on the evolution of a planar mixing layer was studied by Atsavapranee and Gharib [29]. Because the higher density stratification increasingly inhibits instability-wave growth and vortex paring, the flow topography is considerably simplified, as evidenced in Fig. 5. In addition, the total yield of mixed fluid is reduced with high density stratification due to the combined effect of weakened fluid entrainment into the Kelvin-Helmholtz vortices, decreased frequency of vortex paring, and arrest of turbulence during flow restratification.

Figure 7 shows the power spectral densities (PSD) of the axial and radial velocity fluctuations at various radial locations of $r/D_{inj} = 0.6, 0.7$, and 0.8 in the mixing layer for $p_{\infty} = 9.3 \text{ MPa}$. The axial position of $x/D_{inj} = 16$ is near the end of the potential core, where a sharp density gradient exists at $r = 0.1 D_{inj}$ (see Fig. 5). In the low-frequency regime, in which large-scale structures prevail, the axial velocity fluctuation increases as the density stratification layer is approached. The trend for the radial velocity fluctuation, however, is opposite. The velocity fluctuations in the high-frequency range remain basically insensitive to the radial position. Density stratification exerts a strong influence on large-scale flow motions. It acts like a solid wall in the flow that amplifies the axial turbulent fluctuation but damps the radial one. The same PSD results are also observed for Cases 1 and 2, which are not presented here.

A similar phenomenon was reported by Hannoun et al. [30] in their experiments on grid-induced shear-free turbulence near a sharp density interface. As a consequence of the strong anisotropy of the turbulence near the density interface, large eddies of integral length scales become flattened, and the vertical component of the turbulent kinetic energy is transferred to its horizontal quantity. Such an energy redistribution among its spatial components considerably modifies the amount of energy available for fluid mixing at the density interface. Thus, the existence of strong density stratification suppresses radial velocity fluctuations in the flowfield and inhibits the development of instability waves. In the present study, the initial density ratio and the strength of density stratification decrease as the ambient pressure increases, so do their damping effects on the shear layers. The jet surface is nearly straight in Case 1, with only tiny instability waves developing in the downstream region. The shear layers, however, are highly twisted in both Cases 2 and 3, as shown in Fig. 5.

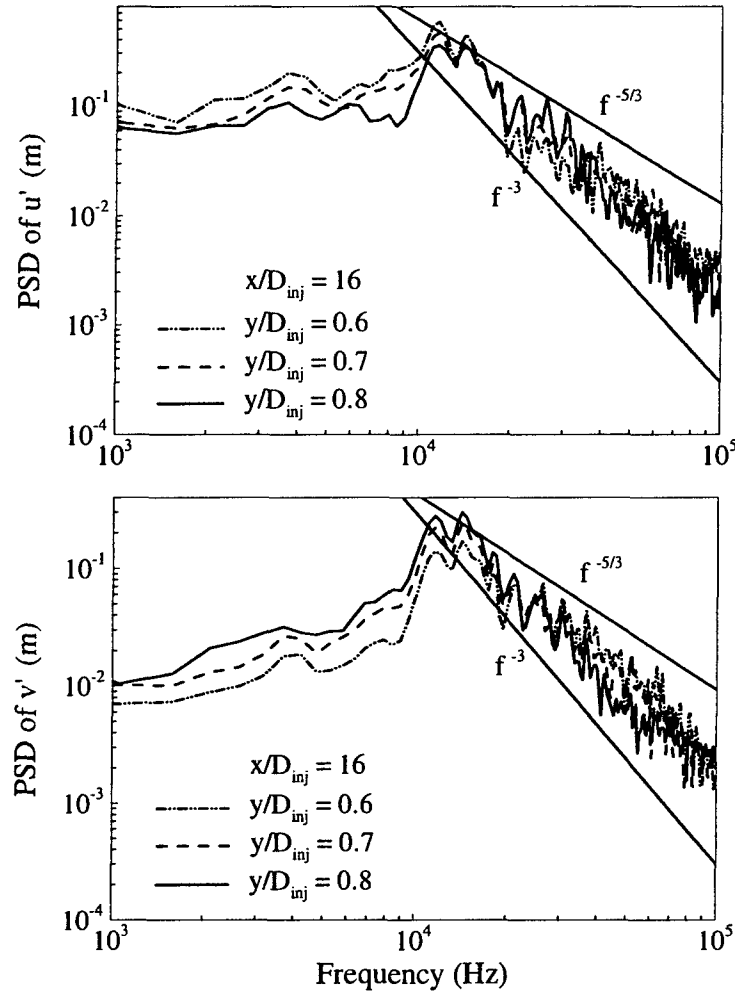


Fig.7 Power spectral densities of velocity fluctuations at different radial locations with $x/D_{inj} = 16$ ($p_{\infty} = 9.3$ MPa, $T_{\infty} = 300$ K, $u_{inj} = 15$ m/s, $T_{inj} = 120$ K, $D_{inj} = 254$ μ m).

The frequency spectra of velocity fluctuations shown in Fig. 7 do not indicate the standard $5/3$ law for the turbulent kinetic energy spectrum based on the Kolmogorov theory, which characterizes the inertial subrange. Apte and Yang [31] mentioned in their two-dimensional simulations of unsteady flow evolution in a porous-walled chamber that the exponent of the wave number in the inertial subrange of the turbulent energy spectrum varies between f^{-3} and f^{-4} , with f being the frequency. Gilbert [32] proposed that the kinetic energy spectrum can be obtained from spiral vortex distributions within coherent vortices and should follow the $f^{-11/3}$ law. In this work, the frequency dependence in the inertial subrange lies between $f^{-5/3}$ and f^{-3} .

The present two-dimensional large-eddy simulation inherently neglects the vortex stretching mechanism, which is responsible for the transfer of energy from large to small scales through energy cascade and the continuous generation of small-scale vortical structures. Since these structures redistribute and dissipate energy at the smallest scales, the lack of vortex stretching leads to lower energy-dissipation and turbulence-production rates during the flow evolution. This issue will be addressed in subsequent three-dimensional calculations.

2.6.3 Shear-Layer Instability

To study the vortical dynamics and flow instability in the mixing layer, the power spectral densities of the radial velocity oscillations at two different axial locations are presented in Fig. 8. The radial position is fixed at $r/D_{inj} = 0.5$. A dominant frequency around 35 kHz, corresponding to the most amplified frequency of the shear layer instability, is observed at an upstream location of $x/D_{inj} = 8$ for both Cases 2 and 3. This frequency is weakly dependent on the ambient pressure (or the density ratio). When the fluid is convected downstream to $x/D_{inj} = 18$, the dominant frequency decreases to 15.9 kHz for Case 2 and 18.6 kHz for Case 3, nearly one half of the value of the most amplified shear instability mode. The vortex pairing process is clearly demonstrated. The situation with Case 1, however, is considerably different. Owing to the low compressibility factor (i.e. 0.21)

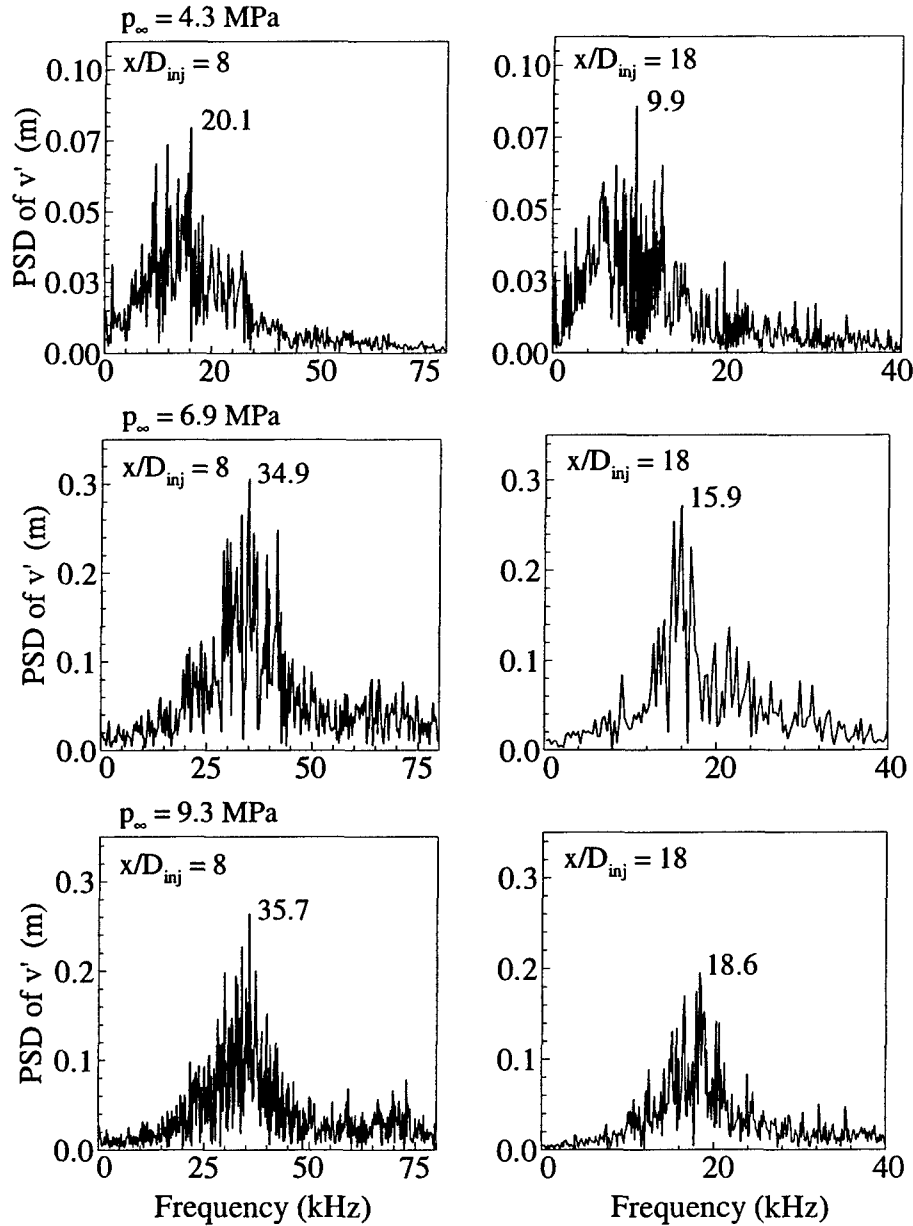


Fig.8 Effect of pressure on power spectral densities of radial velocity fluctuations at two different axial locations with $r/D_{inj} = 0.5$.

of the injected fluid and the large density ratio of 12.24, the jet exhibits a liquid-like fluid behavior distinct from the other high-pressure cases. The dominant frequencies become 20 and 10 kHz at $x/D_{inj} = 8$ and 18, respectively.

The flow instabilities and vortex shedding in constant-density shear layers were reviewed by Schadow and Gutmark [33]. Based on their work, the initial vortex shedding frequency, f_1 , can be scaled with the shear-layer momentum thickness θ_0 and a characteristic velocity \bar{U} , normally taken as the average bulk velocity of the two streams. The result yields a non-dimensional frequency or Strouhal number, $St_i = f_i \theta_0 / \bar{U}$, which ranges from 0.044 to 0.048 for a planar turbulent shear layer. As the vortices move downstream, they merge together to oscillate at the sub-harmonics of the initial vortex shedding frequency, f_1 / N ($N = 2, 3, 4, \dots$). Although the above analysis was formulated for planar flows, it can be applied with good accuracy to mixing layers in axisymmetric configurations if the thickness of the shear layer is much smaller than the radius of the injector. In the present work, $\bar{U} \approx 8 \text{ m/s}$ and the initial momentum thickness θ_0 estimated for a fully developed turbulent pipe flow is 0.011 mm. If the strouhal number is chosen to be $St_i = 0.048$, then the most amplified frequency becomes $f_1 = 34.9 \text{ kHz}$ and the corresponding second harmonic frequency is 17.5 kHz. Those values agree well with the calculated vortex-shedding frequencies based on the radial velocity oscillations in Cases 2 and 3.

To provide more insight into observed flow phenomena, a linear stability analysis is carried out of the effects of ambient pressure on the fluid jet evolution. The work extends the approaches described in Refs. [34] and [35] to include real-fluid thermodynamics. The SRK equation of state is implemented in the formulation. Each dependent variable is decomposed into a base and a perturbation quantity. The former is adopted directly from the present simulation. The latter takes the following general form for a planar jet.

$$\hat{\phi}(x, y, t) = \phi(y) \exp\{i(kx - \omega t)\} \quad (15)$$

where k and ω are the wave number and frequency, respectively. For a spatial instability problem, k is a complex variable and its negative imaginary part represents the spatial growth rate. After substitution of the decomposed variables into the conservation laws and linearization of the result, a dispersion equation characterizing the relationship between the wave number and frequency can be derived in terms of pressure fluctuation as follow.

$$\frac{d^2 \hat{p}}{dy^2} - \left(\frac{1}{\bar{\rho}} \cdot \frac{d\bar{\rho}}{dy} + \frac{2}{\bar{u} - \omega/k} \frac{d\bar{u}}{dy} \right) \frac{d\hat{p}}{dy} - k^2 \hat{p} = 0 \quad (16)$$

The problem now becomes solving Eq. (16) for the eigenvalues k and ω subject to appropriate boundary conditions. A complete discussion of the stability analysis is given in Ref. [36].

Figure 9 shows the spatial growth rates of the instability waves as a function of the normalized frequency (i.e., the Strouhal number) for the three different pressures considered in the present study. The growth rate of the shear wave decreases with increasing pressure. The strong density stratification in the lower pressure case suppresses the growth of the wave and stabilizes the mixing layer. The theoretically predicted frequencies of the most unstable oscillations are 23.2,

28.8 and 29.6 KHz for Cases 1, 2, and 3, respectively. These values are slightly underestimated for Cases 2 and 3, but overestimated for Case 1. The maximum deviation from the numerical simulation is 15%. The frequency of the most unstable mode exhibits a weak pressure dependence at high pressures. It, however, decreases significantly in the near-critical regime due to the enhanced effect of density stratification and increased mixing-layer momentum thickness.

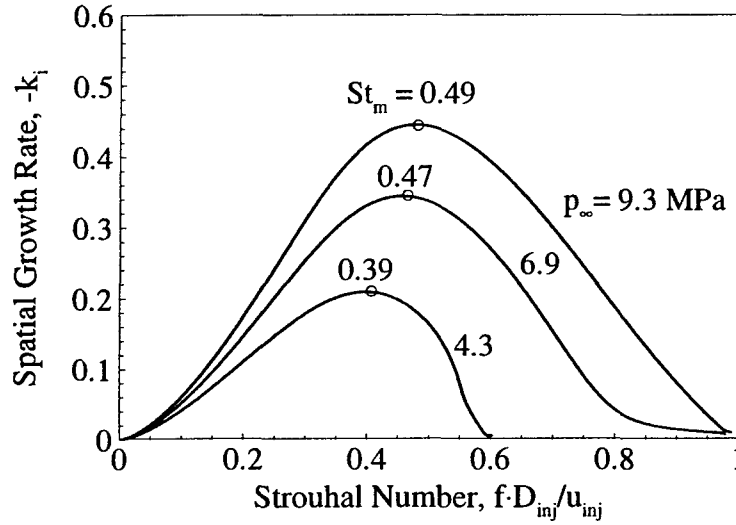


Fig.9 Spatial growth rate as function of Strouhal number at different pressures.

2.6.4 Vortical Dynamics

As a consequence of the large velocity difference between the jet and ambient flow, a strong shear layer is generated near the injector, which is then tilted and develops to large structures due to vortex interactions. The vortical dynamics can be best quantified using the transport equation given below.

$$\frac{D\omega}{Dt} = (\omega \cdot \nabla)u - (\nabla \cdot u)\omega - \nabla \left(\frac{1}{\rho} \right) \times \nabla p + \nabla \times \left(\frac{1}{\rho} \nabla \cdot \tau \right) \quad (17)$$

where D/Dt stands for the substantial derivative. The first term on the right-hand side represents vortex stretching, which vanishes in the present two-dimensional simulation. The second term describes the volume-dilatation effect, and the third term denotes the baroclinic torque produced by the misalignment between the pressure and density gradients. The last term arises from viscous dissipation. For cryogenic fluid injection under supercritical conditions, large volume expansion occurs when the jet is heated by the ambient gas. Thus, both baroclinic torque and volume dilatation may play an important role in determining vorticity transport.

Figure 10 shows an instantaneous azimuthal vorticity budget in the radial direction at the axial position of $x/D_{inj} = 5$ for all the three cases. At this position, the large coherent structures are well developed in Cases 2 and 3. The results are normalized by the bulk velocity (u_{inj}) and momentum thickness (θ_0) at the injector exit. The baroclinic torque and viscous dissipation locally rival in magnitude, and have opposite contributions in equation (17). These two terms attain their maxima in regions with large density gradients in which vigorous mixing between the jet and

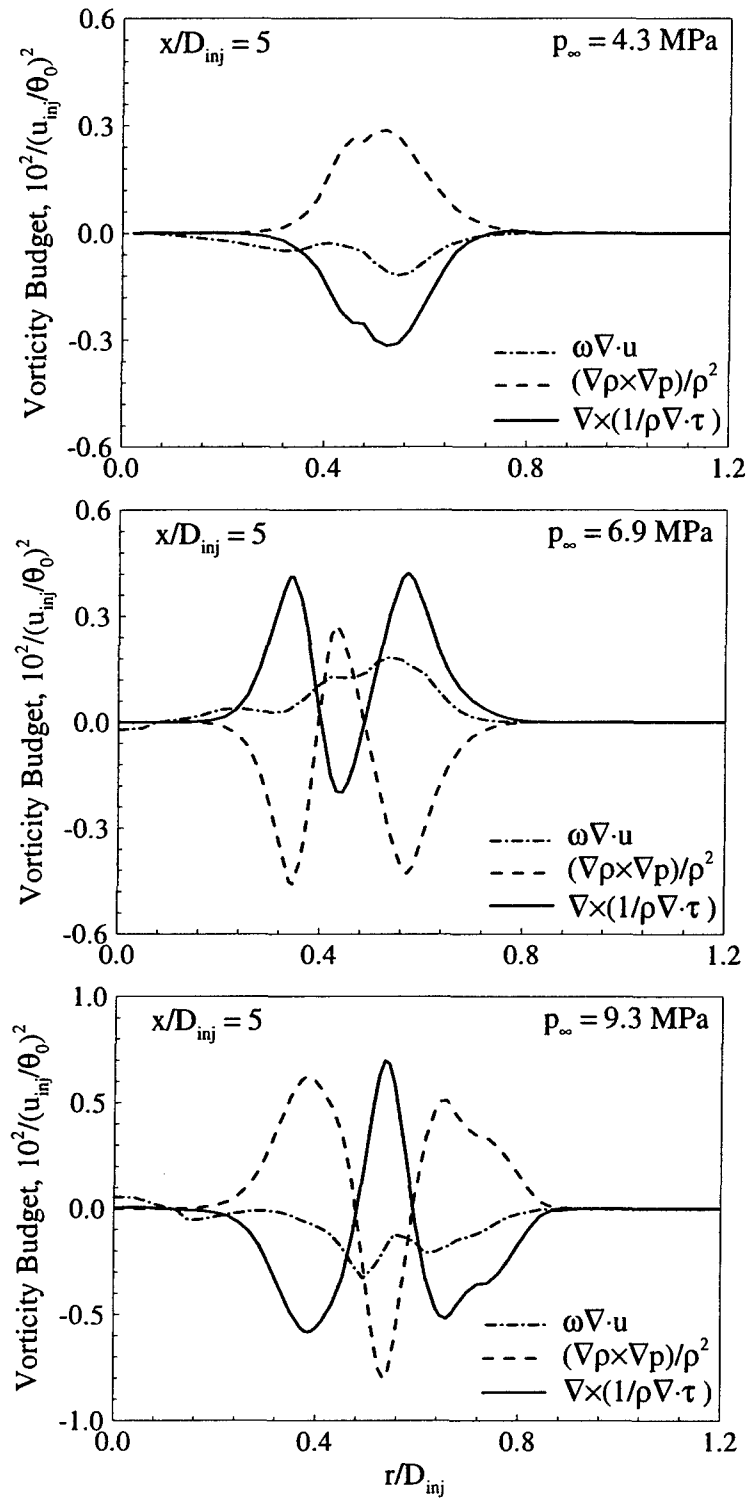


Fig.10 Vorticity budgets at different ambient pressures ($T_\infty=300$ K, $u_{inj}=15$ m/s, $T_{inj}=120$ K, $D_{inj}=254$ μ m, $t=1.55$ ms).

ambient flows occurs (see Fig. 5). In Case 1, much of the vorticity production takes place on the light fluid side. A similar phenomenon was noted by Okong'o and Bellan in their study of a supercritical binary mixing layer.¹⁵ As the ambient pressure increases (or the density ratio

decreases), the location with intensive vorticity production slightly shifts toward the dense fluid, but still resides on the ambient gas side, since the radial position of the mixing region also changes. The magnitudes of all the three vorticity production terms increase with increasing ambient pressure due to strengthened vortical motions.

2.6.5 Mean Flow Properties

The mean flow properties are obtained by taking long-time average of the instantaneous quantities over 10 ms (about 8 flow-through times) after the calculated flowfield has reached its stationary state. Figure 11 shows the radial distributions of the normalized mean density, $\rho^+ = (\bar{\rho} - \bar{\rho}_\infty) / (\bar{\rho}_c - \bar{\rho}_\infty)$, at six different axial locations. The subscript c refers to the quantity at the centerline. The radial coordinate is normalized by the full width of the radial profile measured where the flow property of concern (i.e., density in the present figure) is one half of its maximum value (FWHM), $r_{1/2}$. Similar to incompressible fluid jets, there exist three distinct regions in a cryogenic fluid jet under supercritical conditions: a potential core in the upstream where a flat-hat distribution around the centerline occurs, a transition region, and a fully developed self-similar region. The density profiles at $x/D_{inj} > 25$ merge to a single distribution for Cases 2 and 3, manifesting the existence of self-similarity in the downstream region. Such a self-similar profile, however, is not observed until $x/D_{inj} > 30$ for Case 1. The high-pressure condition facilitates the development of the self-similar behavior through its effect on reducing the density ratio of the injected fluid to the ambient flow. Figure 12 shows the comparison with the density field measured by Chehroudi and Talley [12] using the Raman scattering technique under the same condition of Case 2 ($p_\infty = 6.9 \text{ MPa}$). The calculated and measured radial distributions follow exactly the same trend at the two positions. The maximum deviation is 5%.

Figure 13 shows the normalized axial velocity profiles in the radial direction. Self-similarity is achieved at the same location as that for the density distribution. It occurs at a relatively upstream position as the ambient pressure increases. Compared with the density field, the velocity profile exhibits a narrower distribution, with the jet boundary (defined as the radial position at which $u = 0.01u_c$) situated at $r/r_{1/2} \approx 2.5$, a value consistent with the data reported in Ref. [9]. In addition, no flat-hat profile exists even in the upstream region due to the use of the one-seventh power distribution for a fully developed turbulent pipe flow at the injector exit.

Figure 14 presents the axial distributions of the normalized temperature, density and compressibility factor along the centerline for three different pressures. Evidently, the temperature decreases relatively slowly with decreasing pressure in the axial direction. It is well established that when a fluid reaches its thermodynamic critical state, the constant-pressure specific heat becomes infinite and the thermal diffusivity decreases to zero, a phenomenon known as the critical divergence. Because the ambient pressure for Case 1 ($p_\infty = 4.3 \text{ MPa}$) is closer to the critical value, the specific heat increases drastically when the temperature transits across the inflection point on the isobaric ρ - T curve (see Fig. 4). This effect, combined with the lower thermal conductivity, causes a slower increase in temperature along the centerline in Case 1 as the injected fluid moves downstream. The compressibility factor, shown in Fig. 2, indicates a monotonic decrease with decreasing pressure in the low-temperature regime, and a rapid increase across the inflection point on the isobaric ρ - T curve. The compressibility factor, thus, increases much more rapidly at a lower pressure, which amounts to a faster decrease in density. Although the centerline temperature varies

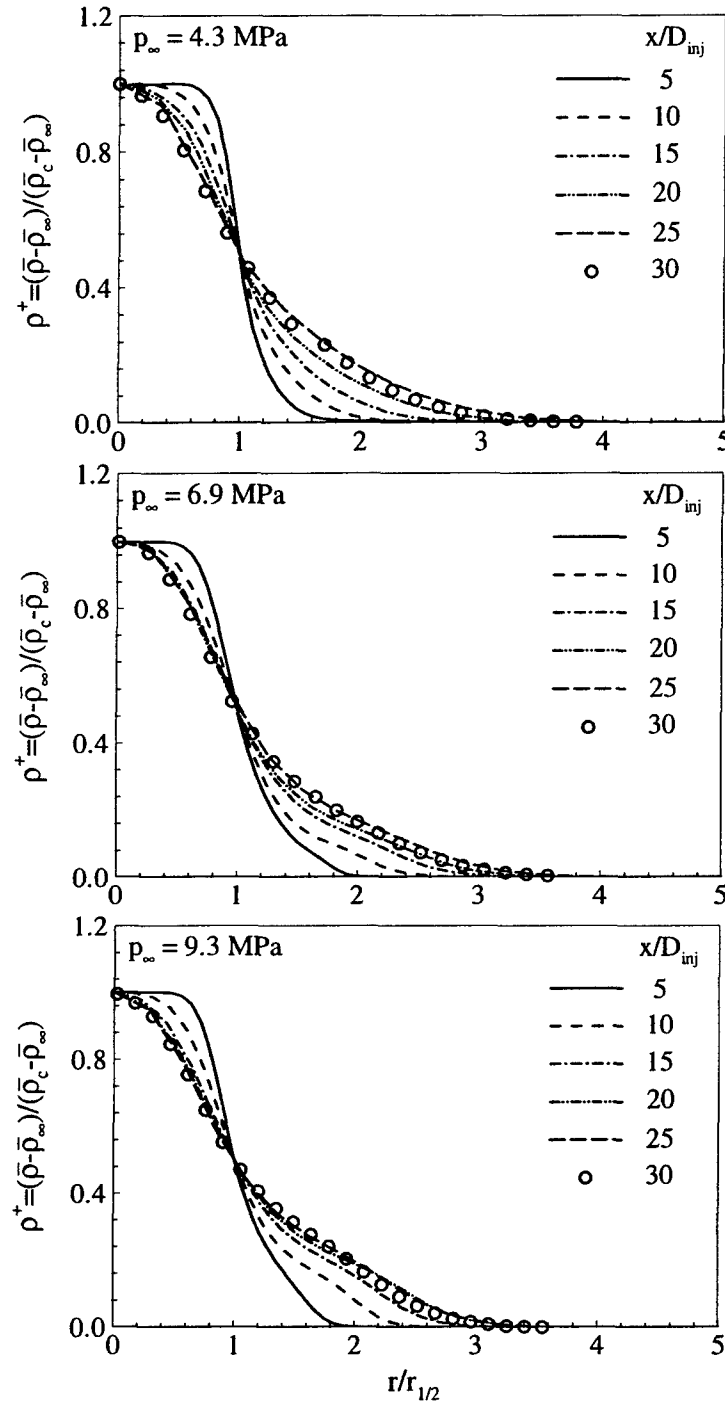


Fig.11 Effect of pressure on normalized density distribution in radial direction.

laggardly in all the three cases, the rapid variation of the compressibility factor causes the density to undergo a fast decrease downstream of the potential core, especially for the case of $p_\infty = 4.3 \text{ MPa}$.

The rapid variations of thermophysical properties exert a significant influence on the jet flow evolution. Figure 15 shows the radial distributions of the specific heat, thermal diffusivity, and kinematic viscosity at $x/D_{inj} = 10$, a location slightly upstream of the end of the potential core.

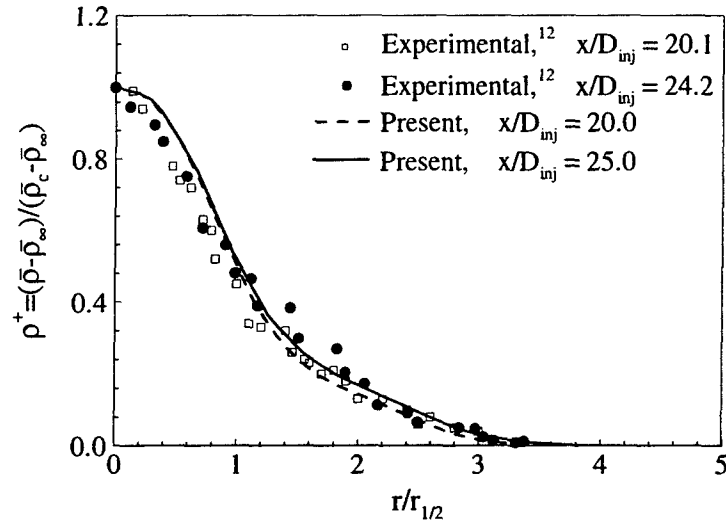


Fig.12 Comparison of calculated and measured density profiles at different axial locations.

A spike exists in the specific-heat profile at $r/r_{1/2} = 0.6$ in Case 1, mainly due to the temperature transition across the inflection point. The same phenomenon is observed for Cases 2 and 3, but with much lower amplitudes. The thermal diffusivity also exercises a large excursion of variation across the temperature inflection point. It increases considerably from the liquid core to the ambient flow by a factor of 14, 7, and 5 in Cases 1, 2, and 3, respectively. A similar situation occurs with the kinematic viscosity. The intensive change of viscosity in the shear layer gives rise to another vorticity production mechanism, as shown in equation (17). These observations, again, highlight the importance of thermophysical properties in dictating the behavior of a supercritical fluid jet [37].

2.7 Conclusions

A comprehensive numerical study has been conducted to investigate cryogenic fluid injection and mixing under supercritical conditions. The model accommodates full conservation laws and real-fluid thermodynamics and transport phenomena over the entire range of fluid states of concern. Turbulent closure is achieved using a large-eddy-simulation technique. The present analysis allows a detailed investigation into the temporal and spatial evolution of a cryogenic jet. The near-field behavior is well captured.

The major results obtained are summarized below.

1. As a result of intensive property variations between the fluid jet and surroundings, a series of large density-gradient regions are formed around the jet surface. These regions act like a solid wall that amplifies the axial flow oscillations but damps the radial ones. The interfacial instability in the shear layer is effectively suppressed, especially for cases with large density ratios. As the ambient pressure increases, the strength of density stratification decreases, so does its damping effect. Thus, the jet expands rapidly with increasing pressure.
2. Various mechanisms dictating vorticity transport are analyzed. The baroclinic torque arising from the density stratification between the injected and ambient flows and viscous dissipation play an important role in determining the flow evolution.

3. The jet dynamics are largely dictated by the local thermodynamic state of the fluid. When the temperature transits across the inflection point in an isobaric process, the rapid property variations may qualitatively change the jet behavior compared with its counterpart at low pressures. In addition, an increase in the ambient pressure may result in an earlier transition of the jet into the self-similar region.
4. The spatial growth rate of the surface instability wave increases as the ambient pressure increases. The frequency of the most unstable mode exhibits a weak pressure dependence at high pressures. It, however, decreases significantly in the near-critical regime due to the enhanced effect of density stratification and increased mixing-layer momentum thickness. The result agrees well with the linear stability analysis.

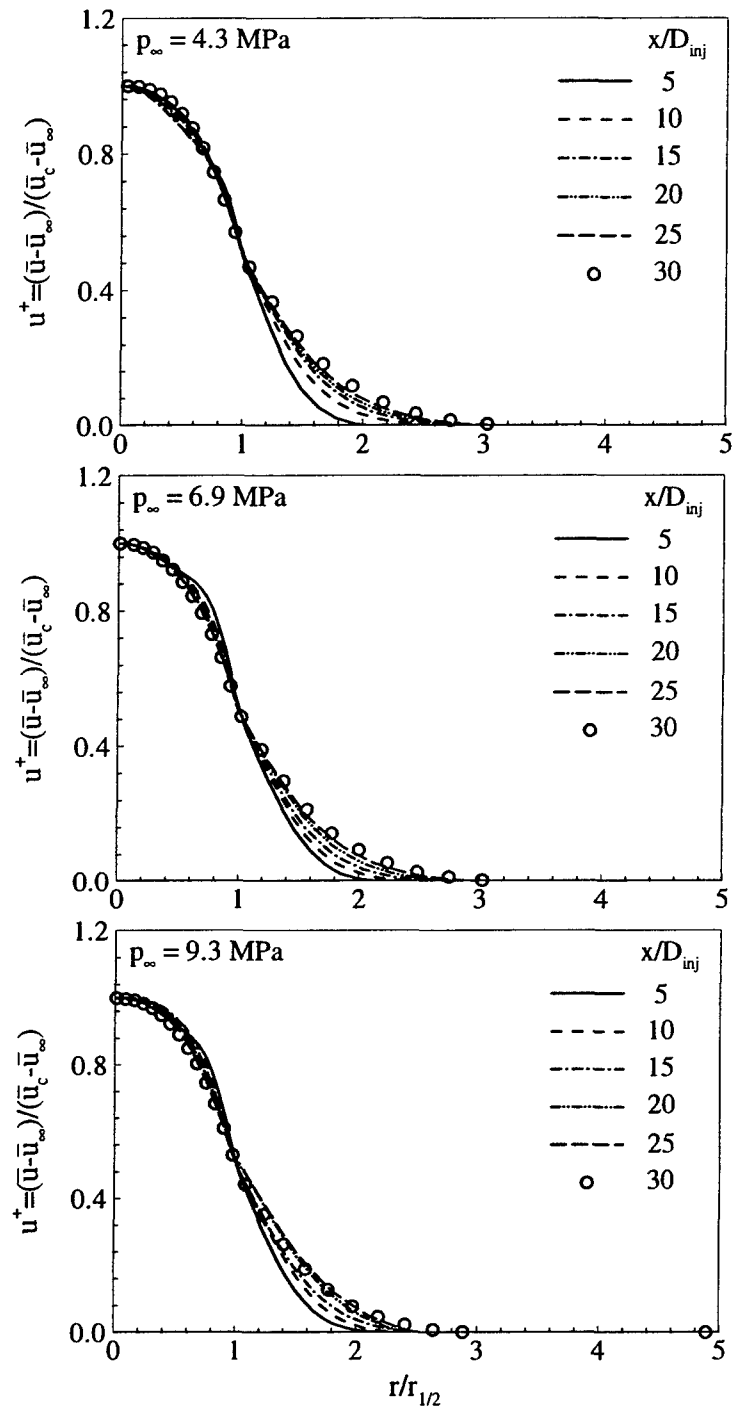


Fig.13 Effect of pressure on normalized velocity distribution in radial direction.

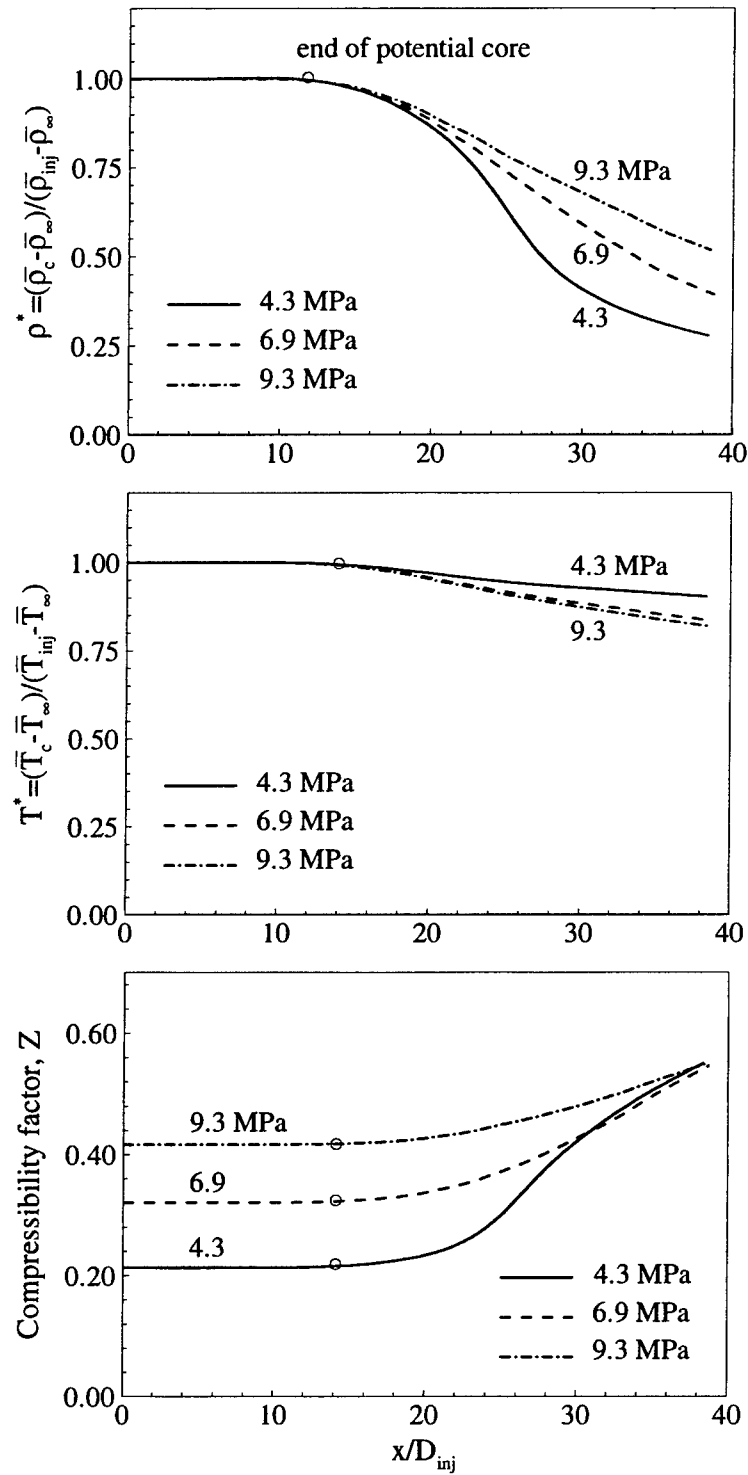


Fig.14 Effect of pressure on normalized density, normalized temperature, and compressibility factor along jet centerline.

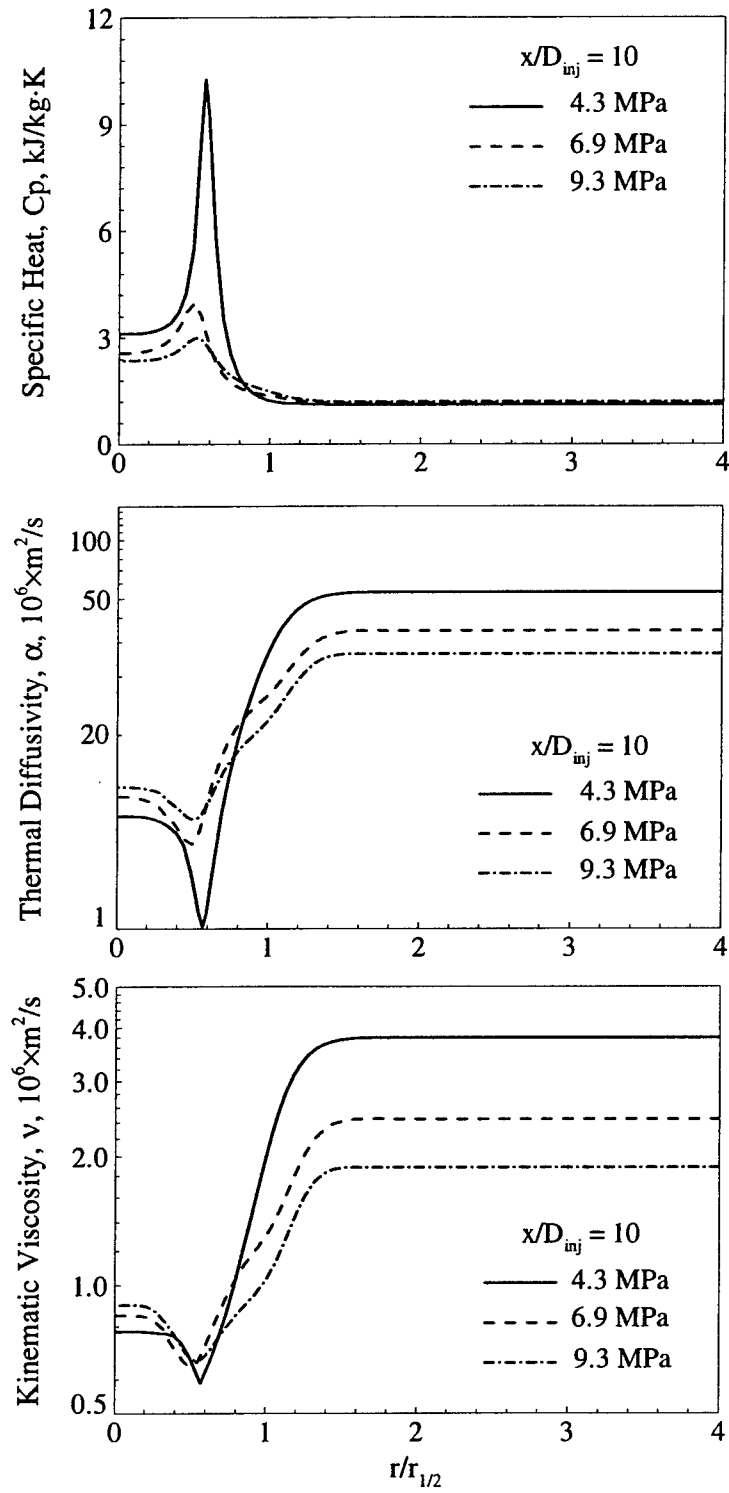


Fig.15 Radial distributions of mean thermophysical properties at $x/D_{inj} = 10$.

Reference:

- [1] J. M. H. Levelt Senger, "Thermodynamics of solutions near the solvent's critical point," *Supercritical Fluid Technology*, eds., T. J. Bruno and J. F. Ely, Chapter 1, CRC Press, Inc, Boca Raton, Florida, 1991.
- [2] J. C. Oefelein and V. Yang, "Modeling high-pressure mixing and combustion processes in liquid rocket engines," *J. Propul. Power* **114**, 843 (1998).
- [3] V. Yang, "Modeling of supercritical vaporization, mixing, and combustion processes in liquid-fueled propulsion systems," *Proc. Combust. Inst.* **28**, 925 (2000).
- [4] J. Bellan, "Supercritical (and subcritical) fluid behavior and modeling: drops, streams, shear and mixing layers, jets and sprays," *Prog. Energ. Combust.* **26**, 329 (2000).
- [5] J. A. Schetz, "Injection and mixing in turbulent flow", *AIAA Prog. Aeronaut. Astronaut.* **68**, 19 (1980).
- [6] G. N. Abramovich, *The theory of turbulent jets*, MIT Press, Cambridge, Massachusetts, 1963.
- [7] J. A. Newman and T. A. Brzustowski, "Behavior of a liquid jet near the thermodynamic critical region," *AIAA J.* **19**, 1595 (1971).
- [8] W. Mayer, A. Schik, M. Schäffler and H. Tamura, "Injection and mixing processes in high pressure liquid oxygen / gas nitrogen rocket combustors," *J. Propul. Power* **16**, 823 (2000).
- [9] R. Branam and W. Mayer, "Characterization of cryogenic injection at supercritical pressure," *J. Propul. Power* **19**, 342 (2003).
- [10] B. Chehroudi, D. Talley and E. Coy, "Visual characteristics and initial growth rates of round cryogenic jets at subcritical and supercritical pressures," *Phys. Fluids* **14**, 850 (2002).
- [11] M. Oswald and A. Schik, "Supercritical nitrogen free jet investigated by spontaneous Raman scattering," *Exp. Fluids* **27**, 497 (1999).
- [12] B. Chehroudi, R. Cohn, D. Talley and A. Badakhshan, "Cryogenic shear layers: experiments and phenomenological modeling of the initial growth rate under subcritical and supercritical conditions," *Int. J. Heat Fluid Fl.* **23**, 554 (2002).
- [13] B. Chehroudi and D. Talley, "Interaction of acoustic waves with a cryogenic nitrogen jet at sub- and super-critical pressures," *AIAA Paper No. 2002-0342*, 40th AIAA Aerospace Sciences Meeting and Exhibit, Reno, NV, January 2002.
- [14] H. Meng, and V. Yang, "A unified treatment of general fluid thermodynamics and its application to a preconditioning scheme," *J. Comput. Phys.* **189**, 277 (2003).
- [15] N. A. Okong'o and J. Bellan, "Direct numerical simulation of a transitional supercritical binary mixing layer: heptane and nitrogen," *J. Fluid Mech.* **464**, 1 (2002).
- [16] R. S. Miller, K. G. Harstad and J. Bellan, "Direct numerical simulations of supercritical fluid mixing layers applied to heptane-nitrogen," *J. Fluid Mech.* **436**, 1 (2001).
- [17] N. A. Okong'o, K. G. Harstad and J. Bellan, "Direct numerical simulation of O₂/H₂ temporal mixing layers under supercritical conditions," *AIAA J.* **40**, 914 (2002).
- [18] G. Erlebacher, M. Y. Hussaini, C. G. Speziale and T. A. Zang, "Toward the large eddy simulation of compressible turbulent flows," *J. Fluid Mech.* **238**, 155 (1992).
- [19] M. S. Graboski and T. E. Daubert, "A modified soave equation of state for phase equilibrium calculation, 1. hydrocarbon systems," *Ind. Eng. Chem. Proc. Design Dev.* **17**, 443 (1978).
- [20] J. F. Ely and H. J. Hanley, "Prediction of transport properties. 1. viscosity of fluids and mixtures," *Ind. Eng. Chem. Fundamentals* **20**, 323 (1981).
- [21] J. F. Ely and H. J. Hanley, "Prediction of transport properties. 2. thermal conductivity of pure fluids and mixtures," *Ind. Eng. Chem. Fundamentals* **22**, 90 (1983).

- [22] J. V. Sengers, R. S. Basu and J. M. H. Levelt Sengers, "Representative equations for the thermodynamic and transport properties of fluids near the gas-liquid critical point," NASA Contractor Report 3424 (1981).
- [23] J. S. Shuen, K. H. Chen and Y. Choi, "A coupled implicit method for chemical non-equilibrium flows at all speeds," *J. Comput. Phys.* **106**, 306 (1993).
- [24] S. Y. Hsieh and V. Yang, "A preconditioned flux-differencing scheme for chemically reacting flows at all Mach numbers," *Int. J. Comput. Fluid Dyn.* **8**, 31 (1997).
- [25] R. C. Swanson and E. Turkel, "On central difference and upwind schemes," *J. Comput. Phys.* **101**, 292 (1992).
- [26] N. Zong, "Modeling and simulation of cryogenic fluid injection and mixing dynamics under supercritical conditions," Ph.D. Dissertation, Dept. of Mechanical and Nuclear Engineering, Pennsylvania State Univ., University Park, PA, 2004.
- [27] T. Poinso, and S. Lele, "Boundary Conditions for Direct Simulation of Compressible Viscous Flows," *J. Comput. Phys.* **101**, 104 (1992).
- [28] S. C. Crow and F. H. Champagne, "Orderly structure in jet turbulence," *J. Fluid Mech.* **48**, 547 (1971).
- [29] P. Atsavapranee and M. Gharib, "Structures in stratified plane mixing layers and the effects of cross-shear," *J. Fluid Mech.* **342**, 53 (1997).
- [30] I. A. Hannoun, H. J. S. Fernando and E. J. List, "Turbulence structure near a sharp density interface," *J. Fluid Mech.* **189**, 189 (1988).
- [31] S. Apte and V. Yang, "Unsteady flow evolution in porous chamber with surface mass injection, part 1: free oscillation," *AIAA J.* **39**, 1577 (2001).
- [32] A. D. Gilbert, "Spiral structures and spectral in two-dimensional turbulence," *J. Fluid Mech.* **193**, 475 (1988).
- [33] K. C. Schadow and E. Gutmark, "Combustion instability related to vortex shedding in dump combustors and their passive control", *Prog. Energy Combust. Sci.* **18**, 117 (1992).
- [34] M. H. Yu and P.A. Monkewitz, "The effect of nonuniform density on the absolute instability of two-dimensional inertial jets and wakes," *Phys. Fluids A* **2**, 1175 (1990).
- [35] M. C. Soteriou and A. Ghoniem, "Effects of the free-stream density ratio on free and forced spatially developing shear layers," *Phys. Fluids* **7**, 2036 (1995).
- [36] T. Liu, "Temporal and spatial stability of real-fluid mixing layer with density stratification," M.S. Dissertation, Dept. of Mechanical and Nuclear Engineering, Pennsylvania State Univ., University Park, PA, 2004.
- [37] B. Chehroudi, D. Talley, W. Mayer, R. Branam, J. J. Smith, A. Schik, and M. Oswald, "Understanding injection into high pressure supercritical environments," 5th International Conference on Liquid Space Propulsion, Chattanooga, TN, 2003.

Task 3

Shear Co-axial Injection of Cryogenic Fluids with Acoustic Excitations

This task simulated the experiments conducted by Chehroudi, Talley, and colleagues at the Air Force Research Laboratory (AFRL). The purpose is to investigate cryogenic fluid injection and mixing of a shear coaxial injector under conditions with and without externally impressed acoustic forcing. A cryogenic nitrogen jet is injected through a sharp-edged stainless-steel tube having a length of 50 mm and an inner diameter 0.508 mm. The inner tube thickness is 0.415 mm. The outer diameter of the annular stream is 2.42 mm. To facilitate the application of acoustic boundary condition correctly, a cuboid computational domain is generated. The entire grid system (except for the region inside the injector) has $141 \times 81 \times 301$ (3.44 million) cells along the axial, radial and azimuthal directions, respectively, of which 41 axial cells are used to cover the LN_2 inlet section and 31 axial cells for the GN_2 inlet section. Square grids are implemented in the center region in order to avoid the numerical singularity at the centerline of the computation domain and to increase the computational efficiency. The grid resolution is chosen based on the inlet Reynolds number, such that the largest grid size falls in the inertial sub-range of the turbulent energy spectrum. The analysis is conducted on an in-house distributed-memory parallel computer. The computational domain is divided into 72 blocks, and a total number of 57 processors are used.

Results from this task have led to the following technical publication.

“Dynamics of Shear-Coaxial Cryogenic Nitrogen Jets with Acoustic Excitation under Supercritical Conditions,” by T. Liu, N. Zong, and V. Yang, AIAA Paper 2006-0759, presented at the 44th AIAA Aerospace Sciences Meeting and Exhibit, January 2006.

3.1 Introduction

Combustion instability has long been one of the most complicated phenomena in the development of liquid rocket engines. The prevalence of instabilities is primarily attributed to two fundamental phenomena:[1] Combustion chambers are almost entirely closed and the internal processes tending to attenuate unsteady motions are weak and the energy required to drive unsteady motions represents exceedingly small fraction of the heat released by combustion. Characterized by high amplitudes and high frequencies, acoustic instability is the most destructive. It will cause local burnout of combustion chamber walls and injector plates and may significantly shorten the lifetimes of a combustor[2]. In order to thoroughly understand the nature of interactions between acoustic waves and liquid propellant combustion in rocket engines, it is important to conduct theoretical and experimental studies on simplified configurations.

Injectors play an important role in defining the flow structure and flame dynamics. In modern liquid rocket engines, shear coaxial jet injectors have been commonly used. Coaxial atomization can be divided into five distinctive physical regimes[3]: 1) turbulent liquid core; 2) liquid/gas interface where primary atomization occurs; 3) dense spray where second atomization and droplet breakup occur; 4) dilute spray where droplets are dispersed; 5) gas flow region. The dominant flow parameters involved include: Reynolds number (Re), momentum flux ratio (M), area ratio, and Weber number (We). The primary advantage of a shear coaxial jet injector lies in the fact that, with a large outer(fuel)-to-inner(oxidizer) momentum flux ratio, it is efficient to fragment and mix the reactants to a satisfactory level of uniformity for evaporation and combustion within a preferred distance.

Studies of shear coaxial injection have been extensive. Mayer and Krülle[3] found in their experiment on water and air that similar to increasing gas velocity, increasing gas density results in a faster and finer atomization. The phenomena may be attributed to the increased surface wave growth and instabilities of liquid jets and enhanced liquid atomization. Rehab, Villiermaux, and Hopfinger[4] studied the effects of large velocity ratio on coaxial water/water jets. When the velocity ratio of the annular to the inner jet is less than a critical value, the inner potential core is found to be inversely dependent on the velocity ratio. Otherwise, the inner potential core will be truncated by the unsteady recirculating bubble. The same authors[5] later examined the geometric effects. A larger annular gap was found to result in a longer inner potential core and a larger value of the critical velocity ratio. The location of the recirculation zone appeared at a further location. An increase of the retraction of the inner jet exit increases inner potential core, and the recirculation zone occurs closer to the outer-jet exit. Lasheras, Villiermaux, and Hopfinger[6] conducted experiments on water jets surrounded with co-flowing high-speed annular air. Weber number was found to have a weak effect on the break-up when $We > 200$. The momentum-flux ratio exerted a dominant effect on the liquid-intact length, especially with a larger initial Weber number.

So far, limited effort was devoted to the effect of acoustic excitation. Chehroudi, Davis and co-workers[7,8,9] studied the interactions between acoustic waves and a cryogenic jet at sub- and supercritical pressures. The effects of acoustic waves on the coaxial injection with liquid and gaseous nitrogen were examined over a wide range of chamber pressures. It was found that the acoustic effects were substantial under subcritical conditions, but became unnoticeable as pressure increased above the critical point. The shear coaxial jets at subcritical conditions were more easily to be influenced with a higher velocity ratio.

The present work attempts to simulate the experiment work described in Ref.7-9. It deals with numerical simulation of coaxial fluid injection and mixing dynamics under super-critical conditions with/without acoustic excitation. Results will enhance basic understanding of interactions between acoustic waves and coaxial jets in cryogenic-propellant rocket engines. This portion of work is organized as follows. Section II and III describe the theoretical formulation and numerical method, respectively. In Section IV, the computational domain and grid system is addressed, and primary results are presented and discussed. Finally, a brief summary is given in Section V.

3.2 Theoretical Formulation

Several computational and modeling challenges must be overcome in order to perform numerical simulations on high-pressure cryogenic fluid dynamics. First, thermodynamic non-idealities and transport anomalies occur as the fluid transits through the transcritical regime. Thus treating these phenomena in a manner consistent with the intrinsic characteristics of a numerical algorithm presents a main obstacle. Second, the rapid variation of fluid state and wide disparities in the characteristic time and length scales impose the well-known stiffness problem. In order to circumvent all these difficulties, a comprehensive theoretical framework capable of treating turbulence, transcritical property variations, and general fluid thermodynamics is developed.

3.2.1 Governing Equations

The present analysis is based on a large-eddy-simulation (LES) technique, in which large-scale turbulent structures are directly computed and small dissipative structures are modeled.

Mathematically, the LES methodology begins with filtering of small-scale effects from large-scale motions in the full conservation equations.

$$f = \tilde{f} + f'' \quad (1)$$

The Favre-filtered averaging is employed here to simplify the governing equations and to account for the variable density effects.

$$\tilde{f} = \frac{\overline{\rho f}}{\bar{\rho}} \quad (2)$$

The Favre-filtered conservation equations of mass, momentum, and energy can be expressed in the following conservation form:

$$\frac{\partial \bar{\rho}}{\partial t} + \frac{\partial \bar{\rho} \tilde{u}_j}{\partial x_j} = 0 \quad (3)$$

$$\frac{\partial \bar{\rho} \tilde{u}_i}{\partial t} + \frac{\partial (\bar{\rho} \tilde{u}_i \tilde{u}_j + \bar{p} \delta_{ij})}{\partial x_j} = \frac{\partial (\bar{\tau}_{ij} - \tau_{ij}^{sgs})}{\partial x_j} \quad (4)$$

$$\frac{\partial \bar{\rho} \tilde{e}_i}{\partial t} + \frac{\partial [(\bar{\rho} \tilde{e}_i + \bar{p}) \tilde{u}_j]}{\partial x_j} = \frac{\partial (\tilde{u}_i \bar{\tau}_{ij} + \bar{q}_j - H_j^{sgs} + \sigma_j^{sgs})}{\partial x_j} \quad (5)$$

where ρ , u_i , p , e_i , q_j and τ_{ij} represent the density, velocity components, pressure, specific total energy, heat flux, and viscous stress tensor, respectively. The subgrid-scale terms in Eqs. (4)-(5), i.e., the subgrid stress, subgrid energy fluxes, and subgrid viscous work are given below.

$$\tau_{ij}^{sgs} = (\overline{\rho u_i u_j} - \bar{\rho} \tilde{u}_i \tilde{u}_j) \quad (6)$$

$$H_j^{sgs} = (\overline{\rho e_i u_j} - \bar{\rho} \tilde{e}_i \tilde{u}_j) + (\overline{p u_j} - \bar{p} \tilde{u}_j) \quad (7)$$

$$\sigma_j^{sgs} = (\overline{u_i \tau_{ij}} - \bar{\rho} \tilde{u}_i \tilde{\tau}_{ij}) \quad (8)$$

The sgs terms are closed by implementing an improved Smagorinsky model proposed by Erlebacher et al.[10]

$$\tau_{ij}^{sgs} = -2\nu_t \bar{\rho} \left(\tilde{S}_{ij} - \frac{\tilde{S}_{kk} \delta_{ij}}{3} \right) + \frac{2}{3} \bar{\rho} k^{sgs} \delta_{ij} \quad (9)$$

$$H_j^{sgs} = -\bar{\rho} \frac{\nu_t}{Pr_t} \left(\frac{\partial \tilde{h}}{\partial x_j} + \tilde{u}_i \frac{\partial \tilde{u}_i}{\partial x_j} + \frac{1}{2} \frac{\partial k^{sgs}}{\partial x_j} \right) \quad (10)$$

where

$$\nu_t = C_R \Delta^2 |\tilde{S}| \quad (11)$$

$$k^{sgs} = C_I \Delta^2 \tilde{S}_{ij} \tilde{S}_{ij} \quad (12)$$

The dimensionless quantities C_R and C_I represent the compressible Smagorinsky constants, Δ is the filter width, $\tilde{S}_{ij} = (\partial \tilde{u}_i / \partial x_j + \partial \tilde{u}_j / \partial x_i) / 2$, and Prt the turbulent Prandtl number for which a standard value of 0.7 is used. The *sgs* viscous work term σ_{ij}^{sgs} , is neglected in the present work due to its small contribution to the total energy equation.

3.2.2 Equation of State and Thermodynamic Properties

A modified Soave-Redlich-Kwong (SRK) equation of state is selected in the present study because of its reasonable accuracy over the high-pressure and low-temperature regime in the present study and ease of implementation[11].

$$p = \frac{RT}{(V-b)} - \frac{a\alpha}{V(V+b)} \quad (13)$$

where V and R are the molar volume and universal gas constant, respectively. The energy and volume constants, a and b , are determined respectively from the following universal relations in terms of the critical temperature and pressure.

$$a = 0.42747 R^2 T_c^2 / p_c; b = 0.08664 R T_c / p_c \quad (14)$$

The parameter α is a function of the reduced temperature and acentric factor.

$$\alpha = \left(1 + (0.48508 + 1.55171\omega - 0.15613\omega^2)(1 - T_r^{0.5}) \right)^2; T_r = T/T_c \quad (15)$$

In order to avoid computationally intensive iterations in calculating thermodynamic properties, an accurate curve fit of $T(e, \rho)$ is employed to update the temperature based on the specific internal energy and density over the entire fluid state of concern. Thermodynamic properties including enthalpy, internal energy and heat capacity are directly calculated by means of fundamental thermodynamic theories.

3.2.3 Transport Properties Evaluation

Transport properties including viscosity and thermal conductivity are estimated by means of the corresponding state principles along with the use of the 32-term Benedict-Webb-Rubin (BWR) equation of state, which are also implemented using curve fits of $\mu(p, T)$ and $\lambda(p, T)$.

3.3 Numerical Method and Boundary Conditions

The theoretical formulation outlined above is solved by means of a density-based, finite volume methodology. The spatial discretization employs a fourth-order, central-difference scheme in generalized coordinates. A fourth-order scalar dissipation with a total-variation-diminishing switch developed by Swanson and Turkel is implemented to ensure computational stability and to

prevent numerical oscillations in regions with steep gradients. Temporal discretization is obtained using a four-step fourth-order Runge-Kutta scheme. A multi-block domain decomposition technique, along with static load balance, is employed to facilitate the implementation of parallel computation with message passing interfaces at the domain boundaries.

The boundary conditions used in the present work are listed below. At the inlet boundary, the three velocity components and temperature are specified. The pressure is obtained from a simplified one-dimensional axial-momentum equation. At the outflow exit, the ambient pressure is specified and the three velocity components and temperature are extrapolated from the interior. The non-slip, adiabatic wall conditions are applied to all solid walls. In the case with acoustic excitations, periodic pressure oscillations are imposed at the side wall in order to generate transverse standing acoustic waves in the chamber.

3.4 Results and Discussions

3.4.1 Computational Case Description

The analysis simulates the experiments by Chehroudi, Davis and coworkers [7-9]. Liquid nitrogen is delivered through the inner tube and gaseous nitrogen flows through the concentric tube at a higher velocity. The temperatures of inner and outer jets are specified as 132 K and 191 K, respectively. The diameters of the inner and outer tubes are 0.508 mm and 1.59 mm, respectively and the annulus height is 0.415 mm as shown in Fig. 1.

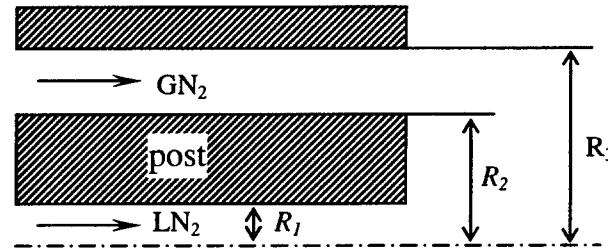


Figure 1. Schematic of the coaxial injector employed for the high-pressure LN2/GN2 mixing simulation. ($R_1 = 0.254\text{mm}$, $R_2 = 0.795\text{mm}$, $R_3 = 1.21\text{mm}$)

In order to efficiently implement acoustic boundary conditions, a cuboid computational domain shown in Fig. 2 is employed. For cases without acoustic excitation, the main body grid system besides the inlet and buffer parts has $301 \times 141 \times 81$ (3.44 million) points along the axial, radial and azimuthal direction, respectively, of which 31 radial points are used to cover the LN2 and GN2 inlet section, respectively. Square grids are used in the center part to avoid the numerical singularity in the center region. The grid resolution is chosen based on the inlet Reynolds number such that the largest grid size falls in the inertial sub-range of the turbulent energy spectrum. All the calculations are performed on an in-house distributed-memory parallel computer. The computation domain is divided into 72 blocks, and a total number of 57 processes are used. For cases involving acoustic excitations, the computational domain is extended in the y direction in order to generate standing acoustic waves with desired frequencies.

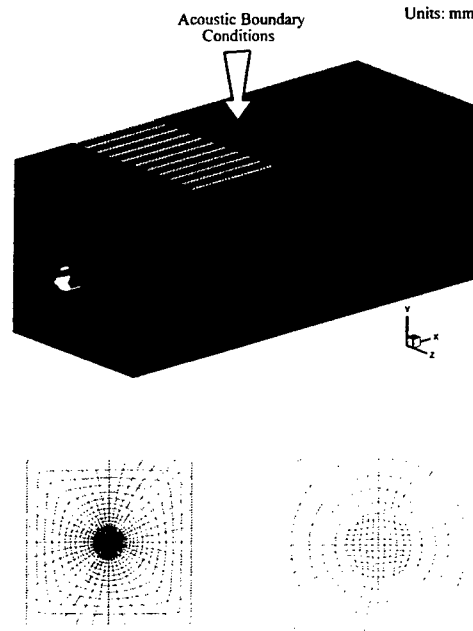


Figure 2. Schematic of grid system, total grid points, $141 \times 81 \times 301 = 3.44$ million. (The presented grid has fewer points than these used in the calculations, but the distributions of grid points are similar)

Four different flow conditions without acoustic excitation were first treated to investigate the effects of ambient pressure, velocity ratio and momentum flux ratio on the injector flow evolution. Table 1 summarizes the flow parameters and simulation conditions. The temperature selected here matches the supercritical cases studied by Chehroudi, et al. [7-9]. Case 1 corresponds to one of their experimental conditions with a chamber pressure of 4.94 MPa. The velocities of the inner and out jets are increased proportionally to shorten the computational time while remaining the same momentum-flux and velocity ratios as those in the experiments. The chamber pressure of case 2 is increased to 10 MPa with all the others conditions remaining fixed in order to examine the effect of chamber pressure. Cases 3 and 4 have the same conditions as cases 1 and 2, respectively, except that different annular flow velocities are selected in order to obtain different momentum flux ratios. In the end, cases 1 and 4 have momentum-flux ratios about 3.45, same as that of the SSME preburner injector. Case 2 has a momentum flux ratio 1.0, which is close to that of the SSME main chamber injector.

A simple 2D computational domain, as shown in Fig. 3, along with periodic boundary conditions in the z direction was first employed to test the specification of acoustic boundary conditions. The chamber pressure is set as 4.94 MPa and temperature as 233 K. Sinusoidal pressure oscillations with a frequency 3000Hz are imposed at one of the side wall. Figure 4 shows the generated acoustic velocity probed at different locations along line 2 at different times. Figure 5 shows the acoustic velocity and pressure along the y direction. It can be concluded from both figures that the acoustic waves generated are nearly perfect standing waves. The deviation may arise from the real-fluid effects, which leads to a more complex relationship between fluid density and temperature. Selected frequency of 3000 Hz is exactly not exactly natural frequency of the chamber in the y direction because of the presence of real fluid density in the inner jet region. The largest velocity oscillation occurs at the acoustic antinodal line in the inner jet regions.

Table 1 Simulation conditions for analysis of shear-coaxial cryogenic nitrogen mixing process.

	case 1	case 2	case 3	case 4
P (MPa)	4.94	10	4.94	10
T_{chm} (K)	233	233	233	233
T_f (K)	191	191	191	191
T_o (K)	132	132	132	132
ρ_f (kg/m ³)	98.8	217.2	98.8	217.2
ρ_o (kg/m ³)	404.0	555.4	404.0	555.4
u_f (m/s)	120	120	65	95
u_o (m/s)	32	32	32	32
u_f / u_o	3.75	3.75	2.03	2.97
$(\rho u)_f / (\rho u)_o$	0.92	1.47	0.50	1.16
$(\rho u^2)_f / (\rho u^2)_o$	3.44	5.50	1.01	3.45
\dot{m}_f / \dot{m}_o	11.9	19.0	6.4	15.0
a_f (m/s)	279.6	302.2	279.6	302.2
a_o (m/s)	230.9	441.2	230.9	441.2
M_f	0.43	0.40	0.23	0.31
M_o	0.14	0.08	0.14	0.08
Re_f	3.3E5	5.8E5	1.8E5	4.6E5
Re_o	1.3E5	1.0E5	1.3E5	1.0E5
<i>Re based on R_i and R_o</i>				

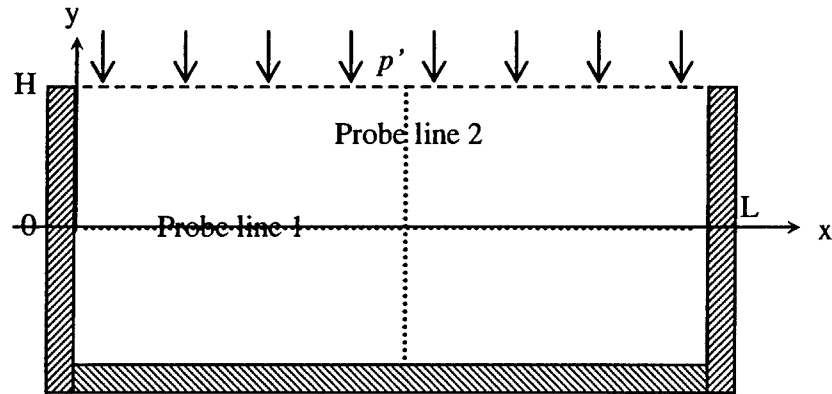


Figure 3. Schematic diagram of acoustic generation

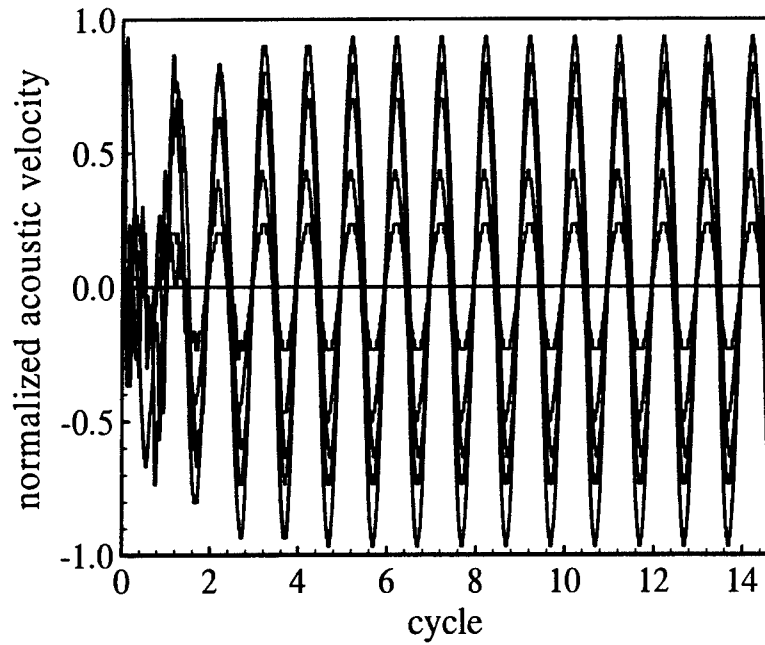


Figure 4. Normalized acoustic velocities at different locations on line 2.

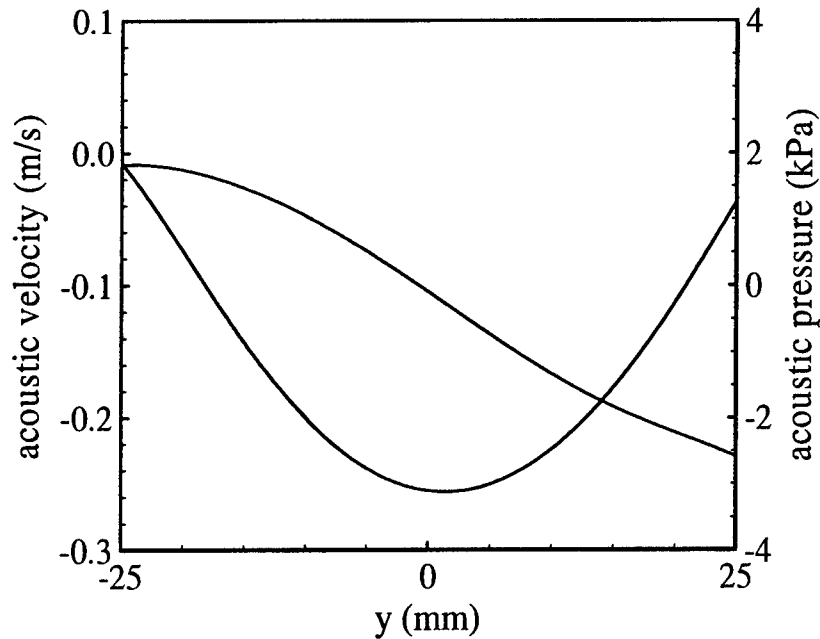


Figure 5. Instantaneous acoustic velocity and pressure along probe line 2.

3.4.2 Flow Evolution without External Acoustic Excitation

Investigations were first conducted into injector dynamics under conditions without externally imposed acoustic oscillations. Figure 6 shows the snapshots of the temperature and temperature-gradient fields. The near-field injector flow dynamics can be characterized by the evolution of three mixing layers. The inner mixing layer forms around the liquid nitrogen jet and

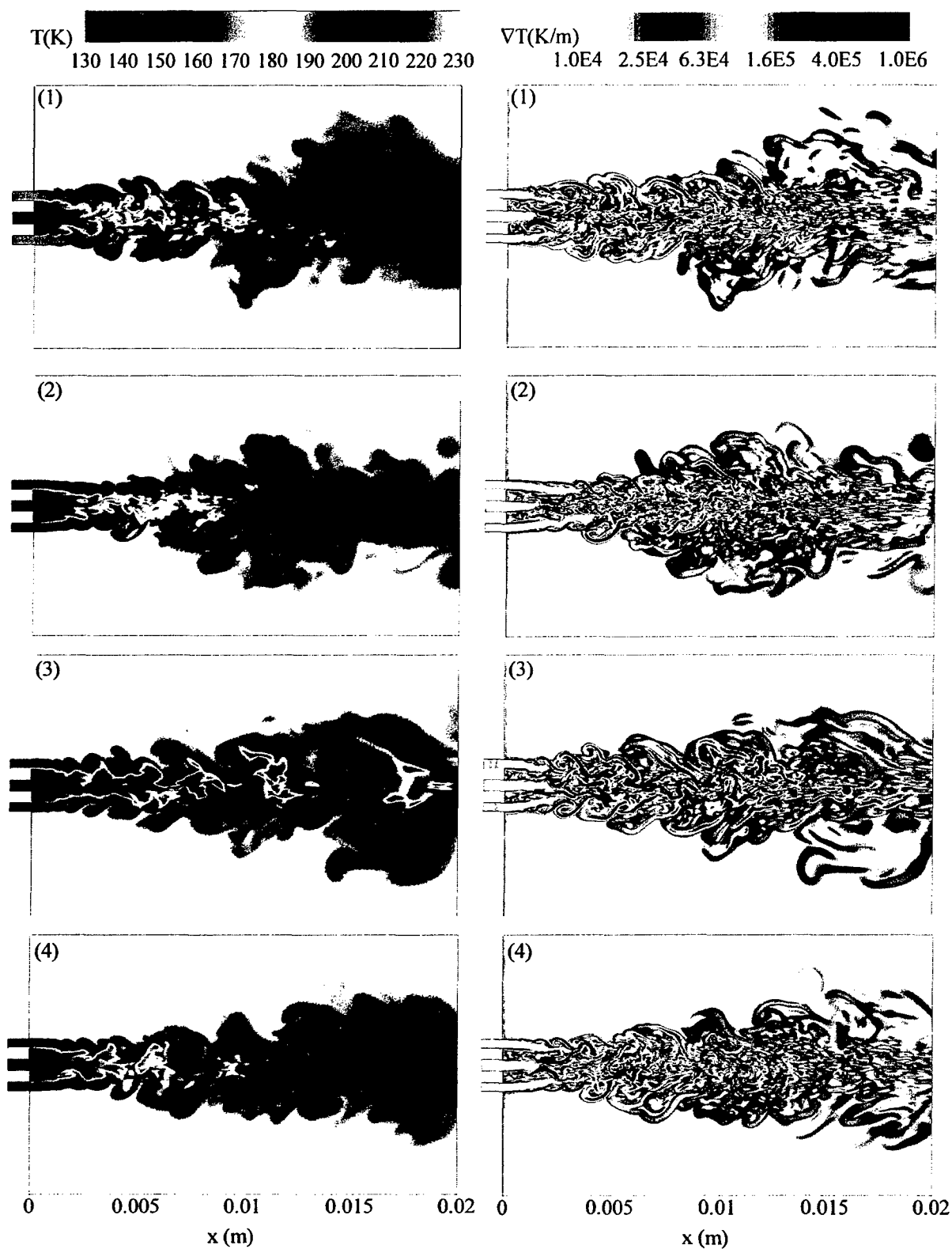


Figure 6. Effect of pressure and velocity ratios on temperature, and temperature-gradient fields.

the other two emerge from the inner and outer boundaries of the annular gaseous nitrogen stream. Two shear layers separated by the port merge together after large-scale vortices originating from the outer rim of the tube grow up. Similar to experimental observations, the evolution of the outer shear layers prevails over the inner one because of the greater velocity difference between the high-speed outer stream and the surroundings. At the same chamber pressure, (i.e. cases 1 and 3), the inner cold fluid, which is colored by blue, fades away after a short flow path for the case with a faster annular stream (case 1). The phenomenon may be attributed to the enhanced turbulent mixing at a higher velocity ratio. At a higher velocity ratio, the large-scale vortices pinch the centerline earlier and the potential cores of the inner streams are reduced. Figure 7 shows the mean-axial velocity and temperature fields. For all cases, the existence of an inner and an outer potential core are clearly demonstrated. The longest inner potential core is obtained in case3, owing to the strong density stratification and the lower momentum flux ratio between the inner and outer streams. Jet spreading angle is an important parameter to measure the mixing and entrainment between the injected flow and the ambience. At a constant chamber pressure, the outer jet spreading angle increases with increasing of annular jet velocity. The existence of wake/recirculation flow region immediately behind the post is manifested by the negative velocity contour in Fig. 7.

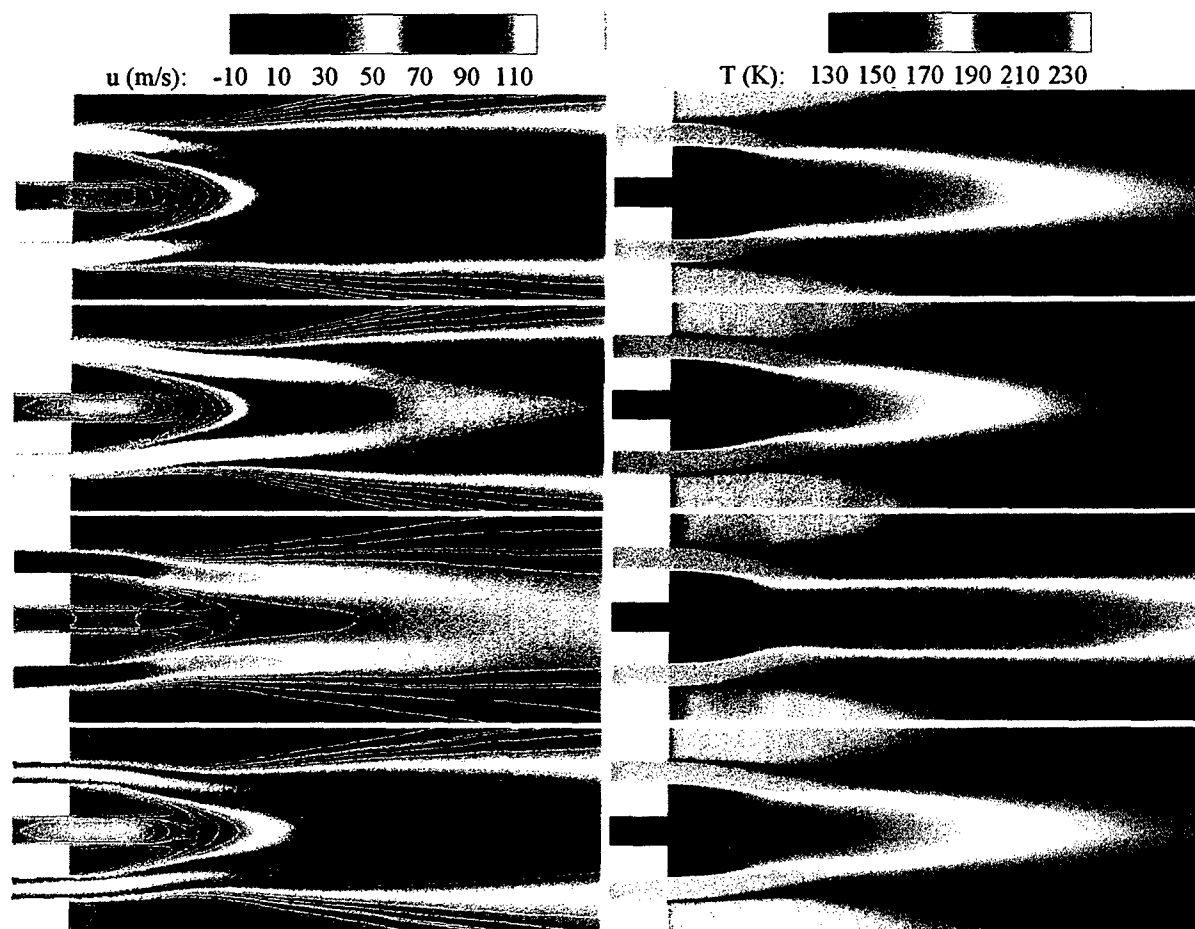


Figure 7. Effect of momentum flux ratio on flow evolution, illustrated by contours of mean axial velocity and temperature for different cases.

Figure 8 shows the streamlines based on the mean axial and radial velocities. Flow recirculation clearly occurs between the inner and annular jets. Rehab, Villiermaux and Hopfinger [4] discussed the mechanism responsible for the occurrence of the recirculating regime on the jet axis. When the jet velocity ratio is large enough, the dynamic pressure $\rho \bar{u}_i^2/2$ is not sufficiently strong to accelerate the flow in the positive direction and a reverse flow thus occurs. A model was also proposed to calculate the critical velocity ratio. The velocity ratios in this work, however, are much less than their predictions because of real-fluid effects and geometrical difference. In their investigation, the thickness of the inner tube is assumed to be zero and the recirculation bubble appears on the jet axis. In the present analysis, the thickness of the inner tube is finite. The resultant wake can easily give rise to flow reversal behind inner tube. The same phenomena were found by Davis[12]. He described a recirculation zone attached to the lip of the inner tube, which agrees well with our simulation. If we further increase the momentum-flux ratio to a sufficiently large value, recirculation zone may extend to the jet axis line.

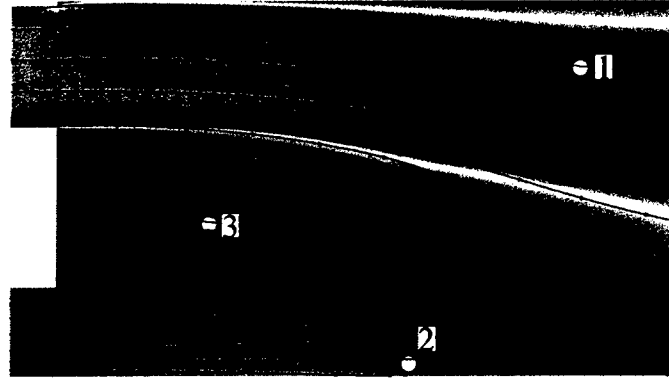


Figure 8. Mean axial velocity field and streamlines based on mean axial and radial velocity components.

Figure 9 shows snapshots of the isosurfaces of positive Q and pressure for case 3. Positive Q isosurfaces isolates areas where the strength of rotation overcomes the strain, thus making those surfaces eligible as vortex envelopes[13]. It is defined as

$$Q = \frac{(\Omega_{ij}\Omega_{ji} - S_{ij}S_{ji})}{2} \quad (16)$$

where

$$\Omega_{ij} = \frac{1}{2} \left(\frac{\partial u_i}{\partial x_j} - \frac{\partial u_j}{\partial x_i} \right) \text{ and } S_{ij} = \frac{1}{2} \left(\frac{\partial u_i}{\partial x_j} + \frac{\partial u_j}{\partial x_i} \right) \quad (17)$$

Large-scale helical structures and discrete vortex rings form intermittently in the near field from the outer shear layer. These rings seem to have the same wavelength until they begin to disappear in the downstream region. Figure 9(a) is plotted with/without showing parts outside the inner tube. The same structures are devoted by the sky-blue color, representing the locations of recirculation bubbles. Figure 10 shows the power spectral densities (PSD) of the pressure oscillation at three near-field locations in inner, annular jets and recirculation region, respectively. The result suggests the oscillation frequency of the recirculation region is determined by the vortex shedding frequency.

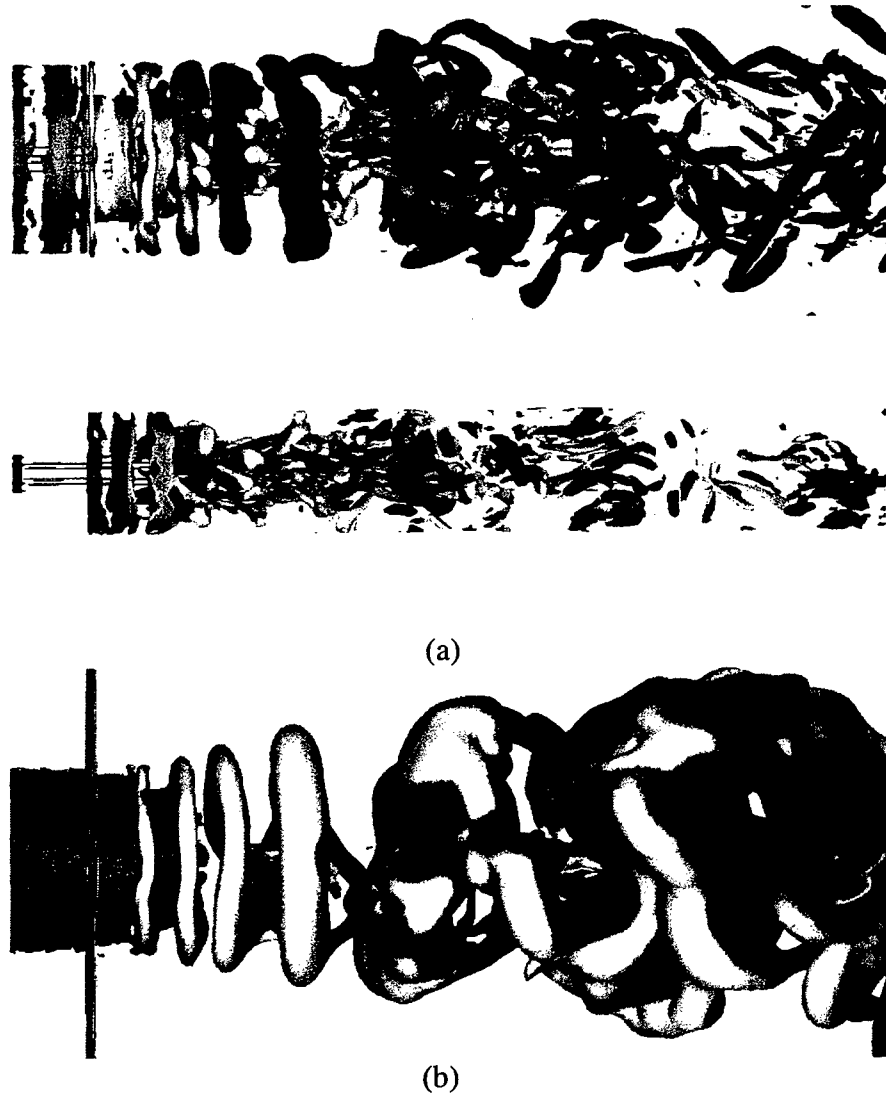


Figure 9. Large coherent structures visualized by iso-surface of instantaneous Q (a) and pressure (b) at 4.935MPa for case 3. (color contours are instantaneous temperature)

3.4.3 Flow Evolution with External Acoustic Excitation

To study the effects of acoustic waves, external pressure oscillation with an amplitude 15kPa and a frequency 3000Hz was imposed at one sidewall after the flowfield becomes stationary. The power spectral densities of the pressure and velocity oscillation near the opposite sidewall were conducted. The resultant dominant frequency of 3000Hz is identical to the frequency of externally imposed pressure oscillations, confirming the success of acoustic generation.

Figure 11 shows the evolution of the temperature field within one cycle of oscillation ($T \sim 0.33$ ms) in the slices perpendicular to the acoustic velocity direction. Even an acoustic excitation with very low amplitude could substantially modify the injector flow dynamics. Some sinuous wave-like structures are clearly observed on the jet surface. Figure 12 shows the evolution of the temperature field in the slices parallel to the acoustic velocity direction. No obvious sinuous structure exists; suggesting that oscillatory motion of the jet is primarily in the direction

perpendicular the acoustic velocity and is two-dimensional. The jet spreads wide and the inner potential core is reduced under the acoustic excitation. The same observation is obtained in the experiments conducted by Davis et. al [7-9,12]. A parametric study is ongoing to quantify the influence of acoustic wave on the injector flow evolution.

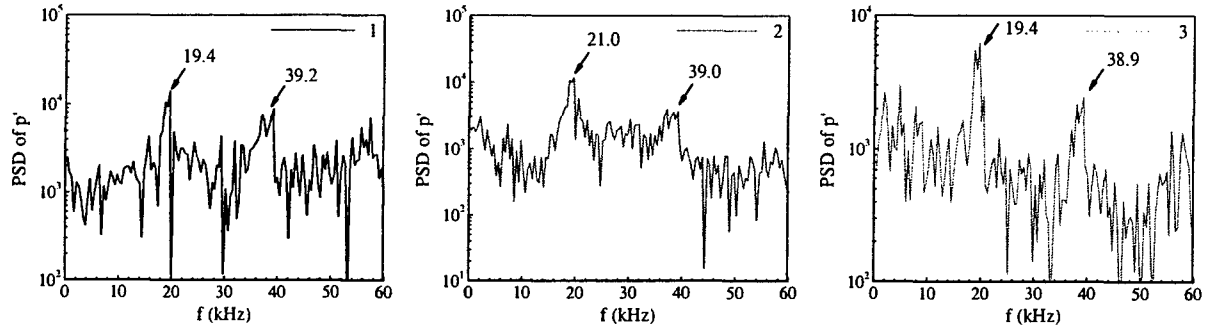


Figure 10. Power spectral densities of pressure oscillations.

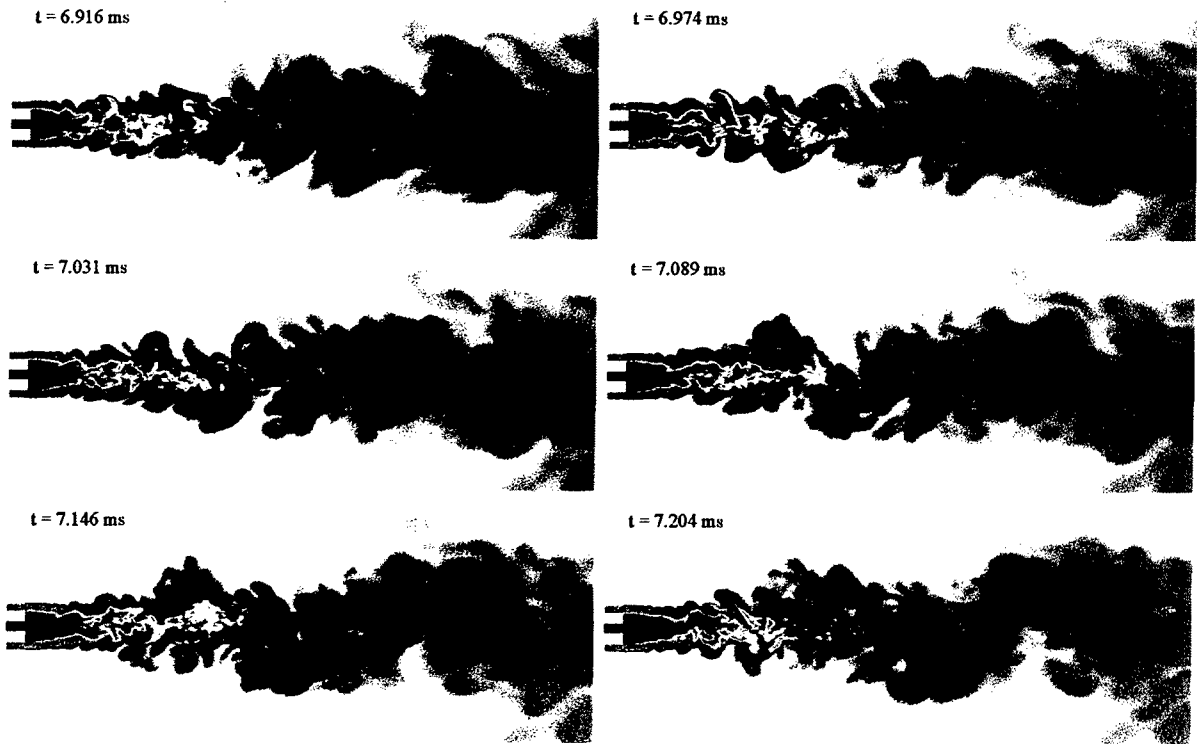


Figure 11. Consecutive snapshots of temperature field in the slices perpendicular to the acoustic velocity direction. Time increases with an interval of $57.6 \mu\text{s}$ between frames.

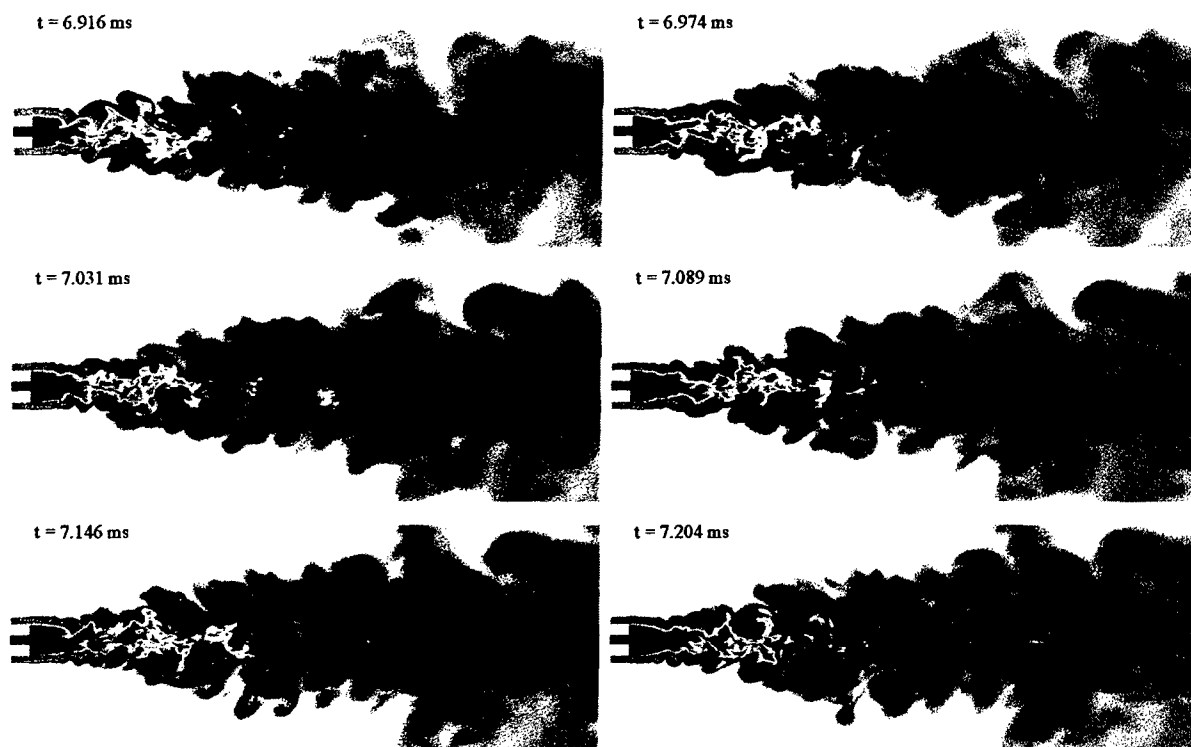


Figure 12. Consecutive snapshots of temperature field in the slices parallel to the acoustic velocity direction. Time increases with an interval of $57.6\mu\text{s}$ between frames.

3.5 Conclusion

A comprehensive numerical analysis has been conducted to investigate shear coaxial injection and mixing of cryogenic and gaseous nitrogen under supercritical pressures. The model accommodates full conservation laws, real-fluid thermodynamics and transport phenomena over the entire fluid state of concerned. The influences of ambient pressure and momentum flux ratio on the injector flow dynamics are systematically investigated. The effects of external acoustic forcing on the flow evolution are also carefully examined. Various important flow features that greatly influenced the injector dynamics are captured. Major results are summarized below.

1. The near-field injector flow dynamics could be characterized by the evolution of three shear layers originating from the rims of the two concentric tubes. Due to the greater velocity difference between the high-speed outer stream and the surroundings, the evolution of the outer shear layers prevails over the inner one.
2. A wake/recirculation region is observed immediately behind the post. It oscillates at a frequency the same as the dominant vortex shedding frequency of the shear layer. The interaction between the wake region and the annular jet is revealed.
3. Owing to the intensive fluid property variations in the flow field, a series of large density-gradient regions are formed around the jet surface. The existence of those large density-gradient regions significantly influences the injector flow dynamics.
4. The dominate effects of the momentum flux ratio/velocity ratio on the flow evolution are demonstrated. As the injection velocity of the annular stream increases, turbulent mixing is greatly enhanced. The inner and outer potential cores are reduced.

5. The influence of ambient pressure on the jet mixing and entrainment is also examined. An increase of chamber pressure gives rise to a shorter inner potential core and a smaller jet spreading angle. The trend is consistent with the experimental observations.
6. The external acoustic excitation has substantial influence on the injector flow dynamics. Even an acoustic wave at very low amplitude could lead to noticeable sinuous wave-like structures on the jet surface. The two-dimensional characteristics of those wavy structures are confirmed.

Reference:

- [1] Culick, F. E. C., and Yang, V., "Overview of Combustion Instabilities in Liquid-Propellant Rocket Engines," *Progress in Astronautics and Aeronautics*, Vol. 169, pp. 3-37, 1995.
- [2] Harje, T. D., and Reardon, H. F., "Liquid Propellant Rocket Combustion Instability," NASA SP-194, 1972.
- [3] Mayer, W., and Krülle, G., "Rocket Engine Coaxial Injector Liquid/Gas Interface Flow Phenomena", *J. Propulsion and Power*, Vol. 11, No. 3, 1995.
- [4] Rehab, H., Villiermaux, E., and Hopfinger, E. J., "Flow Regimes of Large-Velocity-Ratio Coaxial Jets", *F. Fluid Mech.*, vol. 345, pp. 357-381, 1997.
- [5] Rehab, H., Villiermaux, E., and Hopfinger, E. J., "Geometrical Effects on the Near-Field Flow Structure of Coaxial Jets", *AIAA Journal*, Vol. 36, No. 5, 1998.
- [6] Lasheras, J. C., Villiermaux, E., and Hopfinger, E. J., "Break-up and atomization of a Round Water Jet by a High-speed Annular Air Jet", *J. Fluid Mech.*, Vol. 357, pp. 351-379, 1998.
- [7] Davis, D. W., and Chehroudi, B., "The Effects of Pressure and Acoustic Field in a Cryogenic Coaxial Jet," 42nd AIAA Aerospace Sciences Meeting & Exhibit, AIAA, Washington, DC, 5-8 Jan. 2004.
- [8] Chehroudi, B., Davis, D. W., and Tally, D. G., "Initial Results from a Cryogenic Coaxial Injector in an Acoustic Field," 41st AIAA Aerospace Sciences Meeting and Exhibit, AIAA Washington, DC. 6-9 Jan. 2003.
- [9] Davis, D. W., Chehroudi, B., and Sorensen, I., "Measurements in an Acoustically Driven Coaxial Jet Under Supercritical Condition," 43rd AIAA Aerospace Sciences Meeting and Exhibit, AIAA, Washington, DC, 10-13 Jan. 2005.
- [10] Erlebacher, G., Hussaini, M. Y., Speziale, C. G., and Zang, T. A., "Toward the Large Eddy Simulation of Compressible Turbulent Flows," *Journal of Fluid Mechanics*, Vol. 238, pp. 155-185, 2001.
- [11] Graboski, M. S., and Daubert, T. E., "A Modified Soave Equation of State for Phase Equilibrium Calculation, 1. Hydrocarbon Systems," *Industrial and Engineering Chemistry Process Design and Development*, Vol. 17, pp.443, 1978.
- [12] Davis, D. W., "On the Behavior of a Shear-Coaxial Jet, Spanning Sub- to Supercritical Pressures, with and without an Externally-Imposed Transverse Acoustic Field", Ph.D. Thesis, Pennsylvania State University, 2005.
- [13] Dubief, I., and Delcayre, F., "On coherent-vortex identification in turbulence," *J. Turbulence*, Vol. 1, 011 2000.

Task 4

Flow and Flame Dynamics of Shear Co-axial Injectors with Liquid Oxygen (LOX) and Methane

The numerical analysis has also been applied to examine the key phenomena and mechanisms associated with the coaxial injection and combustion of LOX and methane. Emphasis is placed on the flame stabilization and flow/flame interactions in the near field. Co-flowing methane (outer) and oxygen (inner) streams, separated by the central LOX post, are injected through the injector. The inner diameters of the LOX post and the methane annulus are 3.4 and 5.2 mm, respectively. Fully developed turbulent pipe flows are assumed at the injector exit. The computational domain downstream of the injector measures a length of $40D_{LOX}$ and a radius of $12D_{LOX}$, where D_{LOX} is the diameter of the LOX tube. Such dimensions are sufficient to minimize the effect of the far-field boundary conditions on the near-field flow evolution. A quasi-axisymmetric simulation was conducted. The entire grid system consists of 360×240 cells along the axial and radial directions, respectively. The mean grid size of $10 \mu\text{m}$ falls in the subinertial-range of the turbulent kinetic energy spectrum estimated based on the inlet Reynolds number of the oxygen stream. To resolve the wake region and vortical structures which shed downstream from the rim of the LOX post, a total of 40 grid points are used to cover the LOX post in the radial direction. Two different simulation conditions are considered herein. In Case 1, liquid oxygen and methane are injected at temperatures of 122 and 300 K, respectively. The bulk velocities of the two streams are 13 and 75 m/s, respectively. The mixture ratio of 3 is typical of operational engines. In Case 2, the LOX inlet temperature and velocity remain fixed, but the temperature of the methane stream increases to 450 K. Consequently, the methane stream velocity becomes 132 m/s to maintain the same mixture ratio as that in Case 1. The momentum flux ratio of the two streams, increases from 2.5 of Case 1 to 4.3 of Case 2. Such a variation allows a careful investigation of the effects of momentum-flux ratio, a key parameter in the design of shear coaxial injectors, on the flame stabilization characteristics.

Results from this task have led to the following technical publications.

"Near-Field Flow and Flame Dynamics of LOX/Methane Shear coaxial Injector under Supercritical Conditions," by N. Zong and V. Yang, to appear in *Proceedings of the Combustion Institute*, 2006.

"Supercritical LOX/Methane Flame Stabilization and Dynamics in a Shear Coaxial Injector," by N. Zong and V. Yang, AIAA Paper 2006-0760, presented at the 44th AIAA Aerospace Sciences Meeting and Exhibit, January 2006.

"High- Pressure LOX/Methane Mixing and Combustion Processes," by N. Zong and V. Yang, AIAA Paper 2005-0152, presented at the 43rd AIAA Aerospace Sciences Meeting and Exhibit, January 2005.

4.1 Introduction

Extensive experimental and theoretical studies have been conducted to improve the understanding of cryogenic-propellant mixing and combustion under both trans- and super-critical conditions. Most of the previous work was focused on systems involving liquid oxygen (LOX) and gaseous hydrogen [1]. For future development of high-performance reusable liquid rocket engines, combustion of LOX and methane has recently attracted considerable interest. The key issues of

concern include injector dynamics, combustion efficiency and stability, and chamber cooling, to cite a few.

As an attempt to address these questions, Zurbach et al. [2] conducted a preliminary flow visualization of shear coaxial injection and combustion of LOX and methane at near-critical pressures. Shadowgraph images were obtained to reveal that the flame was attached to the LOX post and spreaded downstream along the oxygen jet boundary, a phenomenon quite similar to that observed for the LOX/hydrogen system. Singla et al. [3] later performed a more detailed experiment of high-pressure oxygen and methane combustion associated with a shear coaxial injector. The temperature of the oxygen stream remained at 85 K, whereas the methane stream took a value between 120 and 288 K to simulate trans- and super-critical injection conditions. The chamber pressure varied from 4.5 to 6.0 MPa. Emission images of excited OH and CH radicals were recorded and time-averaged to determine the mean flame structure. Results indicated that the flame was stabilized in the vicinity of the LOX post tip under all flow conditions. Since vaporization was the slowest process at a subcritical temperature, part of the unburned oxygen droplets penetrated into the inner flame. After vaporization and mixing with gaseous methane at the outer boundary of the methane stream, a second flame with a greater expansion angle was formed. Therefore, when both LOX and methane were injected at a transcritical condition, the flame featured two different regions of light emission, one surrounding the liquid oxygen jet and the other located close to the outer boundary of the annular methane stream. The situation changed if oxygen was injected at a subcritical temperature while methane was gaseous. The resultant enhancement of turbulent mixing led to only one flame surrounding the oxygen jet.

In parallel to the experimental studies, a comprehensive numerical model for high-pressure fluid mixing and combustion was recently developed [4]. The analysis is employed in the present work to explore various fundamental physiochemical mechanisms associated with shear co-axial mixing and combustion of LOX and methane under representative engine operating conditions. The effects of the momentum flux ratio of the two propellant streams on the near-injector flow and flame dynamics are examined in detail.

4.2 Theoretical formulation and numerical treatment

The basis of the present work is the general theoretical/numerical framework described in Refs. [5-678]. The formulation accommodates the full conservation laws and real-fluid thermodynamics and transport over the entire temperature and pressure regime of concern. Turbulence closure is achieved by means of a large-eddy-simulation (LES) technique, in which large-scale motions are calculated explicitly and the effects of unresolved small-scale turbulence are modeled either analytically or empirically. The Favre-filtered mass, momentum, energy, and species conservation equations are derived by filtering small-scale dynamics from resolved scales over a well-defined set of spatial and temporal intervals. The effects of subgrid-scale (sgs) motions are treated using the model proposed by Erlebacher et al. [9]. It employs a Favre-averaged generalization of the Smagorinsky eddy viscosity model coupled with a gradient-diffusion assumption to simulate sgs energy and species transport processes. The Smagorinsky coefficients CR (≈ 0.01) and CI (≈ 0.007) are determined empirically. Thermodynamic properties, such as enthalpy, Gibbs energy, and constant-pressure specific heat, are obtained directly from fundamental thermodynamics theories and a modified Soave-Redlich-Kwong (SRK) equation of state [10]. Transport properties, such as viscosity and thermal conductivity, are evaluated using an extended corresponding-state theory [11, 12] along with the 32-term Benedict-Webb-Rubin equation of state

[13]. Mass diffusivity is obtained by means of the Takahashi method, calibrated for high pressure conditions [14]. The implementation and validation of the property evaluation schemes were detailed by Yang [15] and Meng et al. [8]. Owing to the lack of detailed chemical kinetics schemes for oxygen and methane at high pressures, a one-step global reaction model involving four species (CH₄, O₂, CO₂, H₂O) is employed for the combustion of oxygen and methane [16].

4.2.1 Turbulence/flame-structure interaction

The modeling of turbulence/chemistry interaction in a physically meaningful manner represents a critical and challenging issue in the present study of supercritical combustion. Cuenot and Poinot [17] suggested, based on the results from the direct numerical simulations (DNS) of flame/vortex interactions, that such interaction in a non-premixed turbulent flame be characterized by two non-dimensional parameters: turbulent Reynolds number Re_t , and turbulent Damkohler number D_a , defined respectively as follows,

$$Re_t = \frac{u' l_t}{\nu} \propto (l_t / l_d)^{4/3} \quad (1)$$

$$D_a = \frac{\tau_t}{\tau_c} = \frac{\tau_t}{\tau_k} \frac{\tau_k}{\tau_c} \propto 2\sqrt{Re_t} D_a^f \quad (2)$$

where τ_t , τ_c , and τ_k are the characteristic times for turbulent integral-scale motions, chemical reactions, and molecular diffusion, respectively, and ν the kinematic viscosity. The turbulent integral and Kolmogorov length scales are denoted by l_t and l_d , respectively. u' is the characteristic velocity of eddies of size l_t . The local flame Damkohler number D_a^f is defined as the ratio of the flow residence time to the chemical time ($D_a^f = \tau_f / \tau_c$). Depending on the values of the Reynolds and Damkohler numbers, the characteristics of non-premixed combustion can be classified into four different regimes as illustrated in Fig. 1 [17]. Thin flames, also identified as flamelets, take place when the chemical time τ_c is small and Damkohler number D_a is large. As the chemical time τ_c increases and the flame thickness becomes the same order of magnitude as the length scale of the Kolmogorov eddies, the emerging of unsteady effects must be taken into account. Flame extinction occurs for very slow chemical reactions, corresponding to the low Damkohler number regime in Fig. 1. For a turbulent diffusion flame, the local flame thickness and reaction rate depend strongly on such flow conditions as the strain rate, and are affected by various unsteady effects encountered. The flame structures may vary at different spatial locations in the flowfield.

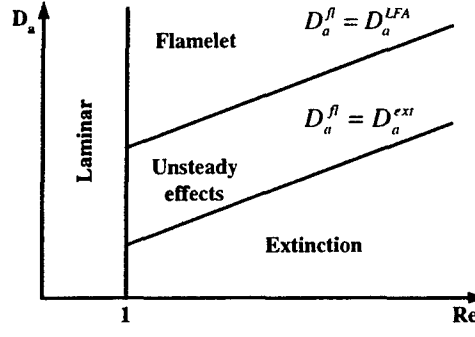


Fig. 1 Regimes for turbulent non-premixed combustion as a function of the Damkohler number $D_a = \tau_t / \tau_c$ and the turbulent Reynolds number Re_t .

Several closure schemes, such as the linear-eddy [18], conditional-momentum-closure [19], laminar-flamelet [20], and probability-density-function (PDF) [21] methods, have been proposed. An accurate and efficient treatment of turbulence/chemistry interactions within the context of LES, however, still remains to be established, even for ideal-gas mixtures. The situation becomes more challenging for supercritical fluids due to complications arising from steep property variations and the lack of basic flame properties at high pressures. Even a well-calibrated *sgs* model for pure fluid-dynamic processes is not currently available. In light of this limitation, a simplified approach is adopted in the present work. It is well known that the Reynolds number increases almost linearly with pressure. An increase in pressure from 1 to 100 atm gives rise to an increase of the Reynolds number by two orders of magnitude. The corresponding Kolmogorov microscale increases by 1.5 orders of magnitude. As a consequence, under supercritical conditions, the Reynolds number may reach such a level that the turbulent eddies may penetrate into the flame zone and greatly enhance the mixing process. This leaves chemical reactions a rate-controlling process. The resolved-scale chemical source can thus be evaluated through a direct closure approach without considering the contributions from *sgs* fluctuations. The filtered reaction rate $\bar{\omega}$ is modeled as,

$$\overline{\dot{\omega}_k(\bar{\rho}, T, Y_1, Y_2, \dots, Y_N)} = \dot{\omega}_k(\bar{\rho}, \tilde{T}, \tilde{Y}_1, \tilde{Y}_2, \dots, \tilde{Y}_N) \quad (3)$$

In spite of the neglect of *sgs* contributions, the approach allows for fluctuations in species production rates as functions of instantaneous flow properties and accounts for finite-rate chemistry. The model uncertainty and error can be effectively reduced if the spatial and temporal resolutions in numerical simulations approach the length and time scales of *sgs* fluctuations.

4.2.2 Computational domain and boundary conditions

Figure 2 shows the physical model under consideration. A methane (outer) and an oxygen (inner) stream, separated by a 0.38 mm thick LOX post, are delivered to a co-axial injector. The inner diameter of the LOX post is 3.42 mm, and the outer diameter of the methane annulus is 5.18 mm. The injector geometry is chosen to match that employed in an experimental study of high-pressure LOX/methane combustion [22]. The computation domain includes the injector and a downstream region that measures $6D_{LOX}$ and $40D_{LOX}$ in the radial and axial directions, respectively. Because of the enormous computational effort required for calculating the flowfield in the entire three-dimensional regime, only a cylindrical sector with periodic boundary conditions

specified in the azimuthal direction is treated herein. The analysis, in spite of the lack of vortex-stretching mechanism, has been shown to be able to capture the salient features of supercritical fluid injection and mixing dynamics [4].

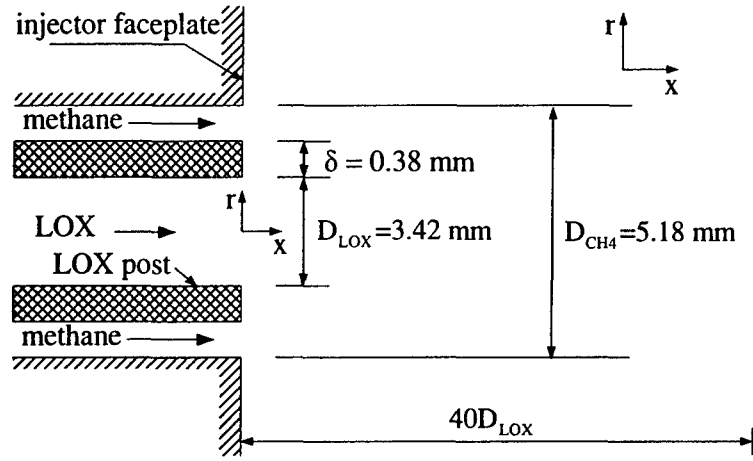


Fig. 2 Schematic diagram of a shear coaxial injector.

The velocity profile for a fully developed turbulent pipe flow is assumed at the injector inlet for both streams. Turbulence is provided by superimposing broad-band white noise onto the mean velocity profile. The disturbances are generated by a Gaussian random-number generator with an intensity of 1% of the mean quantity. The inflow perturbations do not contain any dominant frequency and only serve to trigger the flow instabilities inherent in the shear layers. At the downstream boundary, extrapolation of primitive variables from the interior may cause undesired reflection of waves propagating into the computational domain. Thus, the non-reflecting boundary conditions based on the method of characteristics are applied, along with the specification of a reference pressure [4]. At the radial boundaries, the pressure and temperature are specified as the ambient values. The axial, radial, and azimuthal velocities are extrapolated from the interior. Finally, the no-slip adiabatic condition is enforced along the solid walls.

4.2.3 Numerical framework

The theoretical formulation outlined above requires a robust computational scheme, due to the numerical stiffness caused by rapid flow property variations and wide disparities of the characteristic time and length scales involved. To this end, a unified treatment of general fluid thermodynamics, based on the concepts of partial-mass and partial-density properties, and valid for the entire pressure and temperature regimes of concern, is established and incorporated into a preconditioning scheme [6]. Since the numerical relations, including the Jacobian matrices and eigenvalues, are derived directly from fundamental thermodynamics theories, the algorithm is self-consistent and robust.

The numerical framework employs a density-based, finite volume methodology along with a dual time-step integration technique [23]. Temporal discretization is obtained using a second-order backward difference, and the inner-loop pseudo-time term is integrated with a four-step Runge-Kutta scheme. Spatial discretization is achieved with a fourth-order, central-difference scheme in generalized coordinates. In the present study of LOX/methane combustion, exceedingly large property gradients exist in the near field of the injector where the fluid density varies by a factor of 1000 over a fraction of the LOX post thickness (0.38 mm). To effectively suppress

numerical oscillations in this region and ensure computational stability, the fourth-order scalar dissipation with a total-variation-diminishing switch developed by Swanson and Turkel [24] is implemented. The dissipation coefficient is selected to be $\varepsilon_4 = 0.001$ to minimize the contamination from numerical dissipation.

4.3 Results and discussions

The theoretical model and numerical scheme established in the preceding sections are implemented to study the coaxial injection and combustion of LOX and methane under supercritical conditions. Table 1 summarizes the flow conditions considered herein. In Case 1, liquid oxygen and methane are injected at temperatures of 122 and 300 K, respectively. The bulk velocities of the two streams are 13 and 75 m/s, respectively. The mixture ratio of 3 is typical of operational engines. In Case 2, the LOX inlet temperature and velocity remain fixed, but the temperature of the methane stream increases to 450 K. Consequently, the methane stream velocity becomes 132 m/s to maintain the same mixture ratio as that in Case 1. The momentum flux ratio of the two streams, thus, increases from 2.5 of Case 1 to 4.3 of Case 2. Such a variation allows a careful investigation of the effects of momentum-flux ratio, a key parameter in the design of shear coaxial injectors [25], on the flame stabilization characteristics. It is worth mentioning that for both cases, the methane stream remains at a supercritical state, while the LOX stream enters the injector at a transcritical temperature. The volume downstream of the injector is preconditioned with H₂O and CO₂ with a stoichiometric composition for oxygen/methane combustion. The chamber pressure of 10 MPa is well above the critical pressures of oxygen (5.04 MPa) and methane (4.60 MPa).

Table 1 Simulation Conditions

	Case 1	Case 2
p (atm)	100	100
T_{LOX} (K)	122	122
T_{CH_4} (K)	300	450
ρ_{LOX} (kg/m ³)	1006	1006
ρ_{CH_4} (kg/m ³)	75	42
u_{LOX} (m/s)	13.06	13.06
u_{CH_4} (m/s)	75	132
$(\rho u^2)_{CH_4} / (\rho u^2)_{LOX}$	2.5	4.3
$\dot{m}_{LOX} / \dot{m}_{CH_4}$	3.0	3.0
Re_{LOX}	3.9×10^5	3.9×10^5
Re_{CH_4}	1.2×10^5	9.5×10^4

The computational grid for the regime downstream of the injector consists 360×240 points along the axial and radial directions, respectively. The grids are clustered in the shear layers and near the injector to resolve rapid property variations in those regions. The smallest grid size in the radial direction is 6 μ m, which well falls in the inertial sub-range of the turbulent kinetic energy spectrum estimated using the Kolmogorov-Obukhov theory. The computational domain is divided into 31 blocks, with each calculated on a single processor of a distributed computing facility. The physical time step is 100 nano-seconds and the maximum CFL number for the inner-loop pseudo-

time integration is 0.7. A grid independence study is performed on a fine grid of 540×360 cells for Case 1. No discernible changes of the near-field flow and flame dynamics are observed in terms of the mean properties and vortex shedding frequency phenomenon. The grid system employed in the present work appears to be credible.

Figure 3 shows the instantaneous fields of temperature, density, vorticity, and mass fractions of methane, oxygen, and water in the vicinity of the LOX post. A diffusion-dominated flame emanates immediately from the LOX post and propagates downstream along the surface of the LOX stream. A wake region, which consists of hot combustion products, effectively separates the methane and LOX streams. Similar to the non-reacting flow cases [26], the near-field flow dynamics are characterized by the evolution of the three mixing layers originating from the inner and outer edges of the methane annulus and the inner rim of the LOX post. The development of the inner mixing layer of the methane stream, however, is slightly inhibited by the expansion of the combustion products in the flame zone. Because of the liquid-like behavior of the oxygen jet, a steep density gradient exists between the flame and the oxygen stream. As a result, the large-scale vortices emerging from the outer rim of the LOX post evolve in a manner analogous to that produced by a backward-facing step and mainly reside on the lighter fluid side. The evolutions of those vortices significantly enhance the mixing of methane and hot products. The denser oxygen stream is less influenced. The vortices interact and coalesce with their neighboring vortices while convecting downstream. The flame residing between the oxygen and methane streams appears to be quite resistant to flow straining. Even the strong strain rate generated during the vortex-pairing process does not cause the flame front to break up.

The higher momentum-flux ratio in Case 2 exerts a substantial influence on the flow evolution. Both the inner and outer mixing layers of the methane stream become more dynamic, and the associated instability waves roll up into vortices at an upstream location. The vortices formed downstream of the LOX post are stronger, thereby enhancing the mixing between methane and hot combustion products and shortening the potential core of the LOX stream. The interactions among vortices give rise to a much more complicated flowfield with the emergence of small structures. The potential core of the methane stream is also significantly reduced.

To further explore the flow structure, the instantaneous flow properties are time averaged over two flow-through times after the calculated flowfield has reached its stationary state. Figure 4 shows the time-averaged fields of temperature, density, specific heat, and compressibility factor of Case 1. The constant-pressure specific heat has been normalized with respect to the value at the initial state of the LOX jet. The potential core of the methane stream and the flame zone are clearly observed in the temperature field. The fluid density varies from 10 to 1000 kg/m^3 over a very small spatial domain close to the LOX post. Such a steep density gradient makes this region behave like a contact discontinuity [5,27]. The specific heat exhibits an anomalous variation across the LOX jet boundary. It increases rapidly and reaches a peak as the fluid temperature transits from a subcritical to a supercritical value on the isobaric curve [7]. This effect, combined with the low thermal conductivity (not shown), facilitates the formation of a strong density-gradient region between the LOX jet and hot combustion products [7]. The compressibility factor, which measures the departure from the ideal-gas behavior, has values of 0.30 and 0.87 in the core regions of the LOX and methane streams, respectively. It increases expeditiously and approaches unity in the hot products, where the real-fluid effects essentially diminish due to the local high temperature.

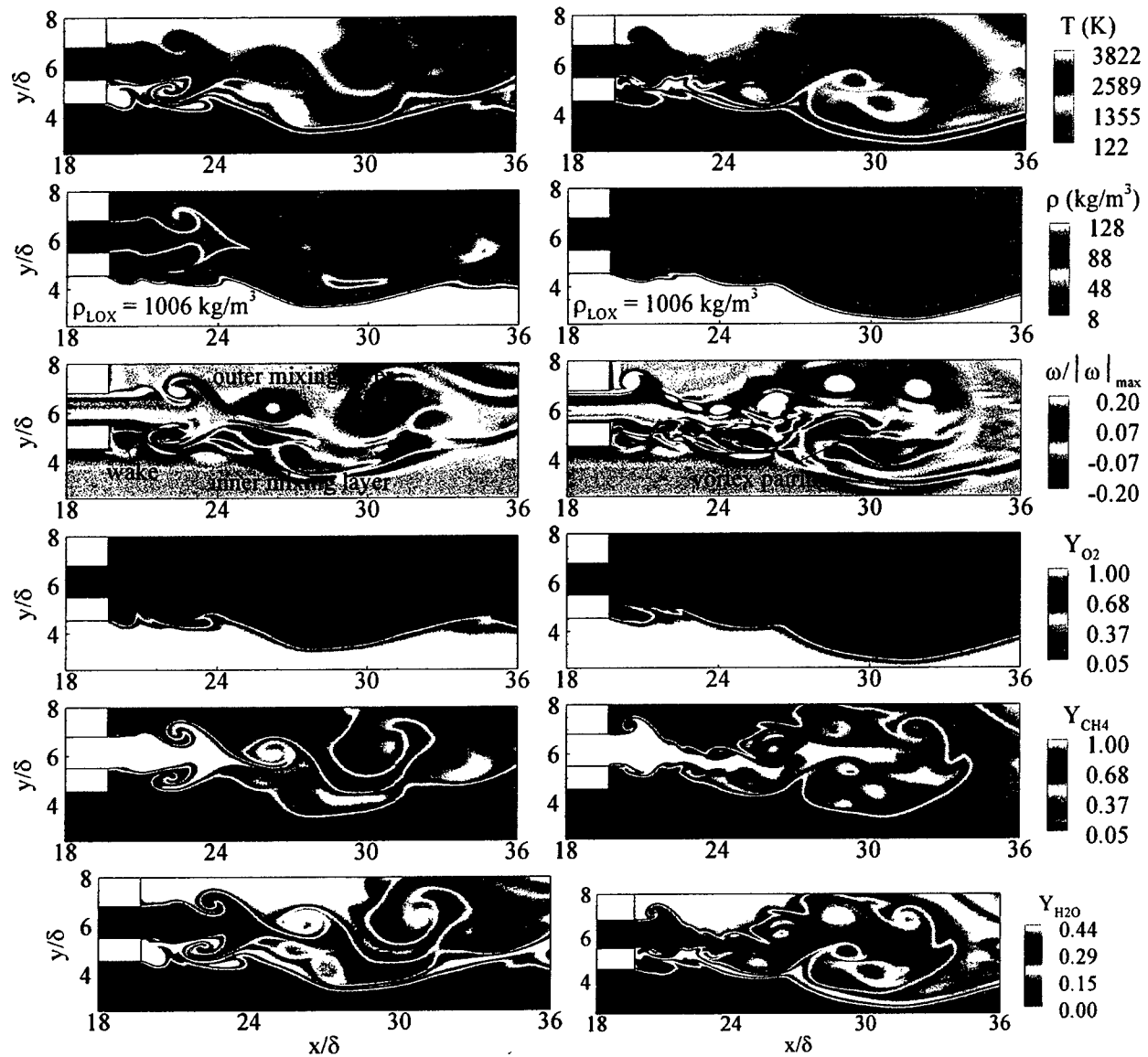


Fig. 3 Snapshots of distributions of temperature, density, vorticity, and mass fractions of oxygen, methane, and water immediate downstream of the injector LOX post for Cases 1 and 2 in Table 1.

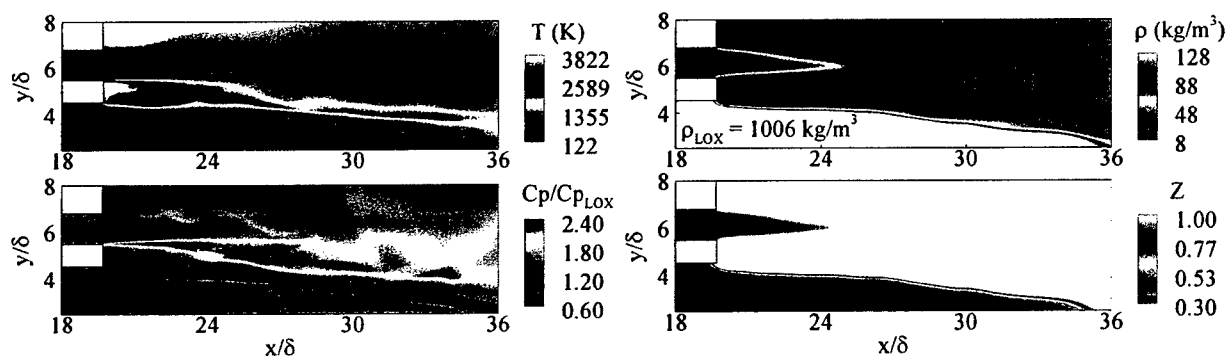


Fig. 4 Short-time averaged temperature, density, constant-pressure specific heat, and compressibility-factor fields of Case 1 in Table 1.

Flame stabilization represents a critical issue in the combustor design. For a shear coaxial injector with cryogenic propellants, the flame is stabilized by the recirculation flow downstream of the LOX post, a phenomenon first quantified in Ref. [5]. Several experimental and numerical studies [5, 27-29] of shear coaxial injection and combustion of LOX/hydrogen have confirmed that such a strong recirculating flow acts as a hot-product pool providing the energy to ignite incoming propellants. Figure 5 shows the temporal evolution of the temperature and velocity-vector fields in the vicinity of the LOX post. The solid lines in the velocity-vector fields correspond to the isotherm of 3000 K, which represents the flame boundary. The large-scale vortices emerging from the outer rim of the LOX post facilitate the mixing between the incoming methane stream and hot products. Driven by those vortices, a relative weak recirculation flow forms close to the inner rim the LOX post and convects the oxygen-rich products toward the methane stream. Unlike the case with LOX/hydrogen combustion, in which the flame is anchored very close to the LOX jet boundary due to the high diffusivity of hydrogen and the strong inertia of the LOX jet [5,27], the LOX/methane flame is anchored between two counter-rotating wake recirculation zones, as illustrated schematically in Fig. 6.

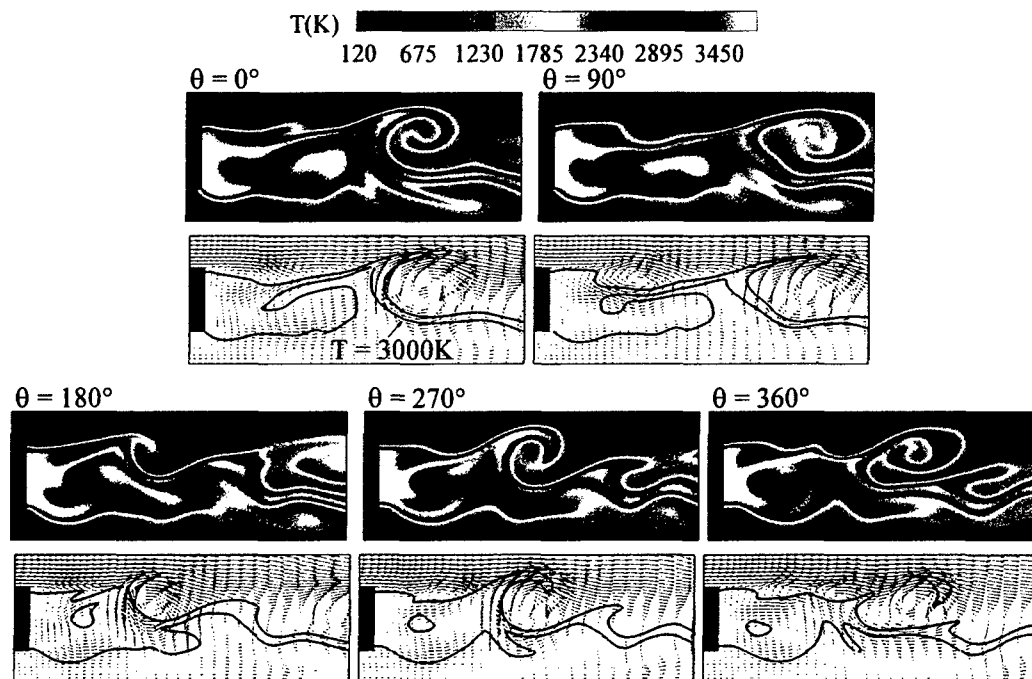


Fig. 5 Time evolution of temperature and velocity-vector fields in the vicinity of LOX post of Case 1 in Table 1; solid lines correspond to the isotherm of 3000 K.

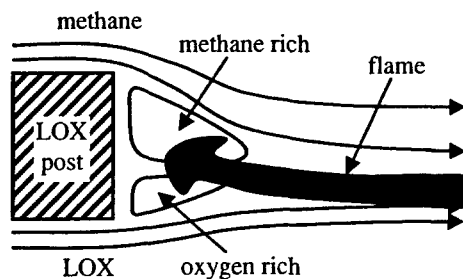


Fig. 6 Schematic diagram of flame anchoring mechanism.

Figure 7 shows the time histories of the fluctuating axial velocities at three different axial locations along the inner and outer shear layers of the methane stream. The locations of Probes 1, 2, and 3 correspond to the positions of the initial instability wave, vortex roll-up, and vortex pairing in the outer shear layer. Small velocity fluctuations are observed in the early stage of the shear layer development. As the vortices roll-up downstream, periodic flow oscillations are clearly observed at Probe 2. The amplitudes of the velocity fluctuations further increase with the growth of the vortices (Probe 3). The effects of chemical reactions on the vortex evolution can be identified from the temporal behaviors at Probes 4-6 along the inner shear layer, which are close to the flame zone. In addition to those well-organized flow oscillations, there exist high-frequency fluctuations. The phenomenon can be attributed to the volume dilatation produced by the oscillatory flame [30]. As a consequence of the strong interactions between vortices, as well as their coupling with the flame, the velocity fluctuation at Probe 6 starts to lose its periodic identity. A closely similar behavior is observed in Case 2 (not shown).

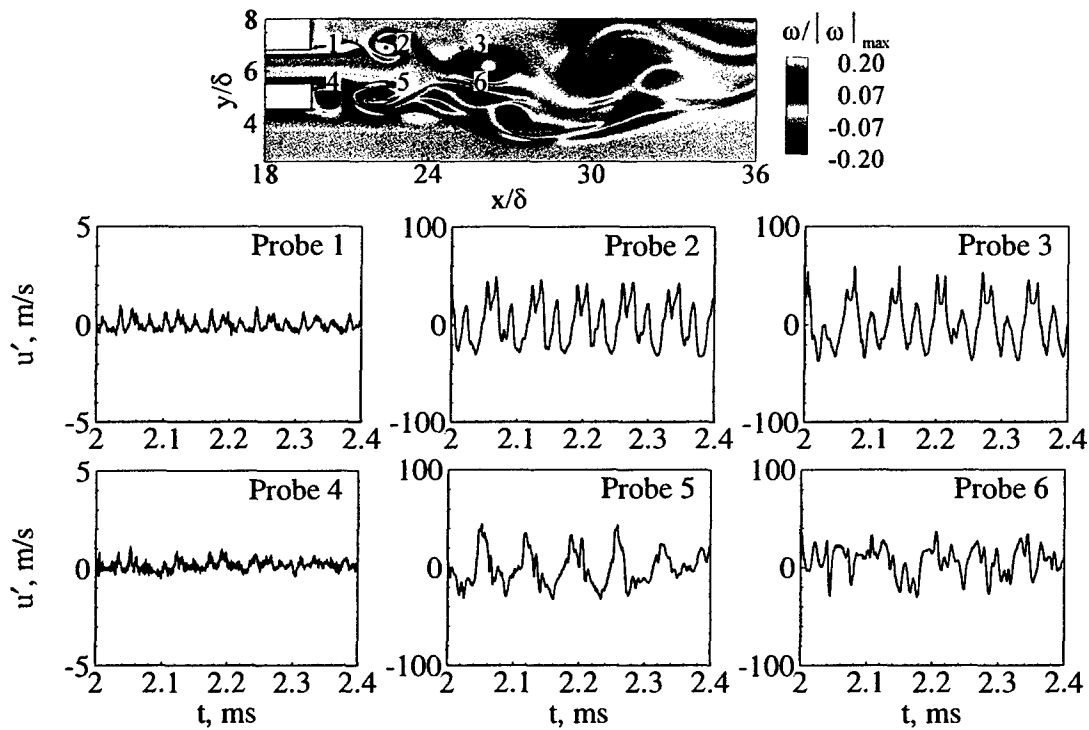


Fig. 7 Time histories of axial velocity oscillations along the inner and outer mixing layers of the methane stream of Case 1 in Table 1.

Figure 8 shows the power spectral densities of the axial-velocity fluctuations at Probe 2 and 5 for Cases 1 and 2. A dominant frequency of 13.8 KHz, corresponding to the vortex shedding frequency, is obtained in both the outer and inner shear layers for Case 1. Higher harmonics exist in the outer shear layer, but their magnitudes become much smaller in the inner shear layer. For Case 2, the higher momentum flux of the methane stream causes an increase of the vortex shedding frequency to 17.2 kHz. Rehab et al. [31] studied the flow characteristics of a coaxial water jet without a splitter between the two streams. They suggested that the outer shear-layer dynamics are dominant over the inner one, and the most amplified frequency can be predicted by the correlation proposed by Schadow and Gutmark [32]. The vortex shedding frequencies obtained in the present work, however, do not confirm their correlation. The existence of a second length scale (i.e., the

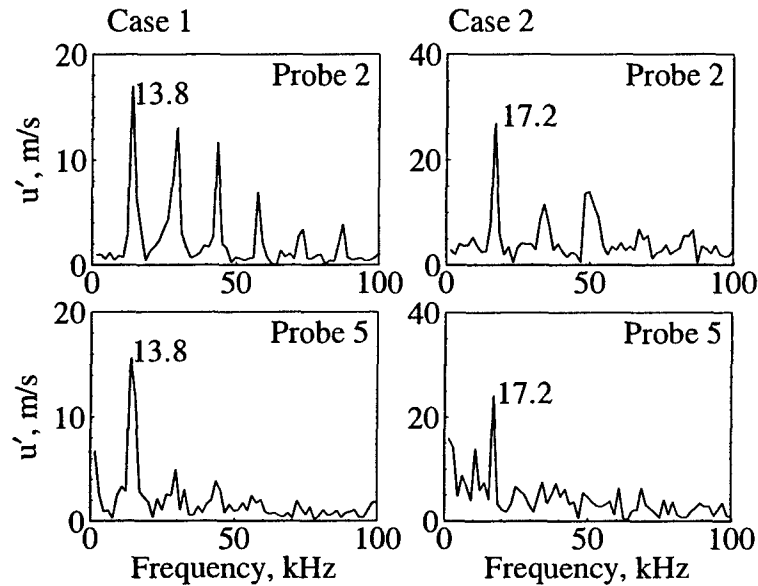


Fig. 8 Frequency spectra of axial velocity oscillations in the inner and outer mixing layers of the methane stream of Cases 1 and 2 in Table 1.

LOX post thickness) and the severe density stratification between the LOX jet and hot products significantly modify the near-field flow dynamics. The vortices shed from the LOX post tip in a manner similar to the vortex generated behind a backward-facing step, where the eddy-formation frequency is on the order of 0.1 in terms of the Strouhal number defined based on the bulk velocity of the outer stream and the step thickness [33].

4.4 Conclusions

A comprehensive theoretical/numerical framework has been established to study the mixing and combustion of co-flowing liquid oxygen (LOX) and gaseous methane through a shear co-axial injector. The physical model and flow conditions are representative of cryogenic-propellant rocket engine injectors operating at supercritical pressures. The formulation is based on the full conservation laws, and takes into account real-fluid thermodynamics and transport phenomena. Turbulence closure is achieved using a large-eddy-simulation technique. The work allows for a thorough investigation into the injector flow development and flame dynamics. As a consequence of the large density stratification, the flame is anchored in the wake recirculating region behind the LOX post and propagates along the boundary of the LOX jet. The near-field flow evolution is dictated by the large-scale vortices in the inner shear layer of the methane stream. The dominant frequencies of vortex shedding match those for a rear-facing step flow, a phenomenon that can be attributed to the strong inertia of the LOX stream and lighter density of gaseous methane. The effects of the momentum-flux ratio of the two streams on the injector flow and flame characteristics are also examined.

Reference:

- [1] V. Yang, M. Habiballah, J. Hulka, M. Popp (Eds.), *Liquid Rocket Thrust Chambers: Aspect of Modeling, Analysis, and Design*, Progress in Astronautics and Aeronautics 200 (2004).
- [2] S. Zurbach, J.L. Thomas, C. Verplancke, L. Vingert, M. Habiballah, in: *AIAA-03-5063, 39th AIAA/ASME/SAE/ASEE Joint Propulsion Conference and Exhibit*, 2003.
- [3] G. Singla, P. Scoufflaire, C. Rolon, S. Candel, *Proc. Combust. Inst.* 30 (2004) 2921-2928.
- [4] N. Zong, Ph.D thesis, The Pennsylvania State University, University Park, PA, 2005.
- [5] J.C. Oefelein, V. Yang, *J. Propul. Power* 14 (1998) 843-857.
- [6] H. Meng, V. Yang, *J. Comput. Phys.* 189 (2003) 277-304.
- [7] N. Zong, H. Meng, S.Y. Hsieh, V. Yang, *Phys. of Fluids* 16 (2004) 4248-4261.
- [8] H. Meng, G. C. Hsiao, V. Yang, J. S. Shuen, *J. Fluid Mech.* 527 (2005) 115-139.
- [9] G. Erlebacher, M.Y. Hussaini, C.G. Speziale, T.A. Zang, *J. Fluid Mech.* 238 (1992) 155-185.
- [10] M.S. Graboski, T.E. Daubert, *Ind. Eng. Chem. Proc. Design Dev.* 17 (1978) 443-448.
- [11] J.F. Ely, H.J. Hanley, *Ind. Eng. Chem. Fundamentals* 20 (1981) 323-332.
- [12] J.F. Ely, H.J. Hanley, *Ind. Eng. Chem. Fundamentals* 22 (1983) 90-97.
- [13] R.T. Jacobsen, R.B. Stewart, R.B. J. *Phys. Chem. Ref. Data* 2 (1973) 757-922.
- [14] S. Takahashi, *J. Chem. Eng (Japan)* 7 (1974) 417-420.
- [15] V. Yang, *Proc. of Combust. Inst.* 28 (2000) 925-942.
- [16] C.K. Westbrook, and F.L. Dryer, *Prog. Energy Combust. Sci.* 10 (1984) 1-57.
- [17] B. Cuenot, T. Poinot, *Proc. of Combust. Inst.* 25 (1994) 1383-1390.
- [18] A.R. Kerstein, *J. Fluid Mech.* 240 (1992) 289-313.
- [19] R.W. Bilger, *Phys. Fluids A* 5 (1993) 436-444.
- [20] N. Peters, *Prog. Energy Combust. Sci.* 10 (1985) 319-339.
- [21] S.B. Pope, *Prog. Energy Combust. Sci.* 11 (1985) 119-192.
- [22] R.J. Santoro, Personal correspondence 2005.
- [23] S.Y. Hsieh, V. Yang, *Int. J. Comput. Fluid Dyn.* 8 (1997) 31-49.
- [24] R. C. Swanson, E. Turkel, *J. Comput. Phys.* 101 (1992) 292-306.
- [25] J. Hulka, J.J. Hutt, in: V. Yang, W. Anderson (Eds.), *Liquid Rocket Engine Combustion Instability*, Progress in Astronautics and Aeronautics 169 (1996) 39-72.
- [26] N. Zong, V. Yang, in: *AIAA-05-0152, 43rd AIAA Aerospace Sciences Meeting and Exhibit*, 2005
- [27] J.C. Oefelein, *Proc. Combust. Inst.* 30 (2004) 2929-2937.
- [28] W. Mayer, A. Schik, M. Schäffler, H. Tamura, *J. Propul. Power* 16 (2000) 823-828
- [29] D. Kendrick, G. Herding, R. Snyder, P. Scoufflaire, C. Rolon, L. Vingert, *J. Propul. Power* 14 (5) (1998) 327-339.
- [30] S. Apte, V. Yang, *Combust. Flame* 131 (2002) 110-131.
- [31] H. Rehab, E. Villermux, E.J. Hopfinger, *J. Fluid Mech.* 345 (1997) 357-381.
- [32] K.C. Shadow, E. Gutmark, *Prog. Energy Combust. Sci.* 18 (1992) 117-132.
- [33] D. Wee, T. Yi, A. Annaswamy, A.F. Ghoniem, *Phys. of Fluids* 16 (2004) 3361-3373.